ABSTRACT

Title of Document: PERFORMANCE EVALUATION OF TWO NEW SEISMIC RESISTANT DIAGRID FRAMING SYSTEMS

Nasim Sadat Moghaddasi Bonab,
Doctor of Philosophy, 2011

Directed By: Yunfeng Zhang, Associate Professor
Department of Civil and Environmental Engineering

The diagrid system offers a visually appealing and structurally efficient structural system for gravity load bearing. The architectural elegancy and high structural redundancy of the diagrid structure makes it a desirable choice for tall building design. However diagrid structure is prone to high inelastic deformation demand during strong earthquakes.

To address this issue of limited ductility and energy dissipation capacity in conventional diagrid framing, two new types of seismic resistant diagrid structural systems termed highly energy-dissipative ductile (HED) diagrid and hybrid diagrid framing systems are proposed in this research and their seismic performance is assessed.

The proposed HED diagrid framing system provides a competitive design option in high seismic regions with its high ductility and improved energy dissipation capacity enabled by incorporating replaceable shear links interconnecting the diagonal members at their nodes. A parametric study has been conducted to investigate the effect of different design parameters on the seismic performance of this system.

A new type of composite brace comprised of glass fiber reinforced polymer (GFRP)-tube confined concrete, steel core and post-tensioned tendons, is developed for self-centering diagrid members. The hysteretic behavior of a self-centering chevron assembly comprised of two inclined composite braces is subsequently examined. Constitutive modeling of GFRP-tube confined concrete with high FRP volumetric ratio is conducted with experimental data calibration under monotonic and cyclic compression. The constitutive model is implemented into a finite element analysis platform OpenSees to enable nonlinear analysis of complex structures utilizing this type of confined concrete elements. The self-centering chevrons are implemented in the lower stories of the hybrid diagrid framing system to form base diagonals with large stiffness, enhanced ductility and energy dissipation capability and enable a rocking behavior for the diagrid system.

The structural characteristics and seismic behavior of these two new seismic resistant systems are demonstrated with a prototype 21-story building subjected to nonlinear static and dynamic analysis. The findings from nonlinear time history analysis verify that satisfactory seismic performance can be achieved by these structural systems subjected to design basis earthquakes in California, specifically

showing re-centering behavior while all main structural elements remain elastic in both systems.

PERFORMANCE EVALUATION OF TWO NEW SEISMIC RESISTANT DIAGRID FRAMING SYSTEMS

By

Nasim Sadat Moghaddasi Bonab

Dissertation submitted to the Faculty of the Graduate School of the
University of Maryland, College Park, in partial fulfillment
of the requirements for the degree of
Doctor of Philosophy
2011

Advisory Committee:

Professor Yunfeng Zhang, Chair/Advisor

Professor Amde M. Amde

Professor Bilal M. Ayyub

Professor Chung C. Fu

Professor Sung Lee

ACKNOWLEDGEMENTS

I would like to take this opportunity to express my sincerest appreciation to my advisor, Dr. Yunfeng Zhang, who has always guided, challenged and encouraged me. I also thank Dr. Amde, Dr. Ayyub, Dr. Fu and Dr. Lee for their valuable time serving on my dissertation committee and providing their insight and comments.

I cherish the University of Maryland in which I had some of the best experiences of my lifetime. I would like to express my gratitude to Department of Civil and Environmental Engineering for granting me with A. James Clark School Fellowship, providing me with the great experience of teaching assistantship, and for the Structural Engineering Laboratory facilities in which the experimental tests of this study were conducted. I also appreciate Future Pipe Industries USA, for providing and shipping the GFRP tubes used in this study.

This dissertation is dedicated to beloved people in my life who supported and encouraged me during my graduate study at University of Maryland.

TABLE OF CONTENTS

LIST OF TABLES

LIST OF FIGURES

CHAPTER 1 : INTRODUCTION

1.1. Introduction

Advancements in structural engineering have resulted in more efficient structural systems that allow for taller buildings. As the height of the building increases, the demand on its lateral force resisting system becomes more significant. Moment resisting frames, braced frames, belt and outrigger truss systems, and framed tube systems are widely used as lateral resisting systems for tall buildings. A combination of the lateral force resisting systems with a reinforced concrete core which provides additional lateral stiffness to the structure or a variation of the concept such as the braced tube system or the bundled tube has resulted in high-rise buildings with large height-to-width ratio.

The modern architecture demands new and sustainable structural systems to fulfill its aesthetic expectations without sacrificing the primary governing factor in construction - economy. An efficient structural system requires a proper value for lateral stiffness and sufficiently large ductility and energy dissipation capacity for seismic response mitigation.

The use of diagrid structures because of their effectively large lateral and torsional stiffness as well as architectural benefits has generated interests especially for high-rise buildings. However, the limited ductility and energy dissipation capacity in conventional diagrid framing has limited its widespread use in seismic active

regions and supplemental energy dissipation mechanism has to be incorporated which could compromise the aesthetic aspect of the diagrid building. Without reliable energy dissipation mechanism, considerable numbers of primary structural diagonal elements might yield during strong earthquake events and large residual displacements could potentially raise questions on the functionality of the structure after the earthquake. To address this issue, two new types of seismic resistant diagrid structural systems are proposed in this research and their seismic performance has been evaluated through nonlinear static and nonlinear time history analysis.

1.2. Research Objectives

This dissertation pursues three following objectives all focused toward creating high-performance seismic resistant structural systems:

1- The first objective is to present a new seismic resistant structural system termed "highly energy-dissipative ductile (HED) diagrid" framing system that has high energy dissipation capability and ductility under seismic loading. This system utilizes shear links into conventional diagrid framing system to retain the main structural elements elastic post earthquake events and improve the seismic response of the building. Development of nonlinear finite element model of a prototype HED diagrid structure to examine the seismic performance of the system under strong earthquakes is followed.

2- The second objective of this research is to develop a composite bracing element to use in a chevron assembly with high stiffness and self-centering behavior. The newly proposed brace is comprised of GFRP-tube confined

concrete, steel core, and post-tensioned tendons. The hysteretic behavior of GFRP-tube confined concrete with high volumetric confinement ratio is studied experimentally and analytically. A constitutive model is developed to predict the hysteretic behavior of GFRP-confined concrete. To enable the numerical simulation of complex systems using this type of confined concrete, the calibrated constitutive model is implemented into the OpenSees (Mazzoni, 2009) finite element analysis framework.

3- The third objective is to create a hybrid diagrid framing system with self-centering capability under seismic loading through application of aforementioned composite chevron into the base stories of the diagrid framing system. The composite base diagonals increase the stiffness of the system and localize the deformation at the base stories of the structure. Hybrid diagrid framing system is proposed with the purpose of re-centering performance and minimized downtime and repair cost of the structure after seismic events which are investigated through nonlinear static and time history analysis of a prototype building.

1.3. Organization of the Dissertation

Characteristics of diagrid structural system and the two new seismic force-resisting systems along with the experimental and analytical study of GFRP-tube confined concrete used in axial-load carrying elements of the hybrid diagrid frame are described in the following seven chapters.

Chapter 2 discusses the specifications of diagrid framing system and landmark buildings of this type. A prototype diagrid structure is designed to be used for study of structural performance of conventional diagrid and the new proposed systems. Finite element model of the prototype diagrid structure is developed and the results of nonlinear static analysis is presented.

A novel seismic resistant structural system termed "highly energy-dissipative ductile (HED) diagrid" is presented in Chapter 3. The concept of this system is first discussed and the model used for numerical simulation of shear links behavior is described. The performance of the system under lateral loads is studied through nonlinear static analysis and nonlinear time history analysis of a prototype building under design basis earthquake records scaled for high seismic region in California.

Chapter 4 presents a parametric study on HED diagrid framing system to investigate the influence of the design parameters including diagonals angle and length of shear links on seismic performance of HED diagrid system. New case studies with similar configuration to the original prototype HED diagrid building studied in Chapter 3 are defined and nonlinear static and time history analysis results of each case is presented and compared with that of the original prototype HED diagrid building.

The experimental and analytical study of GFRP-tube confined concrete with high FRP volumetric ratio is presented in Chapter 5. The results of an experimental study on GFRP-tube concrete filled with lightweight and normal concrete under monotonic and cyclic compression is presented. A constitutive model developed for test specimens is presented and development of an analytical tool for numerical modeling of GFRP-tube confined concrete compression elements is explained.

Chapter 6 introduces a new composite brace comprised of GFRP-tube confined concrete, steel core and post-tensioned tendons. The hysteretic behavior of a self-centering composite chevron consisting of two inclined proposed braces is presented and a parametric study is conducted to investigate the influence of different parameters in the mechanical characteristics of the self-centering composite chevron.

Chapter 7 describes a new hybrid diagrid framing system with self-centering behavior. The composite brace presented in Chapter 6 is used as the base diagonals to form a hybrid diagrid framing system with re-centering behavior. The nonlinear static and nonlinear time history analysis results of this system under strong earthquake records are presented.

Chapter 8 presents a summary of the research, conclusions and some recommendations for future research.

CHAPTER 2 : DIAGRID FRAMING SYSTEM; CHARACTERISTICS AND STRUCTURAL PERFORMANCE

2.1. Diagrid Framing System

2.1.1. Introduction

Diagrid structure is the term used for structural system consisting of diagonal grids connected through horizontal rings which create an elegant and redundant structure especially efficient for high-rise buildings. Figure 2- 1 shows a schematic view of the Hearst Tower in New York city with diagrid structural system. In diagrid structure, diagonals modularize several stories (e.g. every four stories in Figure 2- 1). Horizontal beams tie diagonals at connecting nodes and diagonals are laterally supported by the beams at each story level.

Diagrid structure is different from braced frame systems, since diagonals as main structural elements participate in gravity load carrying in addition to lateral load carrying because of their triangulated configuration. In diagrid, axial action of diagonals carries the story shear forces and diagonals function a combined role of column and brace in braced frames

The column free structure of diagrid system grants high architectural flexibility since most geometries can be created with the triangular grids. In addition to visual elegancy, large free façade surface allows for enormous day lighting and the possibility of solar panel installation. Diagrid structural system is also economically

and environmentally sustainable since the buildings designed with diagrid structural system have used about 20% less steel for construction (Moon, 2008a).

In addition to its aesthetic advantages, the structural performance of diagrid system is also appealing due to certain characteristics of this system. The axial action of diagonals controls the shear deformations (e.g. story drifts) in addition to providing high bending rigidity and redundancy. The uniformly distributed angular configuration of diagonals creates an inherently highly redundant structural network that allows multiple load paths (Rahimian and Eilon, 2007) making the system safer under extreme stress condition and incidents such as blast resulting in removal of one or few diagonals.

This chapter studies the characteristics of diagrid structural system. A prototype diagrid building is designed to be used as the base for case studies of two other presented structural systems. The nonlinear static analysis is conducted for this prototype diagrid building.

Figure 2- 1. Schematic view of the Heart Tower with diagrid framing system

2.1.2. Diagrid Landmark Designs

Diagrid structural system has been used for some of the most elegant buildings in different countries. The 40-storey Swiss Re also known as Gherkin in London completed at 2004 is one of the first iconic designs of diagrid framing systems. Both diagonals and rings are made from wide flange hot-rolled sections. The diagrid provides all the required lateral structural stability and the central core only bears the gravity load (Munro, 2004).

The 46-story Hearst Tower in New York City completed in 2006 is another masterpiece design of diagrid structure. It has been estimated that the diagrid structural system employed for this skyscrapper required 20% less steel than the typical moment frame option because of the high efficiency of the triangular configuration for bearing both the gravity and lateral loads (Rahimian and Eilon, 2007). Each module of the structure comprises four stories and intermediate beams were preinstalled with diagonals to facilitate the construction. The nodes are made from 25-cm steel plates connecting the wide flange hot-rolled sections of diagonals.

The CCTV new headquarter building in Beijing, China is a 234-m tall building in the form of a three-dimensional continuous cranked loop formed by a 9-storey podium structure joining two 50-storey high leaning towers which are linked at the top via a 13-storey cantilevered “overhang” structure at 36 stories above the ground (Carrol et al. 2006). An external skin of leaning columns, horizontal edge beams and triangulated bracing on a two-storey pattern was used to form an enclosed tube structure to support the building. The braced tube structure affords a multitude of

alternative load paths. Such a robustness feature is highly desirable, especially in seismically sensitive Beijing (Carrol et al. 2006).

The Bow, is a 59 story skyscraper standing up to 247 meters height will be the tallest building in Western Canada upon expected completion in 2012. With the goal of creating a progressive and sustainable business center, the diagrid system is comprised of six story high diagonal elements of the bow-shaped building. A saving of 20 percent in structural steel material compared to conventional moment frame was reported for this building (Charnish et al., 2008). Built up triangular plate sections were used for the structural elements.

The flexibility required for desired architectural elegancy of the Freedom Tower at the World Trade Center in New York was achieved by diagrid structural system which is paired with the concrete core to provide substantial rigidity for the building. The column free perimeter diagrid was a perfect option for the twisted geometry of the 105-story tower.

Free-form buildings such as Phare Tower in France which have become popular in recent years, take advantage of diagrid framing system for their exterior structure due to its architectural flexibility (Ali and Moon, 2007). The Phare Tower expected to be completed by 2015 combines the aesthetic characteristics of diagrid with sustainability through using wind and solar energy.

2.2. Structural Characteristics and Geometry of Diagrid Structure

Redundancy is a desirable characteristic for robust performance of any load resisting systems. High redundancy is one of the main advantages of the diagrid structural system. The angular configuration of diagonal grids creates multiple load paths through the structure. Similar to gravity load, the lateral load is imposed directly on the nodes connecting diagonals and transferred to rest of diagonals through different load paths. In case of failure of any of diagonal elements, the load is transferred from a failed portion to other diagonals through alternate load paths.

The progressive collapse is defined as global collapse of the structure because of local failure of structural elements. In the study conducted by Kim and Lee (2009) the progressive collapse of diagrid structure was investigated by removing the diagonals of the first story. The analysis results of a 36-stoty and 54-story building indicated that diagrid has high resistance to progressive collapse caused by sudden removal of diagonals. The progressive collapse of the buildings did not occur before removal of about 11% of all diagonal members. This characteristic is very desirable for a lateral force resisting system assuring the global stability of the building despite local failure of some structural elements.

Framed or braced tube systems are widely used for high rise building and since majority of the structural elements are located at the sides of the structure, their structural performance is usually affected by shear lag effect. The increased stress at corner elements due to shear lag effect reduces the structural efficiency of a tube structure and the lateral displacement of the building increases under lateral load. Through a proper design, the buildings with diagrid system are found to perform three

times better than framed tube buildings in mitigating shear lag ratio and lateral deflection (Leonard, 2007).

The greater lateral stiffness of diagrid structure makes it less prone to the vortex-induced lock-in condition in the across-wind direction since a higher wind velocity is required to cause a lock-in condition for buildings with higher fundamental frequency (Moon et. al, 2007).

Higher torsional rigidity is reported for diagrid system among the common structural systems for high-rise buildings (Soo et al. 2008). The aerodynamic form of tall buildings is one of the controlling factors in reducing the wind forces on the structures. Appropriate mass distribution patterns and twisted forms can be applied in tall buildings design for this purpose. Free form designs are possible with diagrid structures to create unique appearance with a progressive design.

Buildings with low height to width ratio behave like shear beams while slender buildings behave more like flexural beams. In the study by Moon et al. (2007) on lateral stiffness of diagrid buildings, the maximum roof displacement was selected as the index to assess the performance of the building under lateral loading. It was found that for 60-story diagrid structure with the aspect ratio (e.g. height to width ratio) of about 7, the optimal range of diagrid angle is between 65° to 75°. For the 42-story building with aspect ratio of about 5 and the 20-story building with the aspect ratio of about 2, the optimal range of diagonals was found to be about 50° to 70° (Moon et al., 2007). Therefore it was shown that the range of optimal angle for diagonals increases for buildings with higher height to width ratio as the bending deformation becomes dominant.

2.3. Prototype Case Study

2.3.1. Objective

To study the performance of conventional diagrid and the two new proposed systems, a prototype high-rise building is designed and presented in this section. A 3x3 bay, 21-story building, with typical story height of 3.65 m (144 inch) and total height of 76.81 m (252 ft.) was selected for the case study. The plan and elevation views of the prototype building are shown in Figure 2- 2. The building has a square plan and is comprised from seven modules in which diagonals modularize every 3 stories.

In the study performed by Moon et al. (2007) on optimal angles for 20-story diagrid buildings with aspect ratio, H/B, of 2.2, it was found that the performance of the building does not change much for the angles ranging from about 50 to 70 degrees. The optimal angle for diagonals increases with the increase of the aspect ratio of the diagrid building. With the aim of obtaining a relatively higher aspect ratio for the prototype building due to material saving, the diagonal angle of 72° was chosen for the prototype building. The building is 21.5x21.5 m (84.7x84.7 ft) in plan which results in aspect ratio of 3.6.

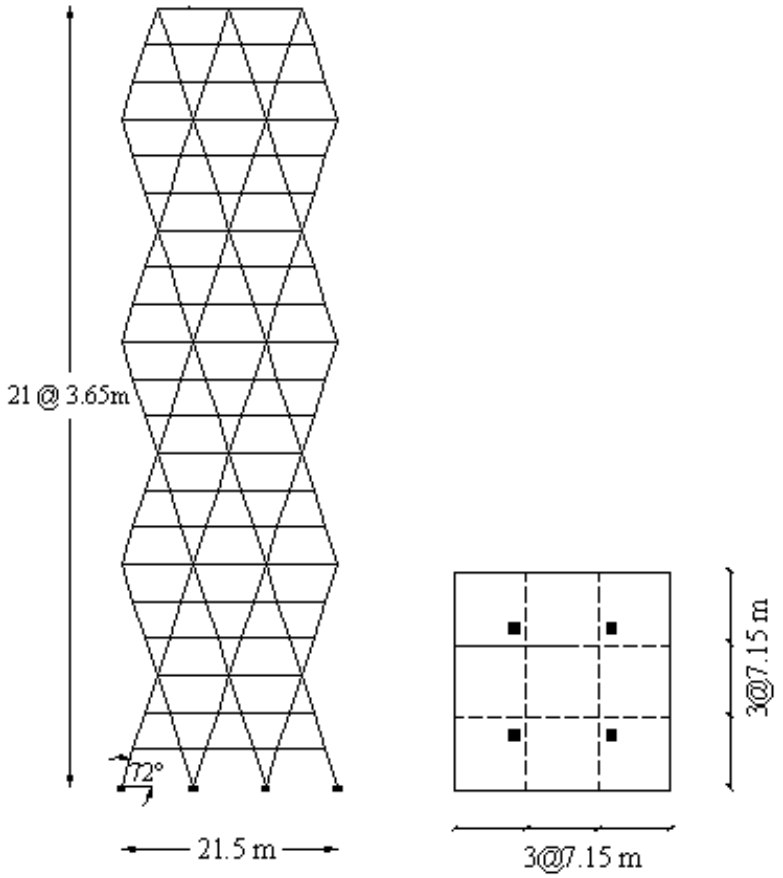

(a) **(b)**

Figure 2- 2. 21-story prototype diagrid building: (a) Elevation; (b) Plan

2.3.2. Design

There are two general approaches to determine the seismic forces in a building: an equivalent static force procedure and a dynamic analysis procedure. For the preliminary design of the prototype building, the equivalent static lateral force procedure of ASCE/SEI 7-10 is employed. The design should satisfy the code requirements for strength and stiffness. The strength check is based on the base shear obtained from equivalent static lateral force procedure. To satisfy the stiffness requirements, the inter-story drift ratios and roof drift ratio obtained from linear analysis should be multiplied by deflection amplification factor, $C_{d,}$ and shall not be larger than 2%.

The design response spectrum corresponding to a hazard level of 10% probability of exceedance in a 50 year period for the Van Nuys, California area was used for the preliminary design. A site class D (stiff soil) and a seismic design category of D was assigned to the prototype building with an importance factor of 1.0. The design spectral accelerations at 0.2 and 1.0 seconds, S_{DS} and S_{D1}, were 1.16 and 0.64 g, respectively. The seismic base shear is determined by the relation (ASCE/SEI 7-10):

$$V = C_s W \tag{2.1}$$

In the above equation, C_s is the seismic response coefficient and W is the effective seismic weight of the building. The total effective seismic weight of the 21-story HED diagrid building is calculated to be 98,660 *kN* (22,180 *kips*); The seismic weight for a typical floor is 4670 kN (1050 kips), based on 6.7 kN/m^2 (140 psf) for

the floors and 1.44 kN/m^2 (30 psf) for the façade. The seismic weight for the roof is 5250 kN (1180 kips), considering 670 kN for rooftop equipment. The floor mass distribution along the building height was assumed to be uniform. Equation 12.8-6 of ASEC7-10 governs for calculation of seismic response coefficient, C_s (ASCE/SEI 7-10):

$$C_s = \frac{0.5S_1}{(\frac{R}{I})} \tag{2.2}$$

In the above equation, S_1 is the mapped maximum considered earthquake spectral response acceleration parameter, R is the response modification factor (a measure of the ability of the structure to withstand seismic forces without collapse) and I is the importance factor. The value of response modification factor of a system is affected by system ductility, seismic energy dissipation capacity, mode of failure mechanisms and past performance of the system. There is no available response modification factor for diagrid system in ASCE/SEI 7-10. Steel diagrid frames systems are usually used as a dual system combined with ductile reinforced concrete core walls in seismic regions and their response modification factor are typically considered between 5.5 to 8.0 (Baker at al., 2010). Hence the response modification factor of 6 recommended in ASCE7-10 for steel special concentrically braced frames is used here. Therefore, the calculated seismic response coefficient is 0.0532 resulted in the seismic base shear of 5250 *kN* for the building. Half of the total seismic weight is considered in the calculation for planar diagrid frame since the building is symmetric.

The story shear at any level is the sum of all the lateral forces introduced at and above that level and is determined from the following equation (ASCE/SEI 7-10):

$$F_x = C_{vx}V \tag{2.3}$$

$$C_{vx} = \frac{w_x h_x}{\sum_{i=1}^{n} w_i h_i} \tag{2.4}$$

where C_{vx} is the vertical distribution factor, w_x *and* w_i *are* the portion of the total effective seismic weight of the structure assigned to level *i* or *x* and h_i and h_x are the height from the base to level *i* or *x.* The detailed calculations for story shears and story moments are presented in Table 2- 1.

In a simplified design methodology for diagrid structure proposed by Moon et al. (2007) the diagrid structure was considered as a beam subdivided longitudinally into units, as shown in Figure 2- 3. Each module encompasses a number of stories depending on the design. Each two modules were considered as a unit acting as web or flange elements depending on the direction of loading; therefore the following equations were derived for calculation of the required area of diagonals as web and flange members (Moon et al., 2007):

$$A_{d,w} = \frac{V}{2nE_d\gamma \sin\theta \cos^2\theta} \tag{2.5}$$

$$A_{d,f} = \frac{2M}{nB^2E_d\chi \sin^3\theta} \tag{2.6}$$

In the above equations V and M are shear and moment of the module, respectively. Parameters γ and χ denote the desired shear and bending deformations,

respectively. The number of diagonals extending over the full height of the module is shown with n and E_d is the modulus of elasticity of the material. Diagonals angle and total width of the building is shown with Θ and B, respectively. For buildings with square plan the required diagonal size should be taken as the larger of the two values calculated for bending and shear. Having the story shears and story moments from Table 2- 1, the minimum required diagonal sizes can be calculated. Designing the structures such that their demands under severe earthquakes falls around 50% to 60% of their ultimate deformation capacity is one of the approaches to create earthquake resistant structures (Gilmore and Cambray, 2009). Since this prototype building is being used as the base for the case study of HED diagrid building presented in next chapter, the preliminary sizes calculated from Eq. (2.5) and (2.6) have been revised and increased based on the nonlinear time history analysis results of the HED diagrid building. The member sizes for the prototype diagrid building are presented in Table 2- 2. All beams and diagonals are rolled steel sections made with structural steel with 345 MPa (50 ksi) minimum yield strength.

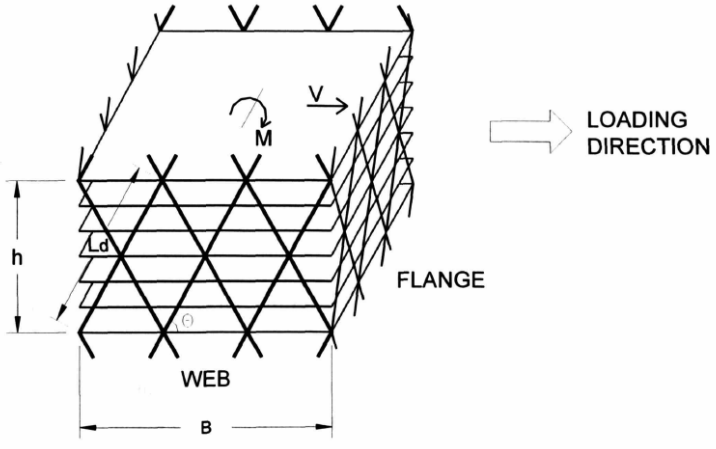

Figure 2- 3. Forces on two modules of a diagrid building (Moon et al., 2007)

Table 2- 1. Calculation of seismic loads for prototype diagrid building

(1) *Level*	(2) *h* (m)	(3) *Δh* (m)	(4) *w* (kN)	(5) *∑w* (kN)	(6) *wh*	(7) *wh/∑wh* □	(8) *Vx(7)* (kN)	(9) *Σ(8)* (kN)	(10) *(3)x(9)* (KN-m)	(11) *Σ(10)* (KN-m)
R	76.8		2624		201582	0.101	265.1			
		3.7		2624				265	970	
21.0	73.2		2335		170832	0.086	224.7			970
		3.7		4960				490	1792	
20.0	69.5		2335		162291	0.081	213.5			2761
		3.7		7295				703	2572	
19.0	65.8		2335		153749	0.077	202.2			5334
		3.7		9630				906	3312	
18.0	62.2		2335		145207	0.073	191.0			8646
		3.7		11966				1096	4011	
17.0	58.5		2335		136666	0.068	179.8			12656
		3.7		14301				1276	4668	
16.0	54.9		2335		128124	0.064	168.5			17324
		3.7		16636				1445	5284	
15.0	51.2		2335		119583	0.060	157.3			22608
		3.7		18972				1602	5860	
14.0	47.5		2335		111041	0.056	146.0			28468
		3.7		21307				1748	6394	
13.0	43.9		2335		102499	0.051	134.8			34862
		3.7		23642				1883	6887	
12.0	40.2		2335		93958	0.047	123.6			41749
		3.7		25977				2006	7339	
11.0	36.6		2335		85416	0.043	112.3			49088
		3.7		28313				2119	7750	
10.0	32.9		2335		76875	0.039	101.1			56838
		3.7		30648				2220	8120	
9.0	29.3		2335		68333	0.034	89.9			64957
		3.7		32983				2310	8448	
8.0	25.6		2335		59791	0.030	78.6			73406
		3.7		35319				2388	8736	
7.0	21.9		2335		51250	0.026	67.4			82142
		3.7		37654				2456	8983	
6.0	18.3		2335		42708	0.021	56.2			91124
		3.7		39989				2512	9188	
5.0	14.6		2335		34166	0.017	44.9			100312
		3.7		42325				2557	9352	
4.0	11.0		2335		25625	0.013	33.7			109665
		3.7		44660				2591	9476	
3.0	7.3		2335		17083	0.009	22.5			119140
		3.7		46995				2613	9558	
2.0	3.7		2335		8542	0.004	11.2			128698
		3.7		49331				2624	9599	
Ground	0.0									138297
∑			**49331**		**1995320**	**1.0**	**2624**		**138297**	

Table 2- 2. Member sizes of the 21-story diagrid building

Story	Structural members (cross sectional area, cm^2)		
	Diagonals	**Beams at the end of module**	**Inter-module beams**
1-6	W33x354 (671)	W36x395 (748)	W36x302 (561)
7-12	W33x263 (484)	W36x330 (594)	W33x263 (445)
13-18	W24x162 (258)	W33x263 (497)	W33x201 (374)
19-21	W24x131 (226)	W24x146 (271)	W24x146 (271)

2.4. Numerical Modeling

The prototype building was modeled as a 2-dimensional frame in OpenSees. OpenSees, the Open System for Earthquake Engineering Simulation was originally developed for general purpose nonlinear finite element analysis of complex structures undergoing inelastic deformations (McKenna 1997). Figure 2- 4 shows a schematic representation of the 21-story diagrid building OpenSees model.

Nonlinear beam-column elements with inelastic fiber sections were used to model all the beams. The diagonal members which are intended to carry the load only through axial action, were modeled with truss elements. The diagonals at the first story were considered rigidly fixed at their base.

Material behavior for all beams and diagonals was modeled using the Giuffre-Menegotto-Pinto model (Menegotto and Pinto, 1973) with isotropic strain hardening of 2% and yield strength of 345 MPa (50 ksi) (ie, Steel02 material in OpenSees).

Floor tributary masses were lumped into the beam end nodes at each floor level. In the planar structural model in OpenSees, half of the total seismic mass was assigned to the planar frame due to symmetry of the building plan.

A lean-on column along the height of the structure shown in Figure 2- 4, consisting of 21 elastic beam-column elements were used in the model to account for the P-Delta effect. The column has the attributes of half of the gravity columns of the diagrid building. The column was connected to the beams of frame at each floor by axially rigid truss elements to transfer the inertia force. The zero-length rotational springs with very small stiffness are used in lean-on column connections to prevent

introducing significant moment in the column. The lean-on column was pinned at its base.

The tributary gravity load of the frame including dead and live loads were applied at each floor level. Half of the load on all gravity columns of the building was assigned to the lean-on column. The seismic load combination based on section 12.4.2.3 of ASCE/SEI 7-10 is:

$$(1.2 + 2S_{DS})D + Q_E + L + 0.2S \tag{2.7}$$

where D, L, Q_E and S denote deal load, live load, earthquake load and snow load, respectively. The live load was considered to be 2.87 kN/m^2 (60 psf).

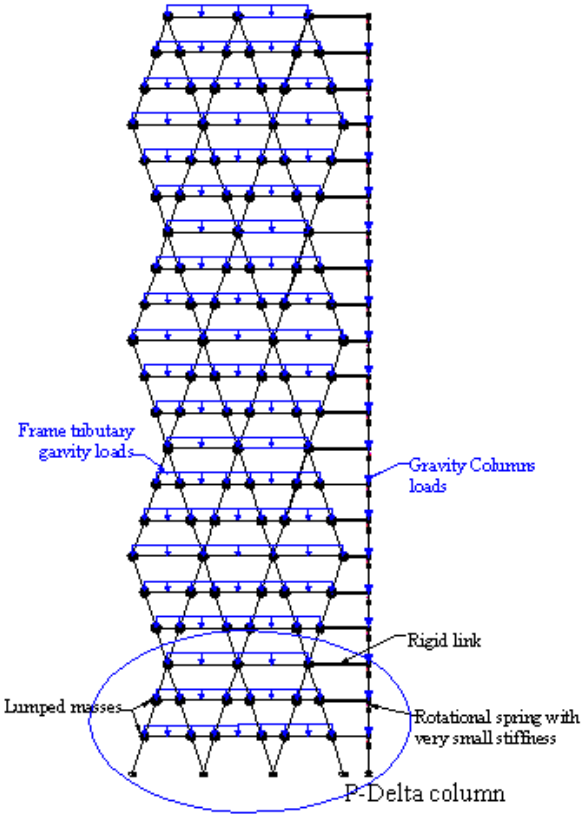

(a)

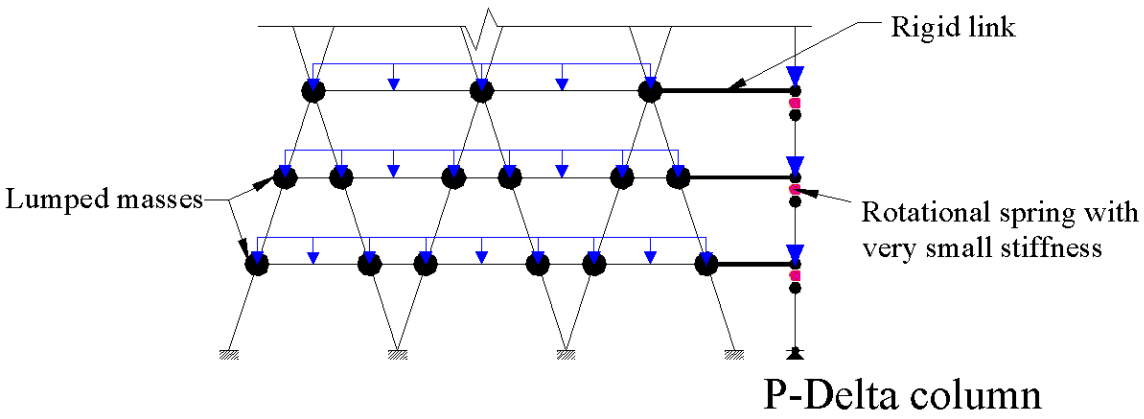

(b)

Figure 2- 4. Schematic of the 21-story diagrid frame OpenSees model: (a) Whole frame; (b) Close-up view

2.5. Eigen Value Analysis

The Eigen value analysis was performed using the model developed in OpenSees. The first three vibration periods of the 21-story HED diagrid building are 2.30, 0.64 and 0.37 seconds, respectively. The corresponding first three mode shapes obtained by nodal Eigenvector command in OpenSees are shown in Figure 2- 5.

If it is assumed that the first mode dominates the seismic response of the structure, the inverted triangular vertical load pattern seems to be appropriate to distribute the base shear along the height of the building in pushover analysis according to the first mode shape of the building.

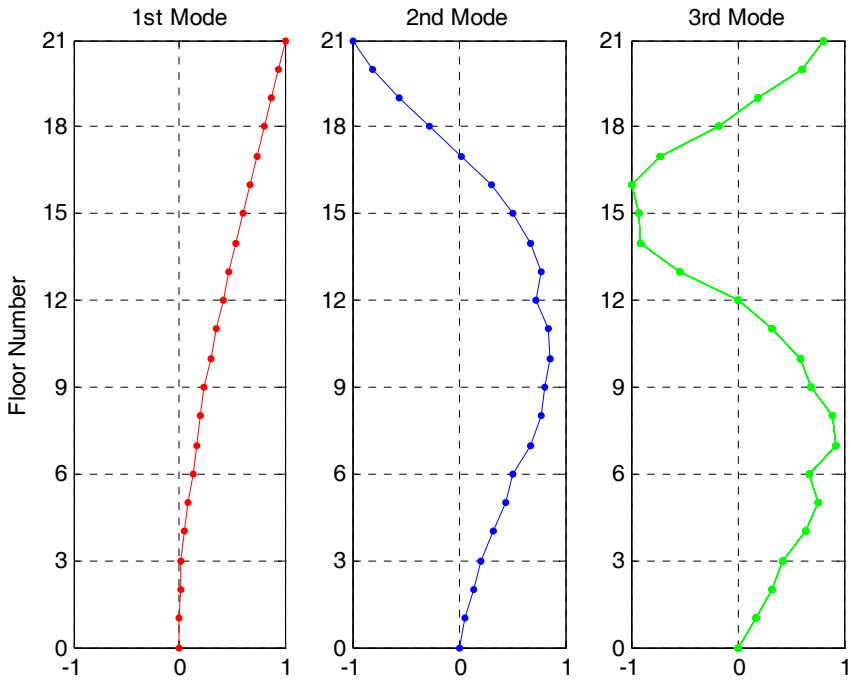

Figure 2- 5. First three mode shapes of 21-story diagrid building

2.6. Nonlinear Static Analysis

In the nonlinear static analysis of the 21-story diagrid building, the inverted triangular lateral load was applied as point forces acting on the leftmost nodes of each floor level as shown in Figure 2- 6. The middle node at the roof level was selected as the control node and the structure was gradually pushed to a target roof drift ratio of 1.5%. The recorded roof drift ratio vs. the normalized base shear of the building, also known as pushover curve is shown in Figure 2- 6. The roof drift ratio is obtained by dividing the roof displacement by the total height of the building. Normalized base shear also known as base shear ratio is the base shear force divided by seismic weight of the building.

The elastic behavior was observed prior to roof drift ratio of 0.74% which corresponds to base shear ratio of 0.115. After this stage, the first diagonal with largest compression load yielded. As the roof drift ratio reached to 1%, about 13% of all the diagonals were already yielded. The ratio of yielded diagonals increased to about 23% once the roof drift ratio reached to 1.5%.

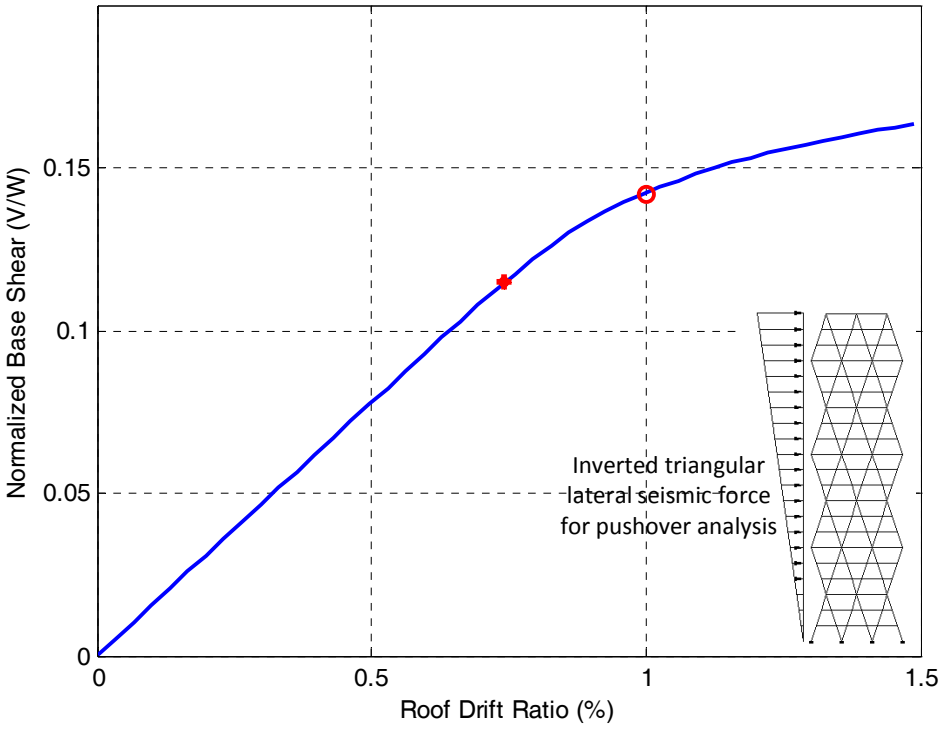

Figure 2- 6. Pushover curve of 21-story diagrid building

2.7. Summary

An introduction to diagrid framing system and its characteristics was presented in this chapter. The structural advantages of diagrid were described and some landmark diagrid designs were introduced to show the great architectural flexibility of the diagrid system in practice. A prototype 21-story diagrid building was designed as a baseline to create the case studies for evaluation of seismic performance of the two other systems presented in Chapters 3 and 6.

The nonlinear static analysis of the prototype building was conducted using a finite element model of the building created in OpenSees. The results showed that at early stage of pushover analysis corresponding to 0.74% of roof drift ratio, the diagonals with the largest axial force yielded. Considerable numbers of diagonals started to yield rapidly as the pushover analysis advanced.

It was shown that once the diagrid frame is deformed post its elastic capacity, failure of the building is anticipated due to yielding of considerable number of diagonals. Therefore low ductility of the diagrid structure makes it vulnerable to large lateral forces (e.g. strong ground motions).

CHAPTER 3 : HIGH ENERGY-DISSIPATIVE DUCTILE (HED) DIAGRID FRAMING SYSTEM

3.1. A New Structural System for Seismic Regions

3.1.1. Introduction

The diagrid system offers a visually appealing and structurally efficient structural system for gravity load bearing. The architectural elegancy of the diagrid structure attributed to its triangular leaning member configuration and high structural redundancy makes this system a desirable choice for tall building design. With the same amount of material use, a higher lateral stiffness may be achieved in the diagrid structure compared to other comparable structural framing systems; however without careful design, the diagrid structure would remain elastic only up to a certain deformation level after that the diagonals start yielding thus causing permanent damage to the primary structural elements (i.e. diagonals that also carry gravity load) as shown in Chapter 2. It is very expensive and intricate to repair and replace these primary structural elements and it is very interrupting to the operation of the building after strong earthquakes.

In this research, a new type of seismic resistant diagrid structural system termed as “Highly Energy-dissipative Ductile (HED) diagrid” is proposed in which the energy dissipation is achieved in dedicated fuse elements and consequently seismic performance has been favorably improved. In the following sections of this chapter the details about this HED diagrid system are presented and the structural

characteristics and seismic behavior (strength, stiffness, energy dissipation, and ductility) of HED diagrid structure are demonstrated with a prototype 21-story building subjected to nonlinear static and dynamic analysis.

3.1.2. Motivations and Objectives

Despite many advantages of diagrid framing system, the lack of a reliable energy dissipation mechanism in concentric diagrid framing has limited its use in seismic active regions. Furthermore, it is quite difficult to fabricate the intersection nodes of the diagrid system due to their complex combination of various diagonal members and beams (Kim et al. 2011). To address these issues, a highly energy-dissipative ductile (HED) diagrid framing design is proposed here which provides a competitive design option in high seismic regions with its high ductility and improved energy dissipation capacity provided by replaceable shear links interconnecting the diagonal members at their nodes. Ductility is defined as the capacity of building materials, systems or structures to absorb energy by deforming into inelastic range (Taranath, 1997). Structural systems with high energy dissipation capacity, ductile deformation behavior and without premature structural failure are desired for seismic applications in high seismic active areas.

The HED diagrid framing system is proposed in this research for high seismic regions with the purpose of accommodating the architectural flexibility and also providing an efficient lateral force resisting structural system. The HED diagrid framing system not only has the aesthetic advantages of diagrid system, but is also easy to construct and repair after strong earthquake shaking.

3.2. HED diagrid Framing System; Concept

The idea of HED diagrid framing system was inspired by diagrid structural system as a visually appealing structure with high elastic stiffness and eccentric braced frame as a ductile lateral force resisting system. Eccentrically braced frames (EBFs) are efficient seismic force resisting system because of their excellent ductility and energy dissipation capacity. In EBF at least one end of every brace is connected to a link element so that the brace force is transmitted through shear and bending of the link (AISC 341-05).

A schematic of the HED diagrid structure is shown in Figure 3- 1. HED diagrid frame consists of modules each of which includes several stories and shear links are placed at the top of each module. The shear links that are located at the outer most sides of the building are referred to as side shear links and the rest of the links are referred to as middle shear links in this study, as shown in Figure 3- 1. The HED diagrid structure takes advantage of diagonal elements as primary load carrying members for both gravity and lateral loads similar to those in conventional diagrid systems, while utilizes shear links connecting the joints of diagonals as seismic fuse elements to realize reliable energy dissipation. Figure 3- 2 shows a schematic of the shear link connection to the diagonals and beams.

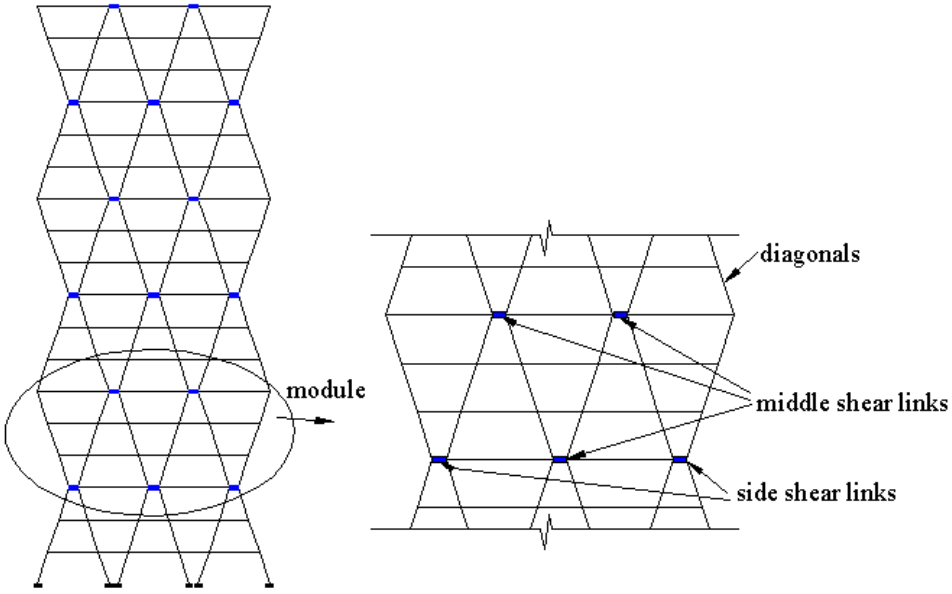

Figure 3- 1. Schematic of HED diagrid framing system: (a) Elevation; (b) Close-up view

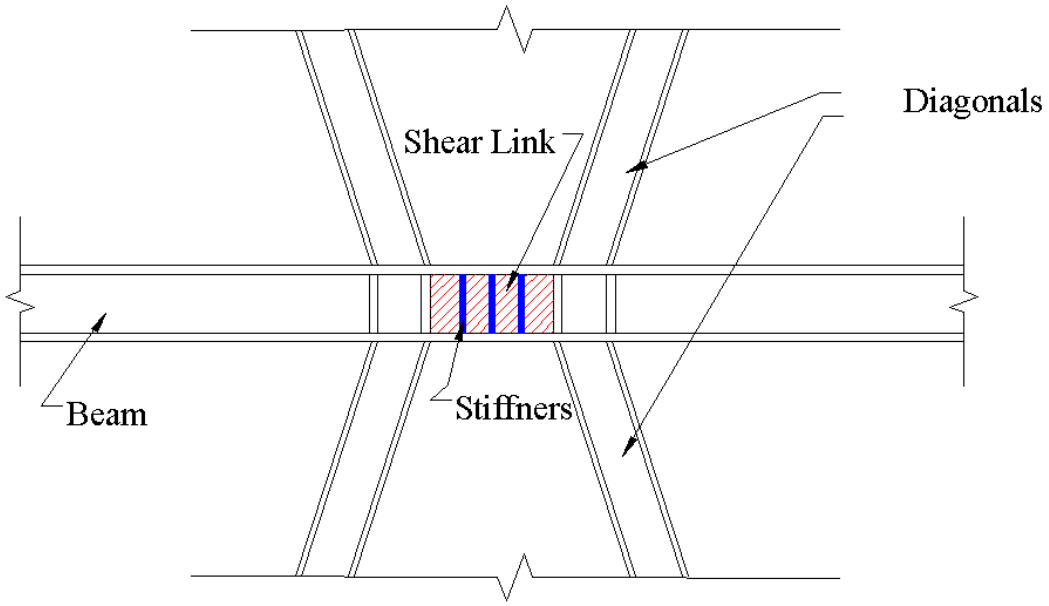

Figure 3- 2. Schematic of shear link connection to diagonals and beams

The seismic design philosophy is based on keeping the structure elastic or slightly inelastic during minor to moderate earthquakes and preventing them from collapse during severe earthquakes. The HED diagrid system features relatively large lateral stiffness due to its angular configuration as well as high energy dissipation capacity enabled by its shear links. Its lateral stiffness limits displacements during minor and moderate earthquakes, while the inelastic deformation of the shear links is intended to dissipate energy as ductile structural fuses. These shear links thus limit the force transferred to the primary structural members such as diagonals and prevent them from getting into plastic phase. The stiffness and strength of the HED diagrid structure can be controlled and tuned by proper design of shear links.

In addition to appealing structural performance under strong earthquakes, the HED diagrid structure has several other advantages. The shear links are easy to replace and they will not fail before experiencing large deformations (Mansour *et al.* 2008). By using the replaceable links, welding of the critical structural elements are done in the shop, hence improving construction quality and reducing erection time. The inspection and replacement of the damaged links following a major earthquake is easy and quick, thus significantly minimizing the disruption time of the structure. Furthermore, using shear links solves the challenge of connection design in conventional diagrid structure design since the diagonals do not join concurrently in the HED diagrid system. The HED diagrid structures are very effective in providing flexural rigidity since they carry shear and bending through the axial action of the diagonal members, thus minimizing the lateral displacement.

The cyclic shear yielding of a link element is an excellent energy dissipation mechanism since the link can undergo large inelastic deformations before failure occurs. If the flange and web local buckling are prevented in a link element through appropriate stiffeners, the failure of the link ultimately occurs by material rupture in the web or flange depending on type of the link. Shear is the dominant failure mode in short links while higher moment is developed in long links making flexure the dominating failure mode. In shear links, yielding occurs over a large segment of the web and is followed by a cyclic diagonal field (Taranath, 1997). After the web yielding, the load is carried by the tension field resulting in fat hysteresis loops representing good energy dissipation. In the HED diagrid system, the link elements are designed with short length to behave as shear links which effectively dissipate energy once the loads from each load path of diagonals are transferred to them.

3.3. Case Study

Nonlinear analysis of a sample HED diagrid building under design basis earthquake is required to assess the seismic performance of the proposed system. The 21-story building presented in Chapter 2 was used as the preliminary design for the prototype HED diagrid building to be analyzed in this chapter. The 3x3 bay building is 76.81 m (252 ft) tall, and 26.5 x 26.5 m (87 x 87 ft) in plan as shown in Figure 3- 3. The diagonals have the slope of 72 degrees. All the shear links were selected to be 1.0 m (40 inch) long. The height of the building is similar to prototype diagrid building and the height to width ratio of the HED diagrid building is 2.9.

The seismic weight of the 21-story HED diagrid building is 122,000 kN (27,500 kips). The seismic weight for a typical floor is 5780 kN (1300 kips), based on 6.7 kN/m^2 (140 psf) for the floors and 1.44 kN/m^2 (30 psf) for the façade. The seismic weight for the roof is 6450 kN (1450 kips), considering 670 kN for rooftop equipment. The floor mass distribution along the building height is considered to be uniform.

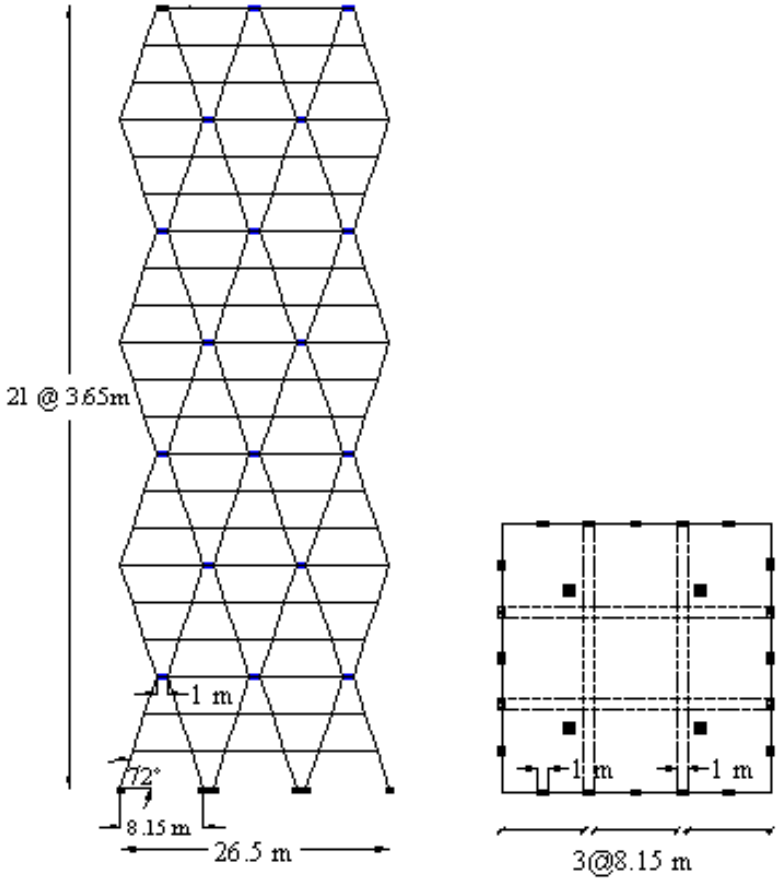

(a) **(b)**

Figure 3- 3. The prototype HED diagrid building: (a) Elevation; (b) Plan

3.4. Structural Design for Case Study Building

3.4.1. Design Provisions

The nominal shear strength of a link in AISC seismic provisions (ANSI/AISC 341-05) is computed as:

$$V_n = V_p \text{ ; if } e \leq \frac{2M_p}{V_p} \tag{3.1}$$

$$V_n = \frac{2M_p}{e} \text{ ; if } e > \frac{2M_p}{V_p} \tag{3.2}$$

where e is the length of the link. The plastic shear and moment capacity of a link, M_p and V_p, are determined from the following equations (ANSI/AISC 341-05):

$$V_p = 0.6A_{web}\sigma_y \tag{3.3}$$

$$M_p = Z\sigma_y \tag{3.4}$$

where σ_y is the yield strength of the shear link material and A_{web} and Z are the web cross sectional area of the link and plastic modulus of the link cross section, respectively.

Links with different sizes and material properties show different yielding behaviors. Yielding in shear extended over the full length of the link or in flexure at the link ends, or a combination of both shear and flexural yielding may be anticipated for a link element. AISC seismic provisions (ANSI/AISC 341-05) defines three types

of link elements with the following criteria for length ranges and allowable link inelastic rotation angles. A link member is considered short with shear yielding behavior if its length, *e*, is below the following limit:

$$e \leq \frac{1.6M_p}{V_p} \tag{3.5}$$

The allowable link inelastic rotation angle for short links is 0.08 radians. A link member is considered long with flexural yielding behavior if its length, *e*, is larger than the following limit:

$$e \geq \frac{2.6M_p}{V_p} \tag{3.6}$$

The allowable link inelastic rotation angle for long links is 0.02 radians. The link is categorized as intermediate if its length is between the two above mentioned limits:

$$\frac{1.6M_p}{V_p} < e < \frac{2.6M_p}{V_p} \tag{3.7}$$

The allowable link inelastic rotation for an intermediate link can be calculated from the interpolation between 0.02 and 0.08 radians.

To limit the local buckling the link cross section shall meet the seismically compact cross section requirements. The Flanges should be continuously connected to the web and the width-thickness ratios of flanges should be less than the limiting value, λ_{ps}:

$$\frac{b_f}{t_f} < \lambda_{ps} = 0.38\sqrt{\frac{E}{\sigma_y}} \tag{3.8}$$

In the above equation, E is the Young's modulus of the link material. Lateral bracing are required at both the top and bottom link flanges at the ends of the link. The effect of axial force on the link's shear capacity needs to be considered if:

$$\frac{P_u}{P_y} > 0.15 \tag{3.9}$$

where P_u is the required axial strength and $P_y = \sigma_y A_g$ is the nominal axial strength of the link (A_g is the total cross-sectional area of the link). It was found that for the 21-story HED diagrid building, the side links of the 1st, 3rd and 5th modules experience high axial forces. These side links are connected only to the diagonals at one side and hence the horizontal resultant force of diagonals is directly transferred to the shear link. For these shear links, the area of the flanges on the were increased to decrease the axial force ratio without changing the shear capacity of the links which is affected only by web area and not the flange.

The diagonals and beams are subjected to large axial forces and bending moments generated by the yielded link. It is essential that all structural elements other than links remain elastic. The beams and diagonals should be designed strong enough to make the links the weakest part of the system which allows them to yield and dissipate energy as the fuse elements. The diagonals of the HED diagrid building have the same sizes as prototype diagrid building in Chapter 2. Larger beams are required in HED diagrid frame so that they remain elastic under the large forces transferred from the shear links.

3.4.2. Sizing of Structural Elements and Capacity of the links

Table 3- 1 shows sizes of the diagonals and beams of the 21-story HED diagrid building and the shear capacity of the links. The length and capacity of shear links were designed and checked according to the Seismic Provisions for Structural Steel Buildings, ANSI/AISC 341-05 described in previous section. All the beams, diagonals and shear links are rolled steel sections made with structural steel with 345 MPa (50 ksi) minimum yield strength.

It is assumed that appropriate full-depth web stiffeners are used in the links to prevent web and flange local buckling. In the modules with three shear links, the side shear links were intentionally assigned with lower shear capacity than the center link since shear force at the center link is much larger; in doing so, their different shear strengths enables them to start plastic deformation and thus energy dissipation simultaneously. This can be illustrated by considering the diagrid structure as a vertical cantilever beam which has the maximum shear stress at its neutral axis. Under lateral loading the center line of the diagrid frame acts like the neutral axis of a cantilever beam and has the highest shear stresses. The shear links at the first and second modules were designed with higher shear capacity compared to the links at higher modules to reduce the residual displacement of the structure under earthquake loading since they undergo larger plastic deformations. At the roof level, the HED diagrid building is not exposed to much shear forces and hence the center shear link at the last module have lower capacity compared to the ones at lower modules.

Table 3- 1. Size and capacity of the 21-story HED diagrid building structural members

Story	Member Sizes (cross sectional area, cm^2)		Shear links design strength (kN)	
	Diagonals	**Beams**	**Middle**	**Sides**
1-6	W33x354(654)	W40x503(935)	7518	5370
7-12	W33x263 (484)	W40x397(742)	6513	3256
13-18	W24x162 (258)	W40x397(742)	6513	3256
19-21	W24x131 (226)	W36x256(458)	3256	3256

3.5. Numerical Modeling

3.5.1. Introduction

A nonlinear finite element model of the case study HED diagrid building is required to investigate its seismic performance under earthquake loading. Therefore, a two-dimensional model of the building was developed in this study using the computer program OpenSees. This general finite element analysis platform has a very large library of various finite elements for use in modeling the structure, however, it does not presently have a built-in element for modeling the links.

Accurate modeling of the HED diagrid structure and specifically the shear links are very critical to the seismic performance evaluation since the inelastic deformation of the HED diagrid structure is confined to these shear yielding links while other members are supposedly to remain linear elastic during design level earthquakes. Therefore in this research a special element that simulates the real behavior of the links was also developed in OpenSees.

3.5.2. Shear Link Model

In short links, shear is the dominating force which is mainly carried by the web and small bending moments also develop at the ends of the link. In the model presented by Ramadan and Ghobarah (1995) which is adapted from the model originally developed by Ricles and Popov (1987 a and b), one elastic beam-column element and two hinges at the ends to capture the inelastic behavior were used to represent the link element. In this study, shear link is modeled using three elements as shown in Figure 3- 4: two zero length elements at two ends of shear link which account for yielding in shear, and one beam element in the middle which accounts for elastic axial, bending and shear deformations and yielding in bending.

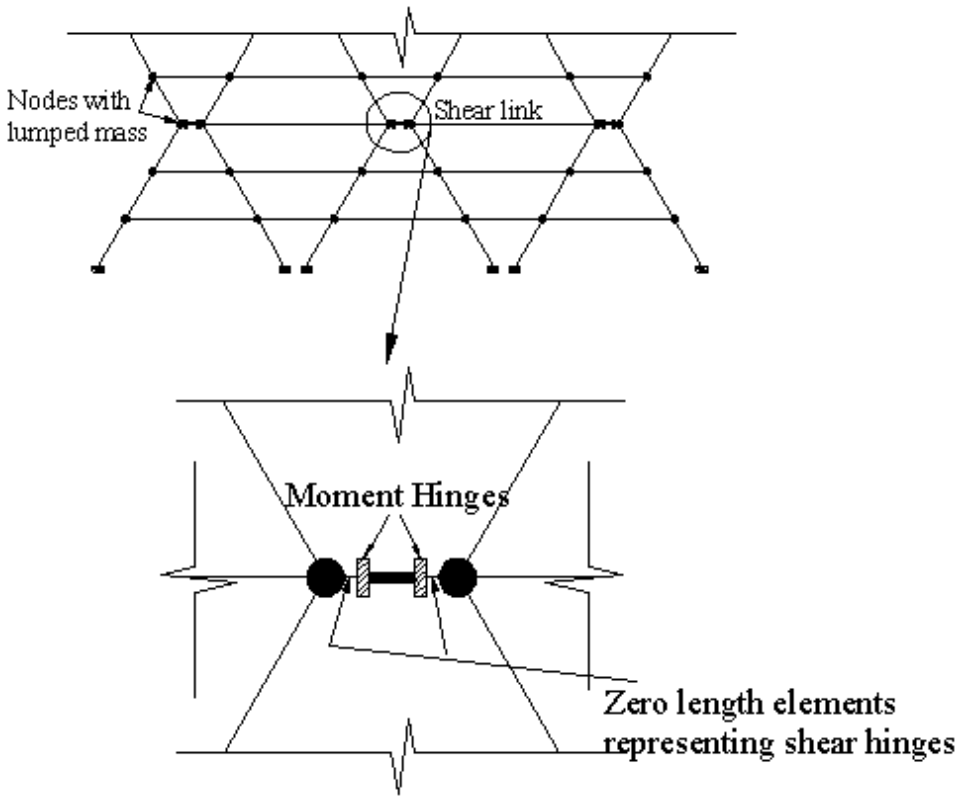

Figure 3- 4. Components of shear link element

The middle beam used in the link model is an OpenSees element called "beam with hinges". This element is comprised of three parts: two hinges at the ends, and a linear-elastic region in the middle (see schematics in Figure 3- 5). The plastic hinging is localized at the element ends through those two hinges defined by assigning to each a prescribed M-θ relation to account for yielding in bending. These lumped plasticity parts (i.e. moment hinges) have zero length and bilinear material (Mazzoni *et al.*, 2009) with yield strength equal to the nominal moment strength of each shear link in order to represent the flexural behavior of the links. The moment developed in the shear links are supposed to be lower than their moment capacity since the links are shear critical. To ensure that the moment developed in the links is below the elastic moment capacity of the link, the moment-rotation response of the moment hinges were recorded during analysis.

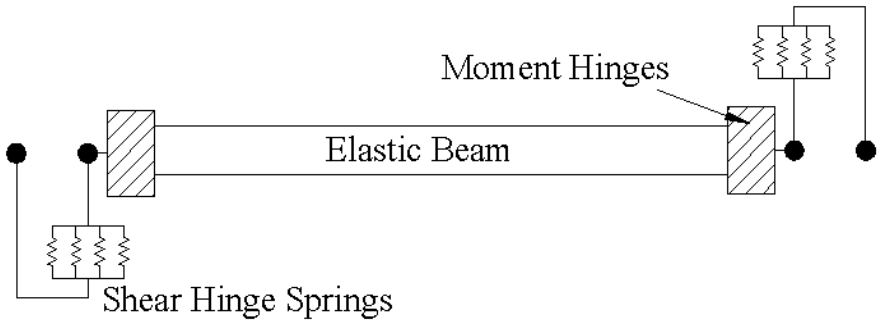

Figure 3- 5. Link element model

The shear link behavior observed in experimental tests, can be divided into three distinct phases: the elastic behavior up to the shear force of V_1; plastic phase before significant local buckling at V_{max}; and the degradation phase which is usually short

and occurs when link rotation is larger than link inelastic capacity resulting in failure of the link by rupture of web section (Okazaki *et al.*, 2006). The short links with tight web stiffener spacing are not prone to local buckling and do not experience degradation (Richards and Uang, 2005). Based on the assumption of proper full-depth web stiffeners for shear links, the shear deformation corresponding to link rotation of 0.08 radians which is the value specified in the code for shear link rotation limitation, is considered as the failure rotation limit of the shear links.

The measured value of V_1 in the test results of Okazaki et al. (2005) was typically equal to or somewhat larger than its nominal value (based on nominal dimensions and nominal yield strength). Based on the described experimental results, the piecewise linear model proposed by Richards (2004) was used to model the links shear behavior. The force-deformation relation of this model is shown in Figure 3- 6. The corresponding shear forces and stiffness on the link's shear force-deformation curves shown in Figure 3- 6 are as follows (Richards, 2004):

$$V_1 = 1.1V_p \tag{3.10}$$

$$V_2 = 1.36V_p \tag{3.11}$$

$$V_3 = 1.5V_p \tag{3.12}$$

The stiffness of each linear part of the link's shear force-deformation curve are calculated as (Ramadan and Ghobarah, 1995; Richards, 2004):

$$K_{v1} = 2GA_{web}/e \tag{3.13}$$

$$K_{v2} = 0.03K_{v1} \tag{3.14}$$

$$K_{v3} = 0.015K_{v1} \tag{3.15}$$

$$K_{v4} = 0.002K_{v1} \tag{3.16}$$

where G is shear modulus of the link material.

Four parallel springs with isotropic bilinear behavior were used to model the shear hinges at both ends of the link element. Elastic-perfectly-plastic material is used to model the hysteretic behavior of four springs connected in parallel, which are represented with zero-length elements at the ends of the link to simulate the piecewise-linear shear behavior of the shear link.

The accuracy of the shear link analytical model and its parameters is verified by the experimental data from the study of Hjelmstad and Popov (1983) and Okazaki and Englehardt (2007). In the experimental research conducted by Okazaki and Englehardt (2007), a total number of thirty seven links with different length were tested under cyclic loading.

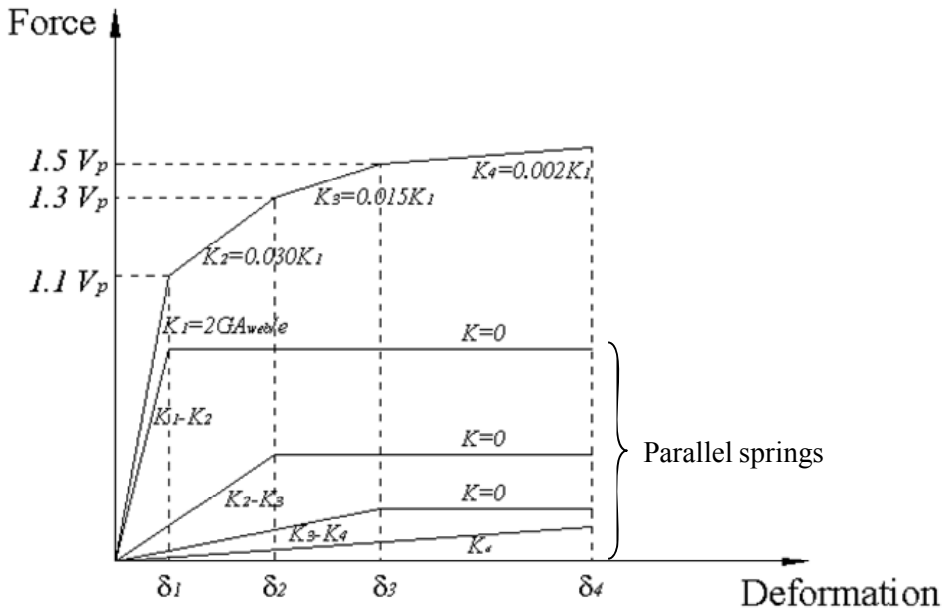

G is shear modulus of the link material.

Figure 3- 6. Combined behavior of parallel springs used to model shear hinge based on the model proposed by Richards (Richards, 2004)

3.5.3. Elements and Constraints

With the shear link model being established, the 21-story HED diagrid building was modeled as a two-dimensional planar structure in the OpenSees software. Figure 3- 7 (a) and (b) show a schematic representation of the 21-story HED diagrid building OpenSees model.

Nonlinear beam-column elements with inelastic fiber sections were used to model all the beams. The diagonal members which are intended to carry the load only through axial action were modeled with truss elements. The diagonals at the first story were considered fixed at their base.

A lean-on column along the height of the structure, consisting of 21 elastic beam-column elements similar to what described in Section 2.3 was used in the

model to account for the P-Delta effect. The lean-on column was connected to the main frame by axially rigid truss elements as shown in Figure 3- 7.

3.5.4. Material and Mass

Material behavior for all elements was modeled using the Giuffre-Menegotto-Pinto model (Menegotto and Pinto, 1973) with 2% isotropic strain hardening and yield strength of 345 MPa (50 ksi) (ie, Steel02 material in OpenSees).

Floor masses were lumped into the beam end nodes at each floor level. In the planar structural model in OpenSees, half of the total seismic mass was assigned to the planar frame due to symmetry of the building plan. The tributary gravity load share of the frame including deal and live loads were applied at each floor. Half of the load on all gravity columns of the building was also assigned to the lean-on column. The load combination presented in Eq. (2.7) was used to calculate the gravity loads and the live load was considered to be 2.87 kN/m^2 (60 psf).

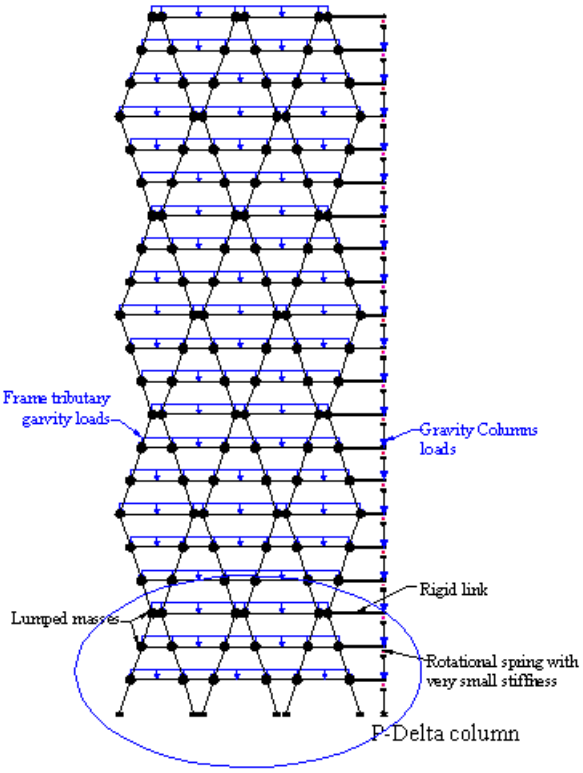

(a)

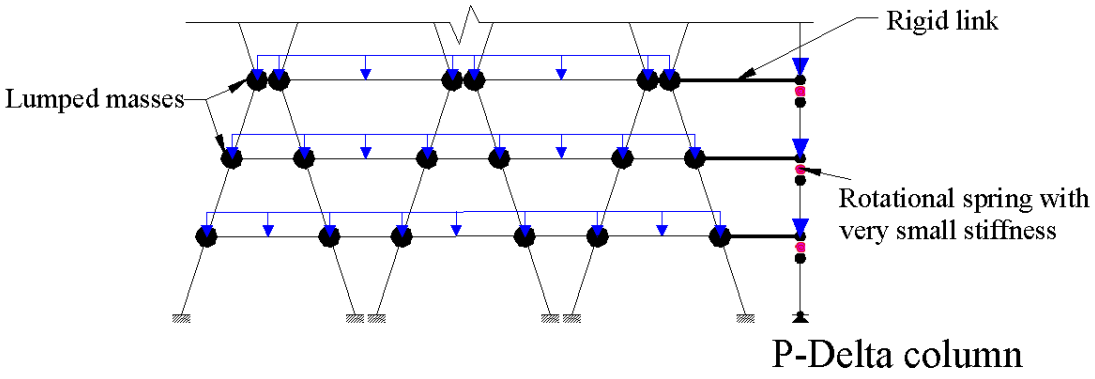

(b)

Figure 3- 7. Schematic of the 21-story HED diagrid frame OpenSees model: (a) Whole frame; (b) Close-up view

3.6. Eigen Value Analysis

The vibration periods and mode shapes of the prototype building was obtained by conducting the Eigen value analysis in OpenSees. The first three vibration periods of the 21-story HED diagrid building are 2.48, 0.8 and 0.46 seconds respectively, and the corresponding first three mode shapes are shown in Figure 3- 8.

The inverted triangular vertical load pattern seems to be appropriate to distribute the base shear along the height of the building in pushover analysis according to the first mode shape of the building, if the first mode dominates the seismic response.

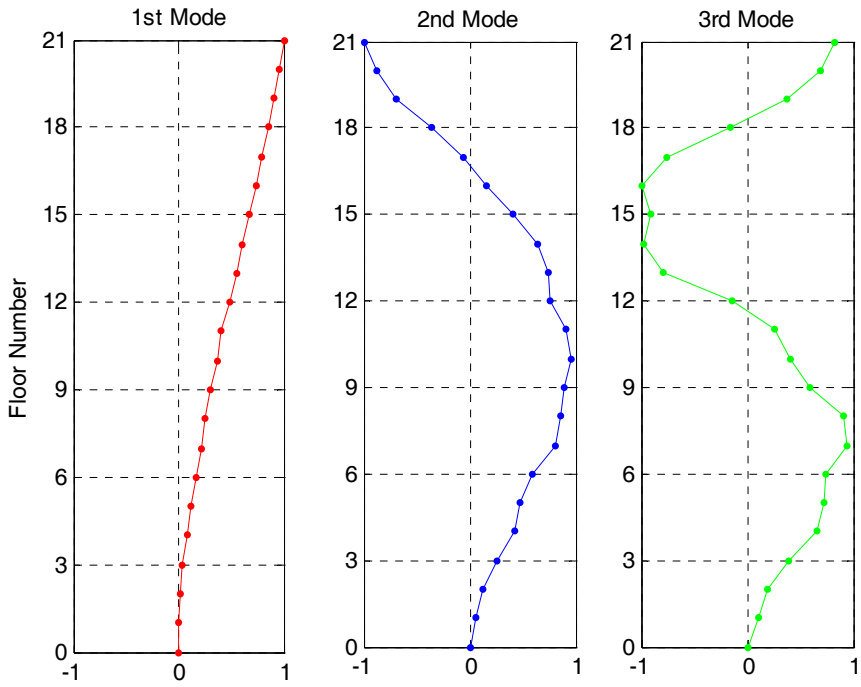

Figure 3- 8. First three mode shapes of the 21-story HED diagrid building

3.7. Nonlinear Static Analysis

Nonlinear static analysis may not be accurate for tall buildings, but it provides a helpful insight into the expected performance of the structure. A pushover analysis of the 21-story HED diagrid building was performed to identify the force-deformation response of the HED diagrid frame. The aforementioned inverted triangular lateral load profile was used as lateral load pattern. The lateral loads were applied as lumped forces at left most exterior nodes at each floor level. The loads were increased monotonically until the horizontal displacement at the roof reached to the drift ratio of 3%.

The roof drift ratio (roof displacement divided by height of the building) vs. the normalized base shear response recorded during the nonlinear static analysis is presented in Figure 3- 9. The force-displacement result of pushover analysis of the HED diagrid building is a piecewise linear curve labeled with Points Y1, Y2, Y3 and Y4 in Figure 3- 9 to show the sequence of the plastic deformation development in the shear links.

It is seen that the slope of the post yield branch of the pushover curve changes as the shear links enter different phases of their inelastic force-displacement relations shown in Figure 3- 6. One purpose of nonlinear static analysis is to provide information on deformation demands for elements that have to deform inelastically in order to dissipate seismically-induced energy (Krawinkler and Seneviratna 1998). During the analysis, the base shear increases linearly until the roof drift ratio reaches about 0.63% and the base shear ratio reaches to 0.087% (Point Y1 in Figure 3- 9).

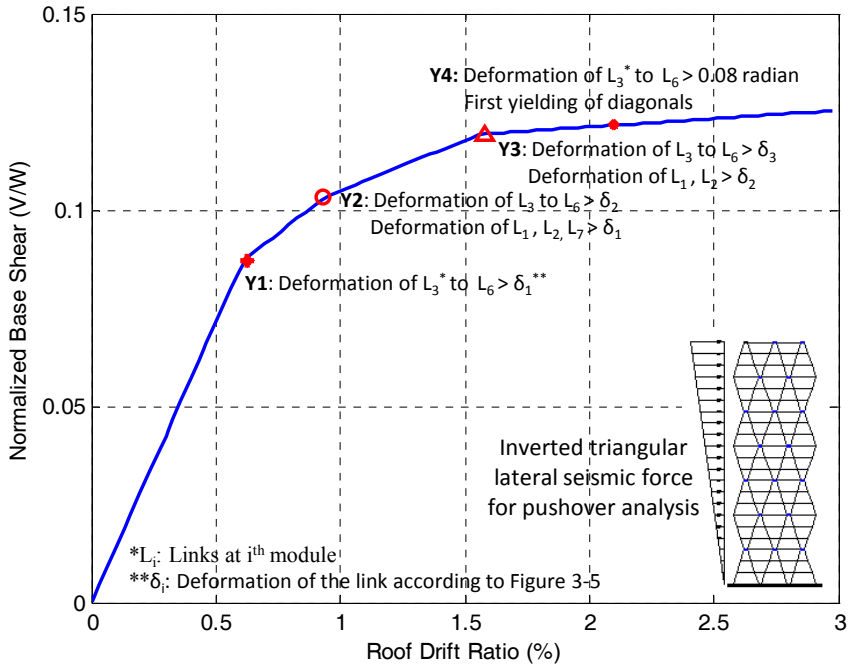

Figure 3- 9. Push-over curve of the 21-story HED diagrid building

The web shear yielding of the shear links of the 3rd to 6th diagrid modules (L_3, L_4, L_5 and L_6) start at 0.63% of the roof drift ratio. At roof drift ratio of 0.93% (Point Y2) and 1.58% (Point Y3), the deformation of these shear links exceeds δ_2 and δ_3, respectively, which correspond to the end of the first and second post-yield branch of the link's force-deformation curve (see Figure 3- 6). The web shear yielding of the links at the 1st, 2nd and 7th modules also start at a roof drift ratio of 0.93%. At roof drift ratio of 1.58%, the deformation of shear links at 1st and 2nd modules exceeds δ_2. It can be seen that inelastic deformation of the shear links is distributed throughout the height of the HED diagrid structure.

All the diagonals and beams remain elastic during pushover analysis up to the roof drift ratio of 2.1% (Point Y4 in Figure 3- 9). At this point, first yielding of the diagonals also occured.

3.8. Nonlinear Time History Analysis

3.8.1. Introduction

The performance of a structural system under strong earthquakes can be evaluated by comparing the nonlinear time history analysis results of the key engineering demand parameters (EDPs) with code specified values and what is generally accepted in practice. For this purpose, nonlinear time history analysis of the 21-story HED diagrid structure is performed under a suite of 14 strong earthquake records.

The same finite element model used for the nonlinear static analysis was used to investigate the response of HED diagrid frame. The Newark average-acceleration (γ=1/2, β=1/4) time-step integration method with Newton initial stiffness interaction was used to solve the dynamic differential equations.

Damping effect for transient analysis was considered through Rayleigh damping. As a typical value for steel buildings, a 2% damping ratio for the first and third modal frequencies of the HED diagrid building were used for the Rayleigh damping parameters in the OpenSees model. The stiffness proportional damping was applied only to the frame elements through combining the region command and Rayleigh command, since for accurate analysis no stiffness damping should be considered for the lean-on column and highly rigid truss elements that link the frame and lean-on column (Zareian and Medina, 2010).

The results of the structural members ductility demand, roof displacement and drift ratio, residual roof drift ratio, inter-story drift ratio, residual inter-story drift ratio, links deformation demand, peak base shear ratio and floor acceleration response

are presented in this section. Since it is not possible to present all detailed results of the time history analysis for all 14 ground motion records, LA18 is chosen as a representative case for the nonlinear time history analysis and some of the detailed time history analysis results are presented for this earthquake record here.

In the results presented in following sections, the "peak" result refers to the highest absolute value of the specified parameter (e.g. ductility demand, inter-story drift ratio, etc.) recorded during the time history analysis. The "ensemble average" refers to the mathematical average value of the results obtained from 14 time history analyses. This value is shown in some figures with the dark circles that are connected with a line.

3.8.2. Selected Ground Motions

The ground motions for this research were selected from the strong earthquake records originally developed by Somerville *et al.* (1997) for the Los Angeles, California region with a probability of exceedance of 10% in 50 years. These scaled earthquake records correspond to the design basis earthquake of the downtown Los Angeles area. Details of these earthquake records are listed in Table 3- 2 . The sampling interval for the all time history analyses was 0.02 second.

Plots in Figure 3- 10 show the acceleration time history of the selected earthquake records. Figure 3- 11 shows the target and the ground motions response spectrum with 5% damping.

Table 3- 2. Earthquake records used for time history analysis

	Record	Earthquake Magnitude	Distance to Epicenter (km)	Duration (second)	PGA (g)
LA01	Imperial Valley, 1940, El Centro	6.9	10	53.48	0.46
LA02	Imperial Valley, 1940, El Centro	6.9	10	53.48	0.68
LA07	Landers, 1992, Barstow	7.3	36	79.98	0.42
LA08	Landers, 1992, Barstow	7.3	36	79.98	0.43
LA09	Landers, 1992, Yermo	7.3	25	79.98	0.60
LA10	Landers, 1992, Yermo	7.3	25	79.98	0.36
LA11	Loma Prieta, 1989, Gilroy	7.0	12	39.98	0.67
LA12	Loma Prieta, 1989, Gilroy	7.0	12	39.98	0.97
LA13	Northridge, 1994, Newhall	6.7	6.7	59.98	0.68
LA14	Northridge, 1994, Newhall	6.7	6.7	59.98	0.66
LA17	Northridge, 1994, Sylmar	6.7	6.4	59.98	0.57
LA18	Northridge, 1994, Sylmar	6.7	6.4	59.98	0.82
LA19	North Palm Springs, 1986	6.0	6.7	59.98	1.02
LA20	North Palm Springs, 1986	6.0	6.7	59.98	0.97

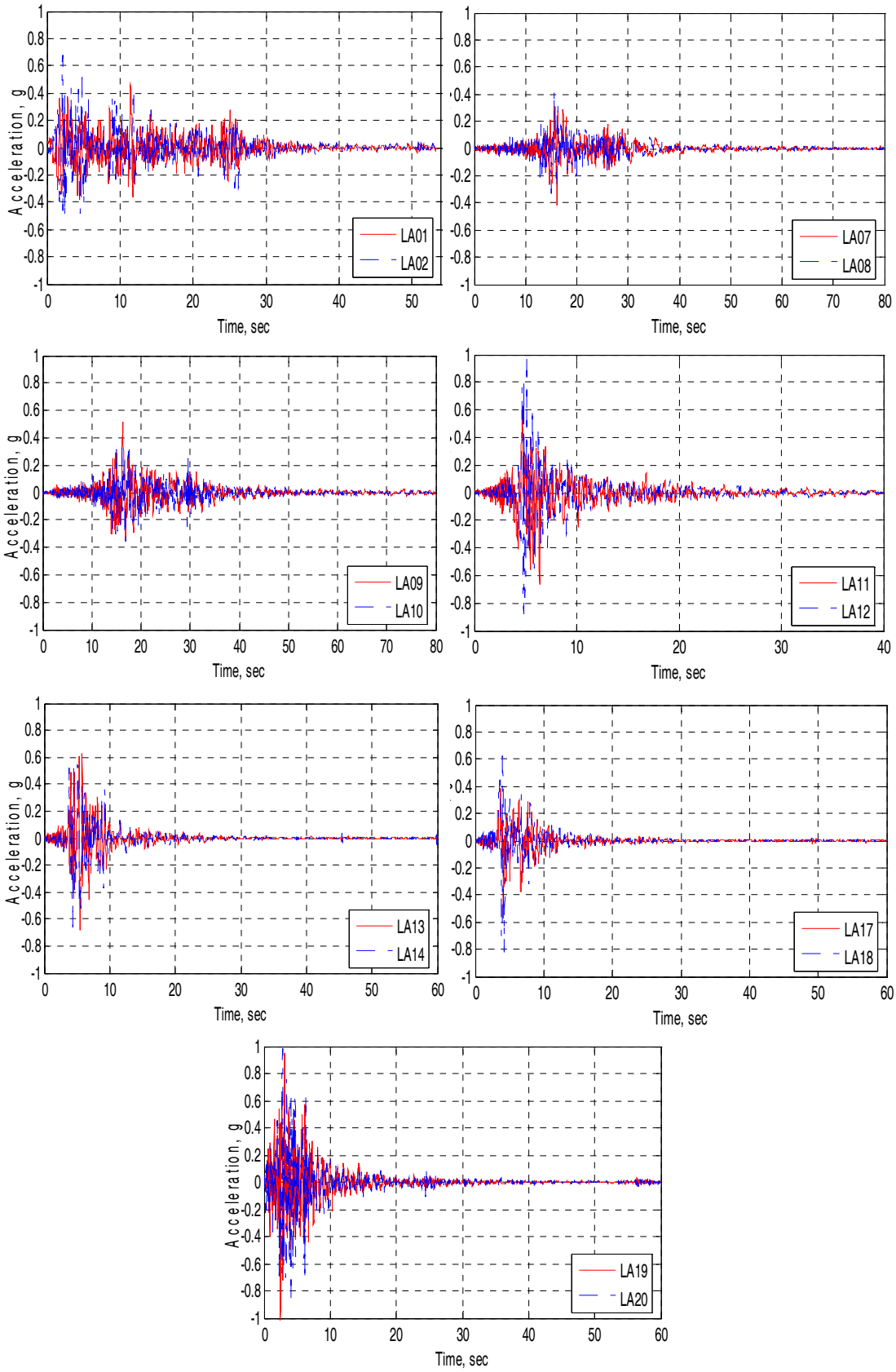

Figure 3- 10. Acceleration time history of the 14 selected ground motions

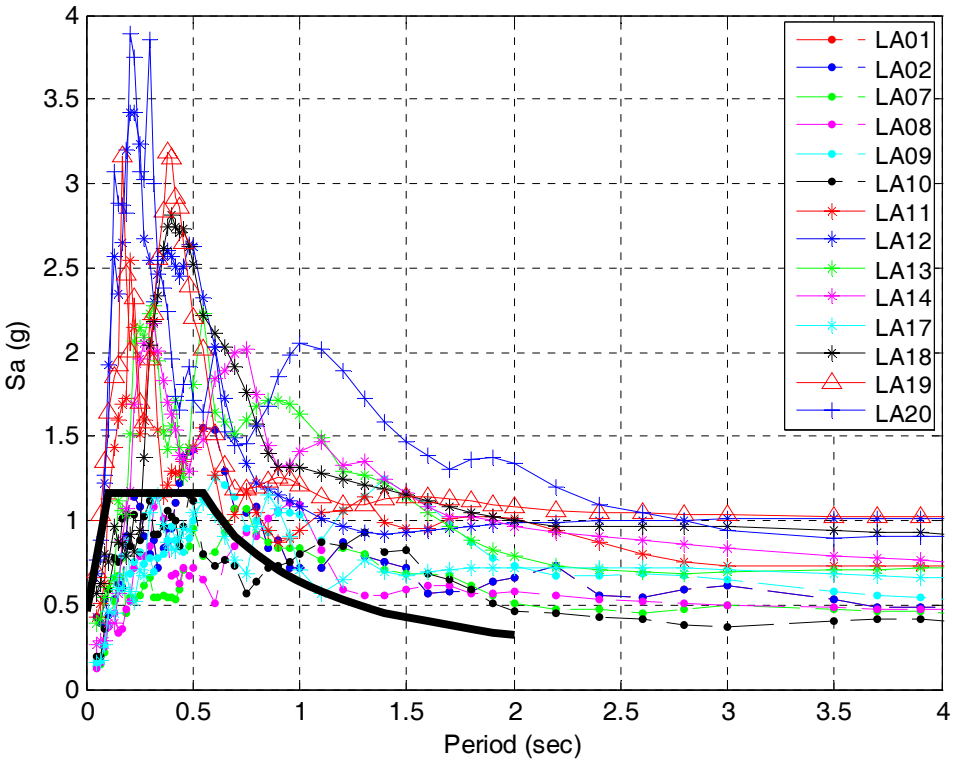

Figure 3- 11. Design spectra and individual earthquake spectra

3.8.3. Structural Members Ductility Demands

One of the main purposes of seismic design is to keep the main structural elements elastic during the earthquake. The force and displacement of all beams and diagonals were recorded during the time history analyses and the maximum ductility demand of diagonals of each story were calculated. The ductility demand for diagonals are calculated by the following equations:

$$\mu = \frac{d_m}{d_y} \tag{3.17}$$

where d_m is the maximum axial displacement demand and d_y is the yield axial displacement of the steel diagonals.

To calculate the ductility demands of diagonals, the force-deformation response of all diagonals were recorded during the time history analysis and peak axial displacement imposed on diagonals of each story was identified by a post-processing code developed in MATLAB (Mathworks Inc.). Consequently the peak ductility demand of diagonals of each story were calculated under individual ground motions and the average of ensemble of results under 14 ground motions were calculated.

Figure 3- 12 shows the peak ductility demand of diagonals of each story under each earthquake record. All the diagonals were remained elastic under all 14 earthquake records since the value of ductility demand is less than one for diagonals of all stories. The ensemble average peak ductility demand at each story is shown with dark circles connected with a line in Figure 3- 12 with the maximum value of 0.88 at 13th story. The maximum ductility demand of 0.98 was recorded under LA12 at 1st story diagonal.

The maximum stress on all beams were checked and it was insured that they all remained elastic during all 14 time history analyses for all case studies.

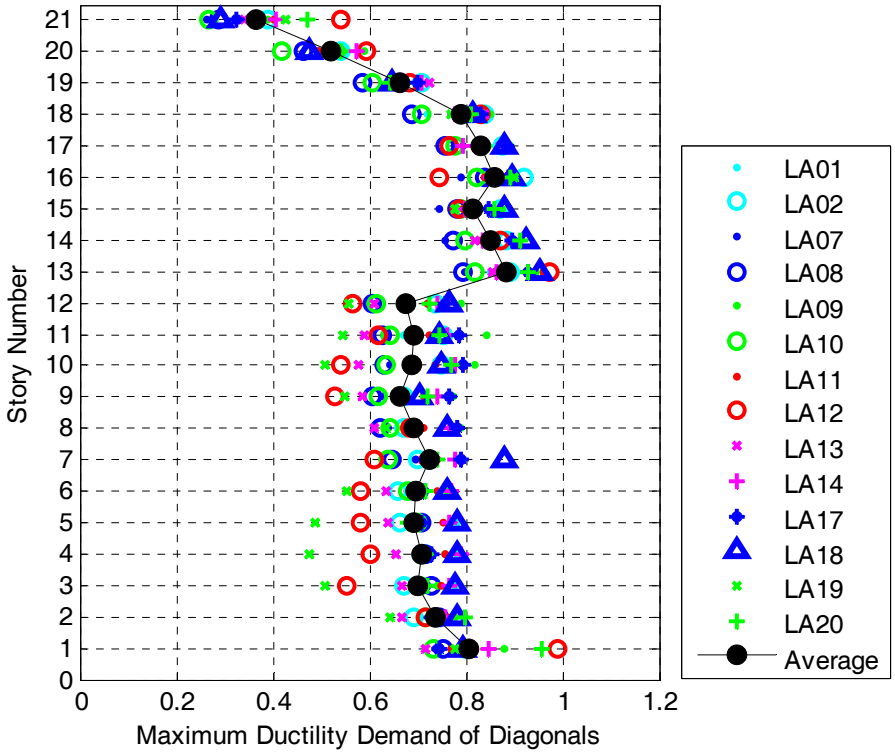

Figure 3- 12. Maximum ductility demand of diagonals of 21-story HED diagrid building under a set of 14 ground motion records

3.8.4. Global Deformation Demands

Figure 3- 13 to Figure 3- 19 show the roof drift ratio (roof displacement divided by the total height of the building) history of the 21-story HED diagrid building under 14 earthquake records.

Figure 3- 20 shows the displacement time histories of the roof, 12th and 3rd floors of the HED diagrid building subjected to the LA18 ground motion. It can be seen that the value of residual displacements are fairly small.

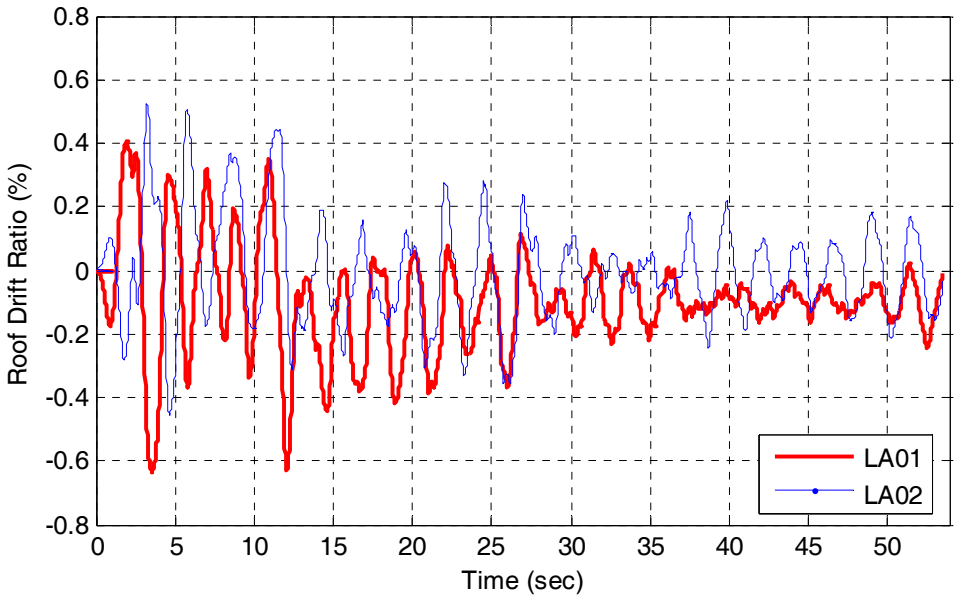

Figure 3- 13. Roof drift ratio time history of 21-story HED diagrid building under LA01 and LA02

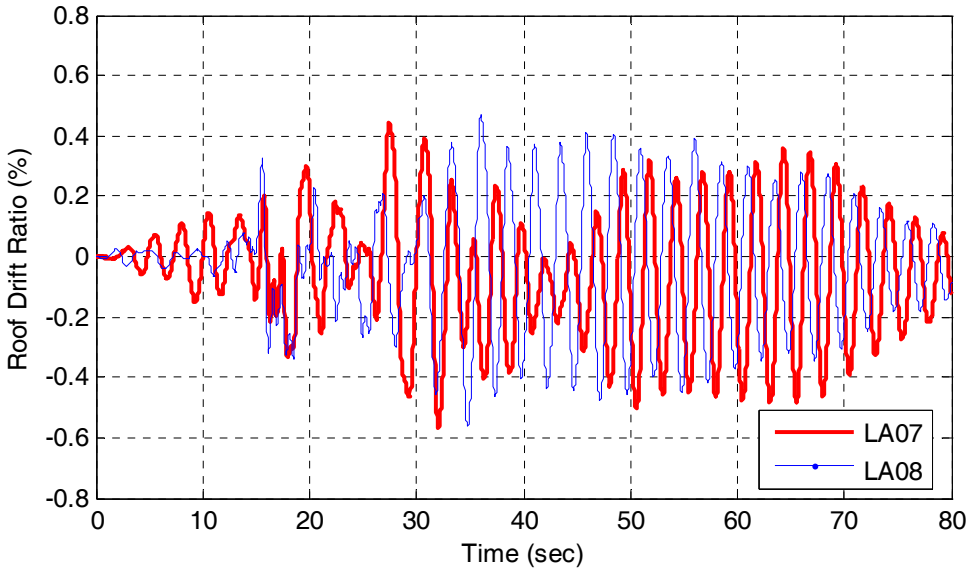

Figure 3- 14. Roof drift ratio time history of 21-story HED diagrid building under LA07 and LA08

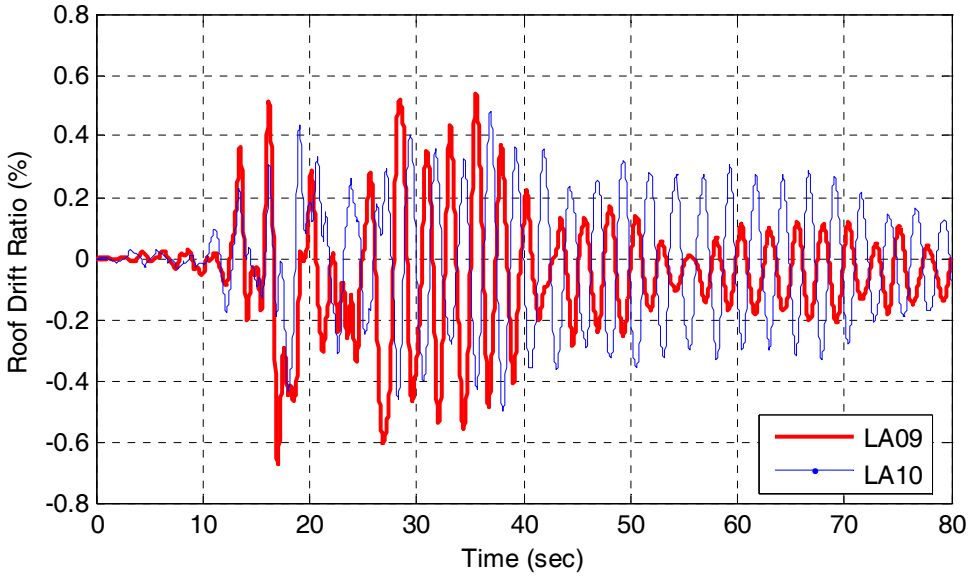

Figure 3- 15. Roof drift ratio time history of 21-story HED diagrid building under LA09 and LA10

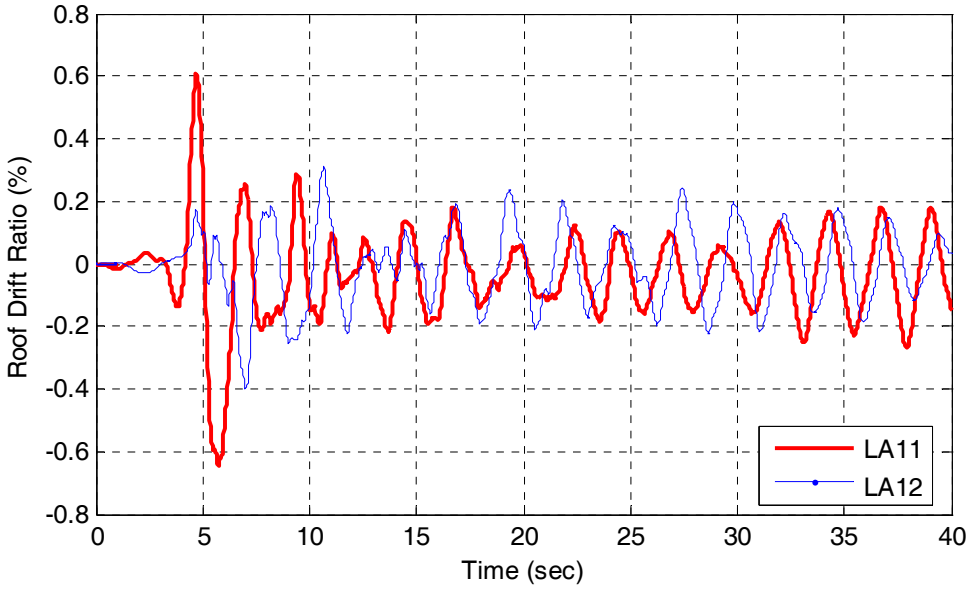

Figure 3- 16. Roof drift ratio time history of 21-story HED diagrid building under LA11 and LA12

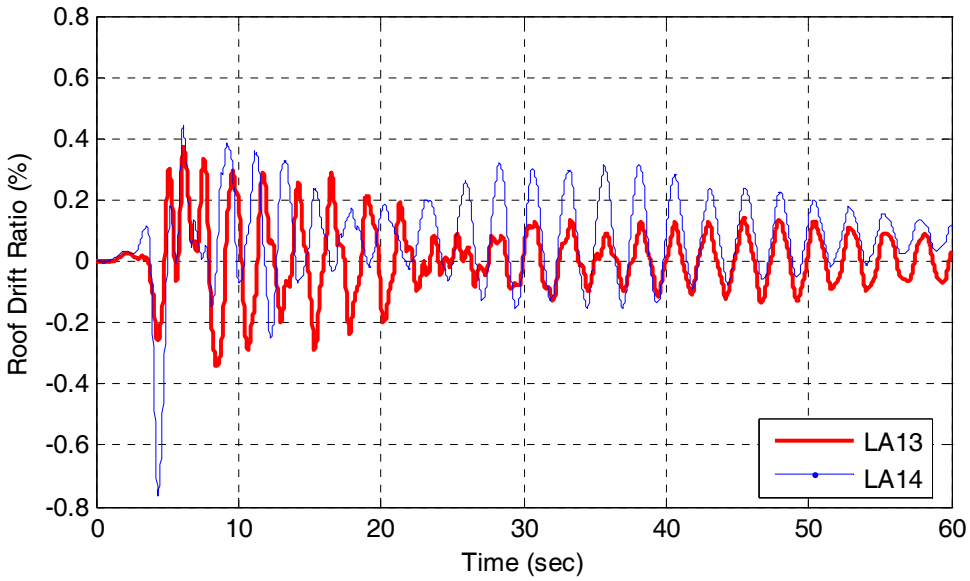

Figure 3- 17. Roof drift ratio time history of 21-story HED diagrid building under LA13 and LA14

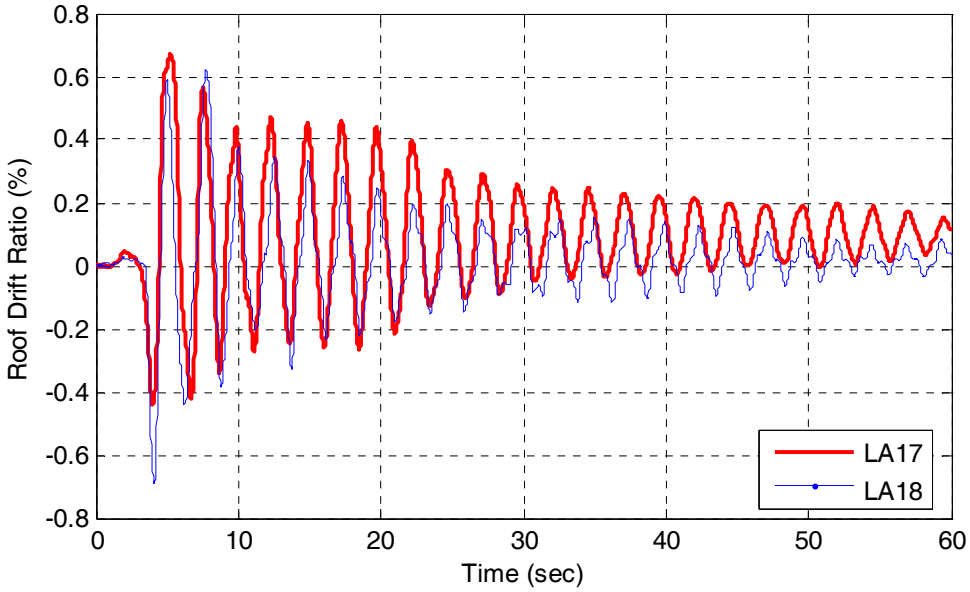

Figure 3- 18. Roof drift ratio time history of 21-story HED diagrid building under LA17 and LA18

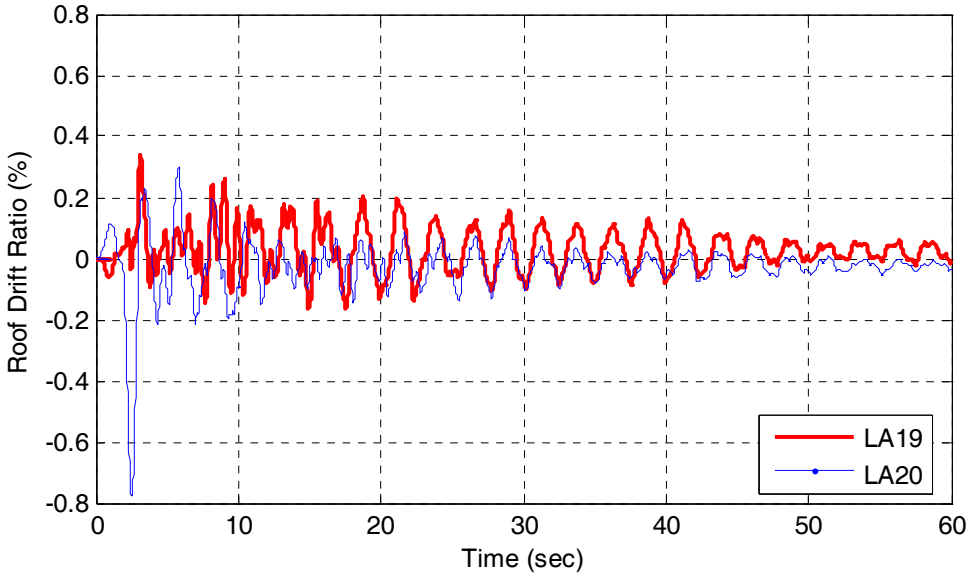

Figure 3- 19. Roof drift ratio time history of 21-story HED diagrid building under LA19 and LA20

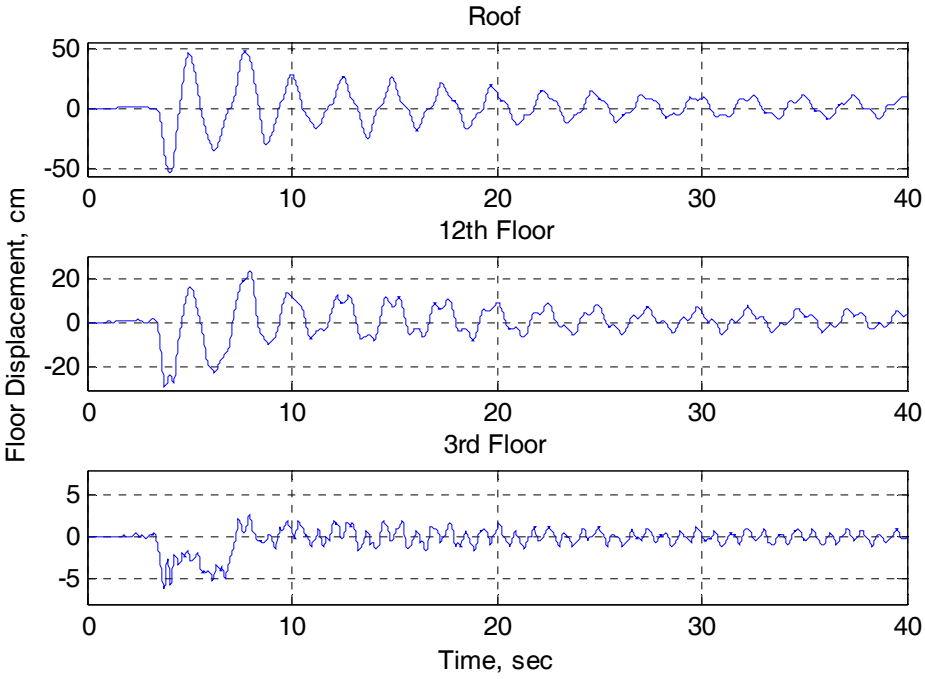

Figure 3- 20. Displacement time history of the selected floors of the 21-story HED diagrid building subjected to LA18 earthquake record

Figure 3- 21 shows the maximum roof drift ratio of the building under each earthquake record. The ensemble average value of the peak roof drift ratio is 0.58% and the maximum roof drift ratio of 0.77% occurred under LA20. The lateral deflection of the HED diagrid building is generally contributed by two main components: (i) axial deformation of the diagonals and beams (ii) deformation of the link elements. Because the diagonals and also beams are designed to remain elastic, therefore their deflection contribution are below their elastic elongation even after the shear yielding of the link. Consequently, the HED diagrid frame has a comparable lateral stiffness to conventional diagrid system. It is seen from Figure 3- 21 that relatively low peak roof drift ratio values were obtained for the HED diagrid frame under all time history analysis records.

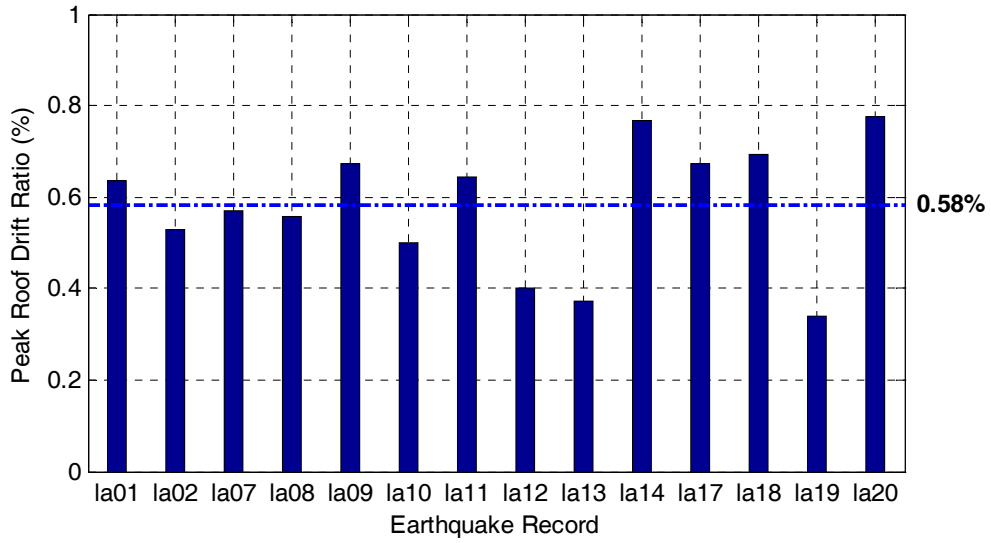

Figure 3- 21. Maximum roof drift ratio of the 21-story HED diagrid building under 14 earthquake records

Figure 3- 22 shows the residual roof drift ratio of the building under each earthquake records. The ensemble average value of the residual drift ratio is 0.04%. The residual drift ratios of up to 0.5% are considered feasible for post-earthquake repair and even the maximum residual drift ratio that occurred under the LA01 ground motion with the value of 0.11% is well below this limit.

The small residual deformation signifies a re-centering ability of the proposed HED diagrid building which is highly desirable after strong earthquake events for the benefit of preserving the building operation. This can be explained by the fact that no inelastic action occurs at the diagonals and beams of the HED diagrid building during the earthquakes and only shear links undergo plastic deformations, therefore after the earthquake the main structural elements almost regain the original shape of the building due to the angular configuration of the primary structural members in the lateral force resisting system.

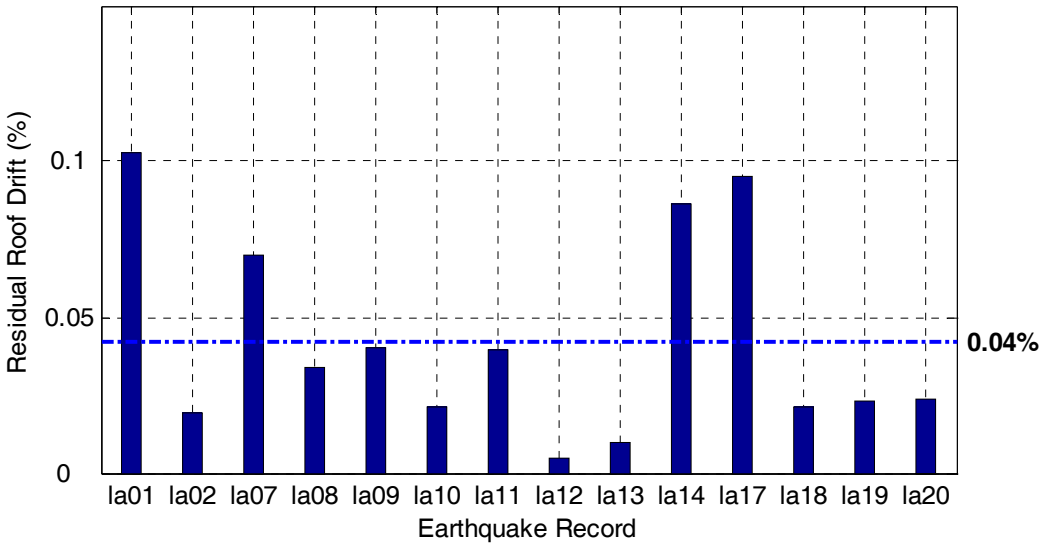

Figure 3- 22. Residual roof drift ratio of the 21-story HED diagrid building under 14 earthquake records

Figure 3- 23 shows the peak floor displacement responses of the HED diagrid building under each ground motion. It is seen from this figure that the maximum roof displacement of 59.3 cm occurred under LA20, corresponds to a roof drift ratio of only 0.77%.

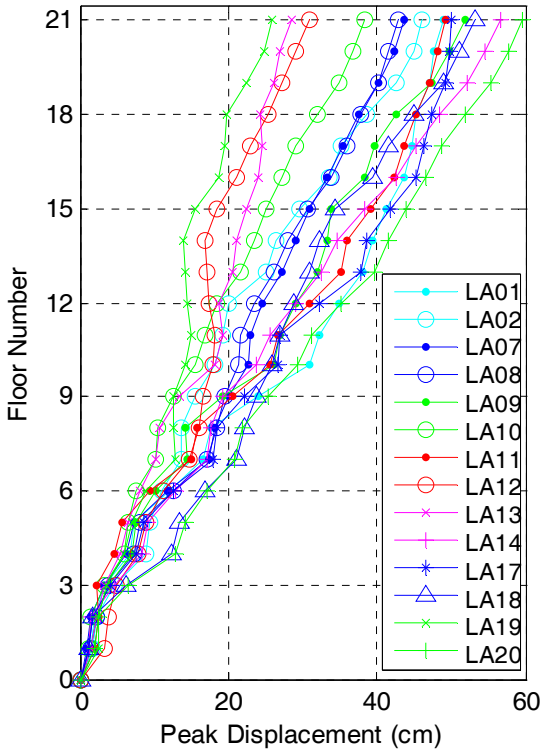

Figure 3- 23. Distribution of the peak displacement of the 21-story HED diagrid building under 14 earthquake records

3.8.5. Local Deformation Demands

The inter-story drift ratio is an important parameter for structural performance measurement since it relates to the damage in both structural and non-structural elements. The inter-story drift demands and residual inter-story drift ratios of the 21-story HED diagrid building are presented in this section.

Figure 3- 24 shows the peak inter-story drift ratio values of the 21-story HED diagrid building under 14 ground motions. The values of the inter-story drift ratio are higher at the end of each module where the shear links are located. The distribution of ensemble average inter-story drift ratios is shown in Figure 3- 24 with dark circles connected with a line with the maximum ensemble average inter-story drift ratio of 1.4% at the 16^{th} story. The maximum inter-story drift ratio happened under LA17 at the 16^{th} story with a value of 2%. Based on Section 16.2.4.3 of ASCE 7-10, the inter-story drift ratio value should be lower than 2.5% if the nonlinear time-history analysis is performed. The large triangles in Figure 3- 24 show the of the peak inter-story drift ratios of the HED diagrid building under LA18 earthquake ground motion.

Figure 3- 25 shows the values of residual inter-story drift ratio under 14 earthquake records. The dark circles connected with a line show the ensemble average inter-story drift ratios with the maximum value of 0.2% at 16^{th} story. The residual inter-story drift ratios are below 0.5% for all time history analyses except LA01 and LA14 with the maximum residual inter-story drift ratio of 0.6% occurred at 6^{th} story.

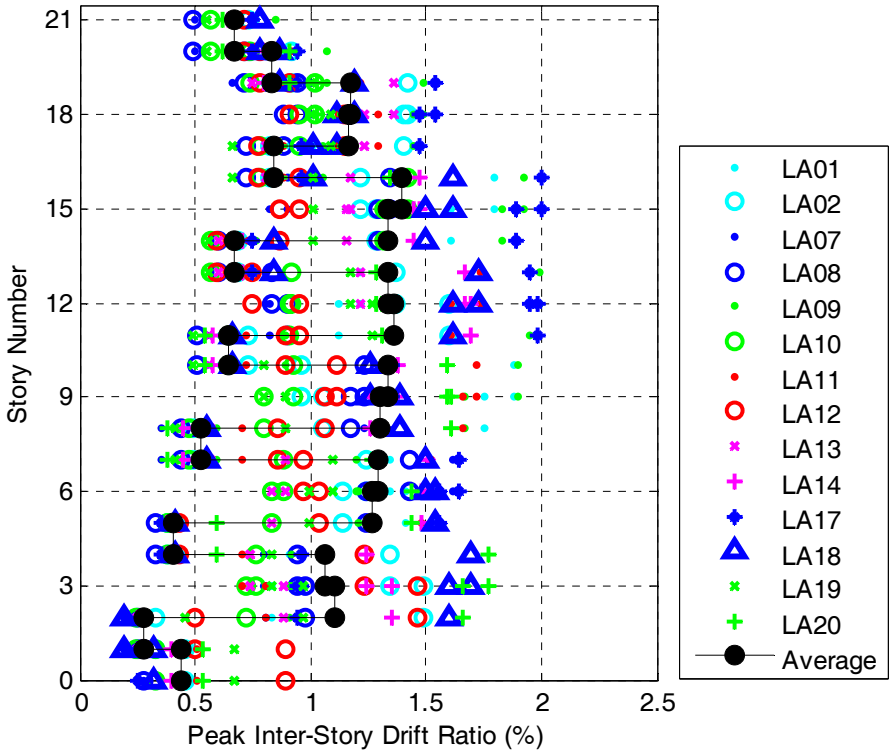

Figure 3- 24. Distribution of peak inter-story drift ratio under 14 earthquake records

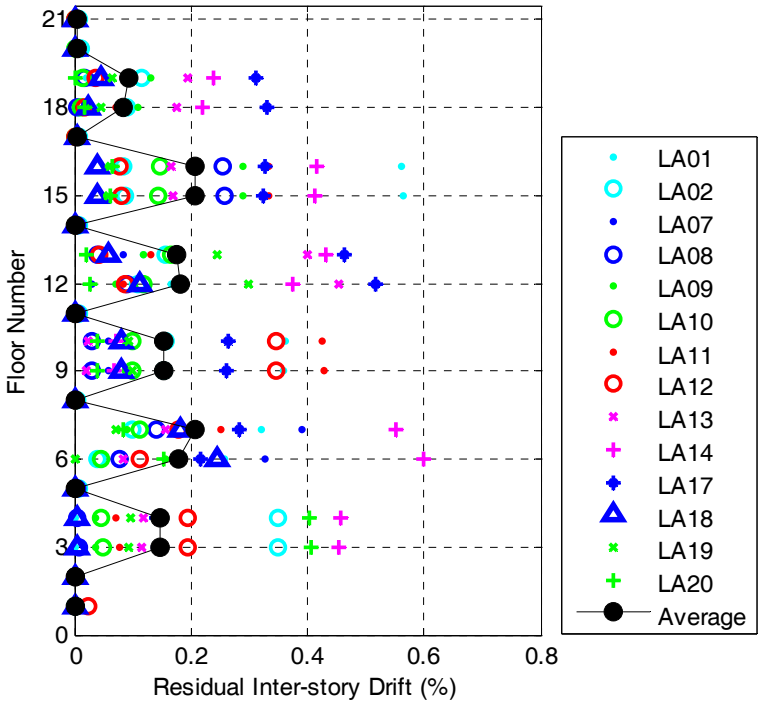

Figure 3- 25. Residual inter-story drift ratio under 14 earthquake records

3.8.6. Link Rotation Demands

Length and capacity of the links are controlling factors to maintain displacement performance goals and the stiffness and deformation of the building can be tuned by appropriate link design. Figure 3- 26 shows the maximum rotation demands of the links at each module under different ground motions. The link rotation angle is defined as the vertical displacement between two ends of the link normalized by the link length. The large dark triangles in Figure 3- 26 shows the peak links demand under LA18 ground motion. The ensemble average of peak link rotations under 14 earthquake records are shown with connected dark circles.

The maximum ensemble average of peak links rotation is 0.0225 radians at links of 9^{th} floor. The maximum rotation of 0.037 radians occurred at the 1^{st} module under the LA20 ground motion.

Figure 3- 27 shows the hysteresis loops of the side and middle shear links (see Figure 3- 1) at the 3^{rd} floor of the HED diagrid building under the LA20 ground motion, which have the largest link rotation demand among all other links under 14 earthquake records. The fat hysteresis loops of the shear links indicate the large amount of energy dissipated by shear links that are distributed along the height of the building.

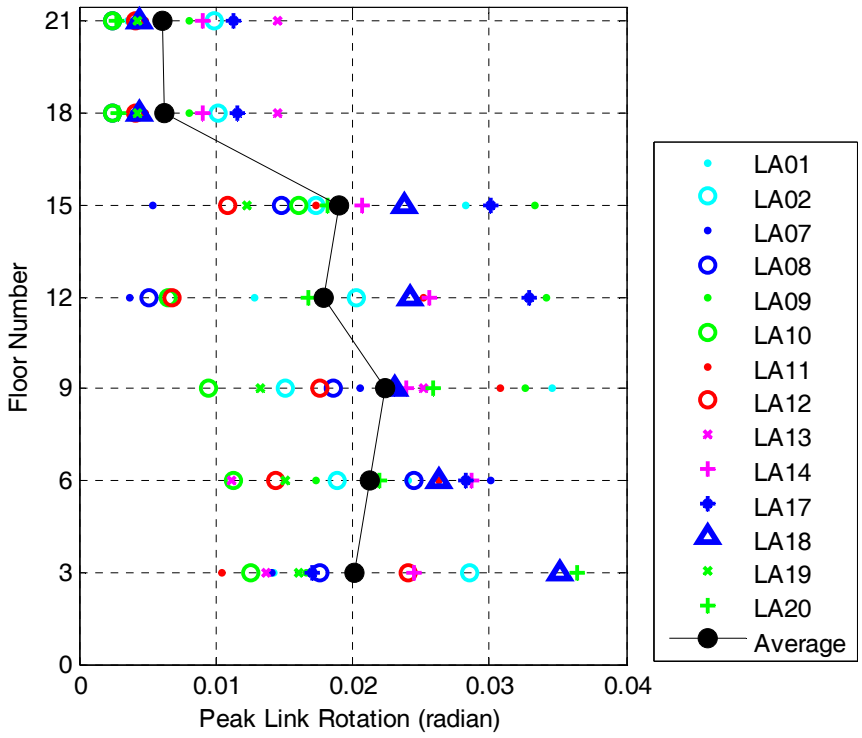

Figure 3- 26. Distribution of peak rotation demand of shear links under 14 earthquake records

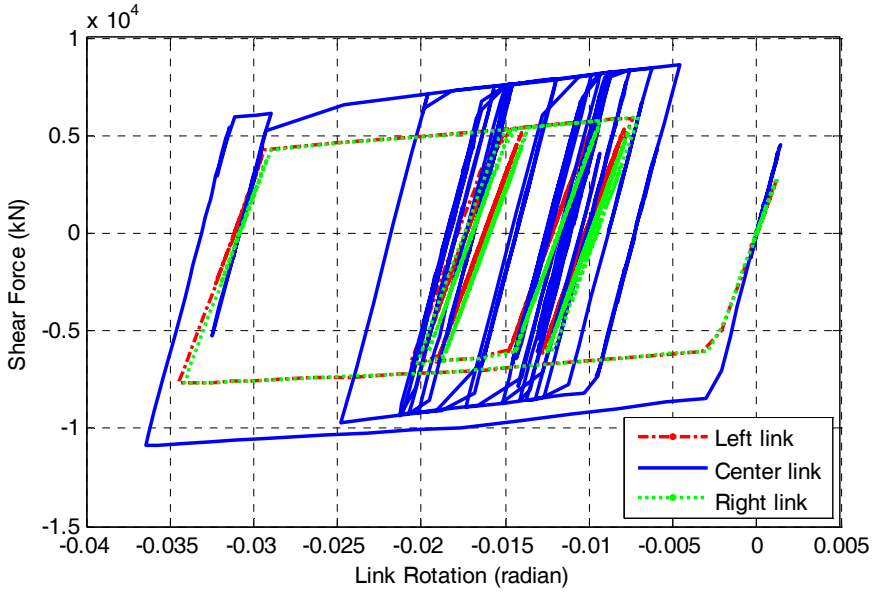

Figure 3- 27. Hysteresis loops of the shear links at the 3rd floor of the 21-story HED diagrid building under LA20

3.8.7. Base Shear Demands

The maximum base shear ratio sustained by the HED diagrid frame under each earthquake record is shown in Figure 3- 28. The average maximum base shear ratio of the building is around 0.26. The maximum and minimum base shear ratio of 0.42 and 0.19 occurred under LA12 and LA07, respectively. For high-rise building structures with long fundamental period, higher modes may dominate the response of the structure. The pushover analysis is solely based on fundamental mode and hence may not be precise in predicting the behavior of the building. The second and third periods of the HED diagrid building, are 0.8 and 0.46 sec, respectively, which fall within the prevalent frequency range of most earthquake ground motions. Therefore, the prominent effect of higher modes (particularly the 2nd mode) results in greater base shear for the nonlinear time history analysis compared to nonlinear static analysis.

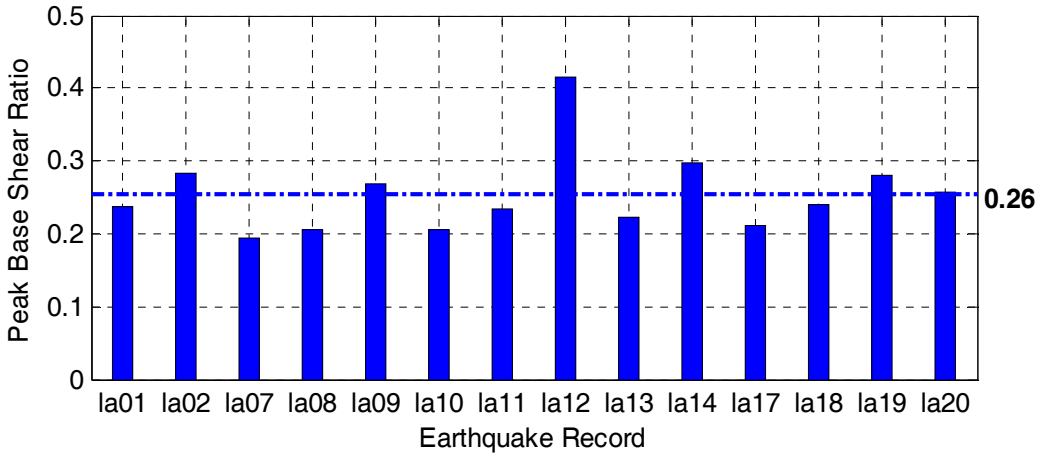

Figure 3- 28. Maximum base shear of the 21-story HED diagrid frame under 14 earthquake records

3.8.8. Floor Acceleration

Figure 3- 29 shows the acceleration time history of the 21-story HED diagrid frame at the roof, 12th and 3rd floors under the LA18 ground motion. The peak floor accelerations under all 14 ground motions along the building height are shown in Figure 3- 30. The floor accelerations under LA18 are shown with large connected dark triangles.

In the study performed by Thaghavi and Miranda (2006), it was shown that peak floor acceleration depends on the level of ground motion intensity and higher mode shapes of the structure especially in taller buildings. That study also showed that upper floors generally have smaller coefficient of variation compared to lower floors. As seen in Figure 3- 30, the lower floors acceleration varies significantly between about 0.5g and 3g for different intensities of ground motions while the variations are smaller for the higher level floors acceleration having values between about 0.5 g to 1.9 g.

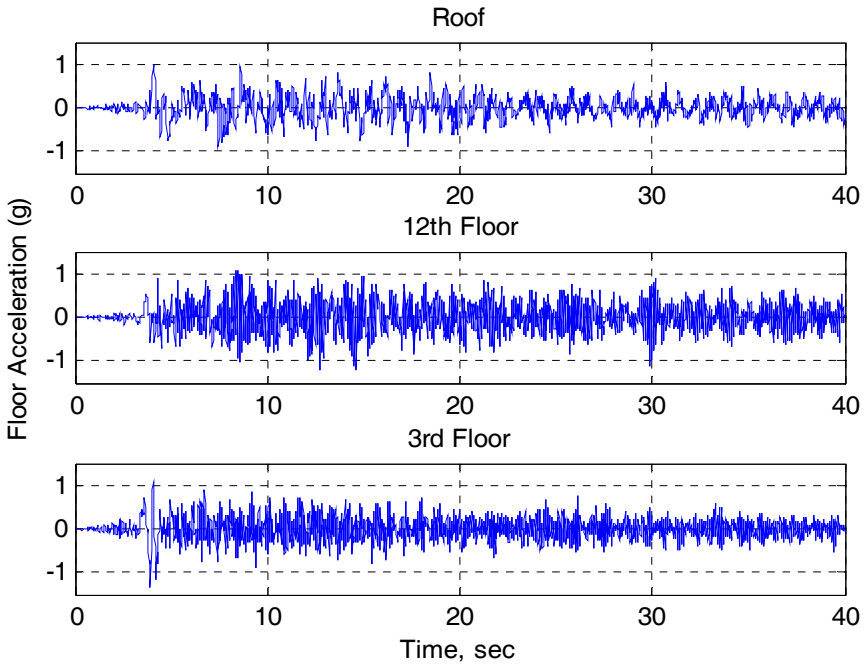

Figure 3- 29. Acceleration time history of the selected floors of the 21-story HED diagrid building under LA18

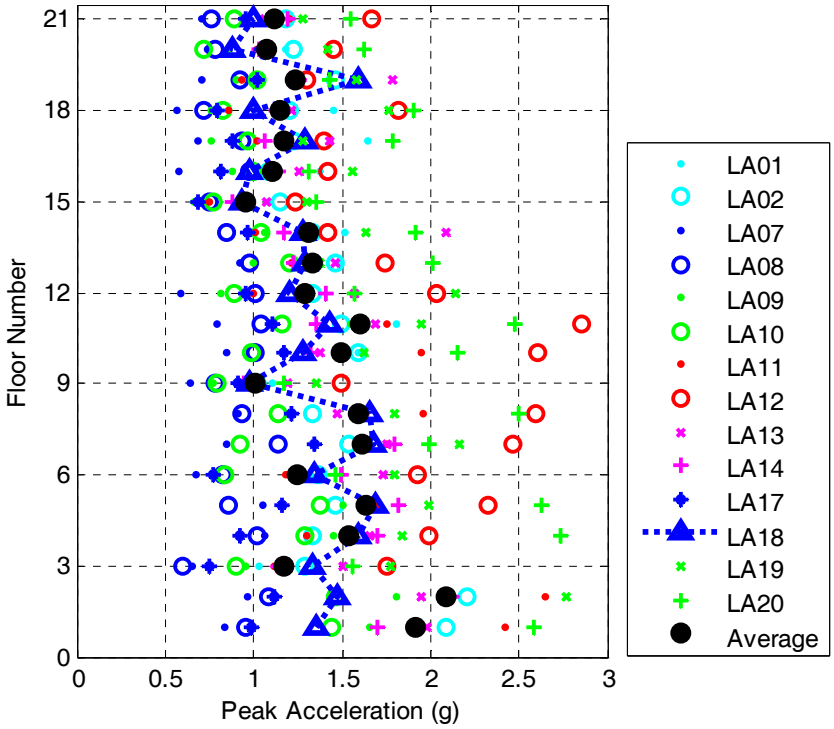

Figure 3- 30. Distribution of peak floor acceleration of the 21-story HED diagrid building under 14 earthquake records

3.9. Summary and Conclusions

This chapter presented the highly energy-dissipative ductile (HED) diagrid framing structure as a new type of seismic resistant system. The nonlinear response of a prototype HED diagrid frame was investigated using a finite element model developed in OpenSees.

HED diagrid framing system has high elastic stiffness due to its angular configuration and the axial action of the principal diagonal elements. The HED diagrid structural system also features high ductility and energy dissipation capability attributed to stable plastic deformation mechanism associated with its shear links connecting the diagonal nodes. This is observed in a case study involving both nonlinear static and time history analysis of a 21-story steel HED diagrid building frame.

The nonlinear time history analysis of a 21-story HED diagrid building is performed with an ensemble of 14 earthquake records scaled to the design basis earthquake (i.e., with 10% probability of exceedance in 50 years) of the Los Angles, California region. The findings from nonlinear time history analysis verify that satisfactory seismic performance can be achieved by HED diagrid framing structures subjected to design basis earthquakes. The HED diagrid structure retains the diagonal and beams elastic and effectively dissipates energy through web shear yielding mechanism associated with the links. In particular, one appealing feature of the HED diagrid building is the small residual displacement after strong earthquakes. The low response values of 0.58% and 0.04% were observed for the ensemble averages of maximum drift ratio and residual drift ratio at roof level, respectively. The ensemble

average of maximum inter-story drift ratio observed along the height of the HED diagrid building was 1.4%. The small roof residual drifts associated with the HED diagrid building is believed to be related to the "pull-back" effect from inclined diagonal elements which remain elastic during earthquakes.

Based on the analysis results presented in this chapter, it is concluded that HED diagrid framing system provides a promising seismic-force resistant structural system which is not only aesthetically elegant, but also promising for application in high seismic regions. Furthermore, the links alleviate the complexity in designing and constructing the connection which is one of the challenges in diagrid system design and construction. Under severe earthquake loading, the damage can be confined to the links which are easy to replace and hence ease of reparability and its relatively low cost is another advantage of the system.

CHAPTER 4 : PARAMETRIC STUDY OF HED DIAGRID FRAMING SYSTEM

4.1. Introduction

A new type of seismic resistant diagrid structural system termed "HED (highly-energy-dissipative ductile) diagrid" frame was proposed in Chapter 3. In the HED diagrid framing system, energy dissipation is realized in dedicated fuse elements and consequently seismic performance can be improved. As it was presented in Chapter 3, the HED diagrid framing design provides a competitive design option in high seismic regions with its high ductility and improved energy dissipation capacity provided by replaceable shear links interconnecting the diagonal members at their joints.

A parametric study was carried out on the HED diagrid frame to better understand the effect of design parameters on the performance of such systems. The considered parameters are the length of shear links and slope of diagonals.

In the following sections of this chapter, four case study HED diagrid buildings considered for the parametric study are presented and the effects of design parameters on structural seismic behavior of HED diagrid structure are demonstrated through nonlinear static and nonlinear time history analysis of the case study buildings under the same set of 14 strong ground motions that were used in Chapter 3. The analysis results of all cases are presented and discussed.

4.2. Case Studies

The 3x3 bay, 21-story HED diagrid building analyzed in Chapter 3 is considered as the original prototype building for comparison basis and four case studies are defined with variable design parameters. The considered parameters are the length of shear links and the inclination angle of diagonals. Member sizes in this parametric study are kept the same as the prototype building studied in Chapter 3 for consistency in comparative study and one parameter was varied at a time.

The length of shear links was 1.0 m for the original prototype building. As the length of shear link increases, the flexural behavior becomes more dominant in the link while decreasing its length makes shear deformation the dominant mode. To investigate the effect of shear link's length on seismic performance of the building, a ±20% change in length was considered. The links with 20% increase in length are still shear behavior dominant since their length is still below the limiting value of Eq. (3.5). Therefore, two case studies titled SL-1 and SL-2, were defined with the shear links of 0.81 m (32 inch) and 1.21 m (48 inch) length, respectively.

The change in diagonals' inclination angle will change the aspect ratio of the diagrid building since it changes the bay width of the building while the story height and consequently the total height of the building is kept constant. For fair comparison purpose, no significant change in global shear and flexural behavior of the building was desired in this parametric study, therefore the changes were kept within about ±5% of the original angle of diagonals which was 72°. Two HED diagrid buildings with diagonals inclination angle of 68° and 76° were created and titled DS-1 and DS-2, respectively.

Table 4- 1 shows a summary of the considered case studies with the values of length of shear links and inclination angle of diagonals.

Table 4- 1. HED diagrid building case studies

Case	Diagonal angle (deg)	Length of shear links, *e* (m)
SL-1	72	0.81
SL-2	72	1.21
DS-1	68	1.0
DS-2	76	1.0

4.3. Numerical Modeling

The two-dimensional models of the four case study buildings, similar to the model of the original prototype building in Chapter 3, were developed in OpenSees. The same element that was previously created for the shear link was used in the finite element models of these case studies. Also, nonlinear beam-column elements and truss elements were used for beams and diagonals, respectively. The material properties, constraints and lean-on column configuration were also similar to the original prototype building model.

The seismic weight of all case study buildings were kept the same as original prototype building so that the change in analysis results of different cases would be solely due to changed design parameters (i.e. length of shear links and inclination angle of diagonals). Therefore, the floor and roof seismic weights of the all case studies were 5780 kN (1300 kips) and 6450 kN (1450 kips), respectively.

4.4. Eigen Value Analysis

The Eigen value analysis was performed for all the case studies to compare the effect of changed parameters on natural frequencies of the building. Table 4- 2 shows a comparison of first three vibration periods of original prototype building and the case studies.

Chang in the length of shear links has a small effect on Eigen value analysis results of the prototype building. Shortening the shear links increases the stiffness of the structure while longer links reduces the stiffness of the building. The first three vibration periods of case SL-1 with shorter shear links (e=0.81 m) were 2.45, 0.78 and 0.44 seconds, respectively. The first three vibration periods of case SL-2 with longer shear links (e=1.21 m) were 2.53, 0.84 and 0.49 seconds, respectively.

The effect of changing slope of diagonals is more significant on Eigen value analysis results since the aspect ratio of the building changes rapidly with change of geometry. The aspect ratio of the buildings of cases DS-1 and DS-2 are 2.42 and 3.57, respectively while the aspect ratio of the original prototype building was 2.9. The first three vibration periods of case DS-1 with lower diagonals angle were decreased to 2.15, 0.70 and 0.43 seconds, respectively. The first three vibration periods of case DS-2 were increased to 2.79, 0.97 and 0.55 seconds, respectively.

Table 4- 2. First three natural periods of the original prototype HED diagrid building and parametric study cases

Case	Vibration periods (sec)		
	T_1	T_2	T_3
Original prototype building	2.48	0.8	0.46
SL-1	2.45	0.78	0.44
SL-2	2.53	0.84	0.49
DS-1	2.15	0.70	0.43
DS-2	2.99	0.97	0.55

4.5. Nonlinear Static Analysis

Nonlinear static analysis of all 21-story HED diagrid building case studies was performed to identify the effect of changed parameters on force-deformation response of the HED diagrid frame. The aforementioned inverted triangular lateral load profile was used as lateral load pattern for all cases. The lateral loads were applied as concentrated forces applied to the left most nodes at each floor level. The loads were increased monotonically until the horizontal displacement at the roof reached a value corresponding to 3% roof drift ratio.

Figure 4- 1 shows the pushover curves of the SL-1 and SL-2 cases considered in the parametric study along with the pushover curve of the original prototype building. The sequence of plastic deformation development is indicated with the markers corresponding to Points Y1 to Y4 similar to Figure 3- 9 in Chapter 3. The elastic stiffness of all three cases are about the same since their fundamental periods were fairly close. The main difference between the pushover response of these cases are at the roof drift ratio level that shear link's deformation exceeds the limits of the first and second post-yield branch of the link's force-deformation curve (δ_2 and δ_3 in Figure 3- 6). Also the roof drift ratio level at which the rotation of some links exceed 0.08 radians and the diagonals start to yield (i.e. Point Y4) is different for each case. It is observed that the link's deformation demand increases with decreasing length of the shear links. As it can be seen in Figure 4- 1, the third and fourth post-yield branches of the pushover curve were started at a lower roof drift ratio value for case SL-1 in comparison with the original prototype building. Similarly but conversely, the third and fourth post yield branches of the pushover curve were started at the

higher roof drift ratio for case SL-2 compared to the original prototype building. The roof drift ratio corresponding to Point Y2 for the case SL-1, original prototype building and case SL-2 were 0.85%, 0.93% and 1.05%, respectively. Initiation of point Y3 for the case SL-1, original prototype building and case SL-2 occurred at roof drift ratio of 1.4%, 1.58% and 1.75%, respectively. The rotation of some shear links exceed the limit of 0.08 radians at roof drift ratio of 1.82%, 2.1% and 2.35% for case SL-1, original prototype building and case SL-2, respectively. At this stage first yielding of diagonals was also observed.

The comparison between pushover analysis results of cases DS-1 and DS-2 and original prototype building is shown in Figure 4- 2. As it was expected from the Eigen value analysis the elastic stiffness of case DS-1 is higher than the original prototype building, while the elastic stiffness is decreased with increased diagonal angles for case DS-2. The linear behavior was observed for case DS-1, original prototype building and case DS-2 up to the roof drift ratio of 0.58%, 0.63% and 0.7%, respectively (Point Y1). The sequence of plastic deformation development is similar in three cases, however the link deformation demands are higher for case DS-1 and lower for case DS-2 at a particular level of pushover analysis. The roof drift ratio corresponding to Point Y2 for the case SL-1, original prototype building and case SL-2 were about 0.84%, 0.93% and 1.12%, respectively. Initiation of Point Y3 for the case SL-1, original prototype building and case SL-2 occurred at roof drift ratio of about 1.42%, 1.58% and 1.9%, respectively. Diagonals of case DS-1 experience higher ductility demand compared to original prototype building at a same stage of pushover analysis. The stage of pushover analysis at which the first yielding of

diagonals was observed, were corresponding to the roof drift ratio of 1.3% and 2.1% for case DS-1 and original prototype building. Pushover analysis of case DS-1 stopped at a level corresponding to roof drift ratio of 2.6%, when more than ten diagonals yielded. No yielding of diagonals occurred during the entire pushover analysis of case DS-2.

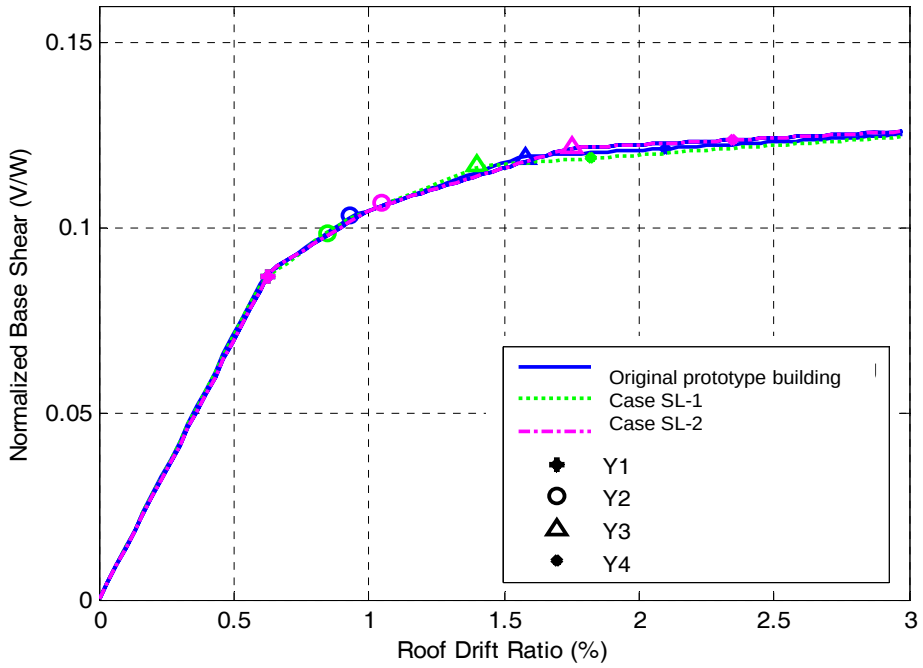

Figure 4- 1. Push-over curves of original prototype building and cases SL-1 and SL-2

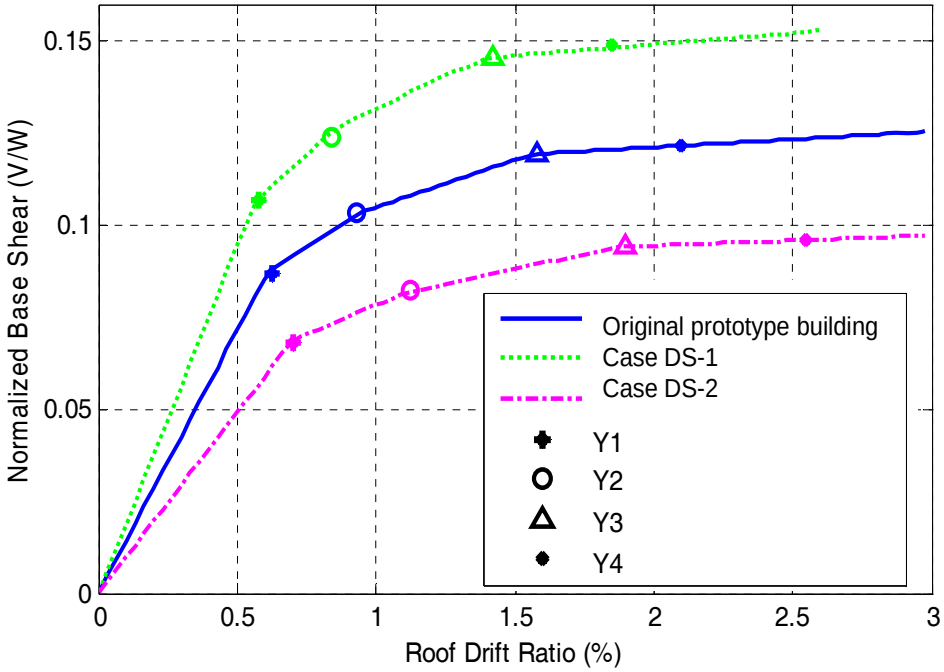

Figure 4- 2. Push-over curves of original prototype building and cases DS-1 and DS-2

4.6. Nonlinear Time History Analysis

The nonlinear time history analysis of all cases considered in this parametric study was performed under the same 14 strong earthquake records with a probability of exceedance of 10% in 50 years for Los Angles, California area, that were used in Chapter 3 (see Table 3- 2). The time interval used for all time history analyses was 0.02 seconds. The Newark average-acceleration (γ=1/2, β=1/4) time-step integration method was used to solve the dynamic equations. Rayleigh damping with 2% damping ratio for the first and third modal frequencies of the building were assigned for the nonlinear time history analysis of all cases in the OpenSees model.

The results of structural members ductility demands, roof displacements and drifts, residual roof drifts, inter-story drifts and residual inter-story drifts, links rotation demand, peak base shear and floor acceleration response of all case studies are presented in this section and compared with the results of the original prototype building.

In the results presented in following sections, the "peak" result refers to the highest absolute value of the specified parameter (e.g. ductility demand, inter-story drift ratio, etc.) recorded during the time history analysis. The "ensemble average" refers to the mathematical average value of the results obtained from 14 time history analyses. This value is used is shown in some figures with the dark circles that are connected with a line.

4.6.1. Structural Members Ductility Demands

The ductility demands of main structural elements of HED diagrid buildings under parametric study are important index measuring the seismic performance of the HED diagrid framing system since one of the main goals in design of an HED diagrid structure, is to keep the main structural elements elastic. In addition, yielding of diagonals may result in large story displacements. The ductility demands of diagonals defined by Eq. (3-17) were calculated for all cases from the time history analysis results under 14 earthquake records.

The maximum stresses on all beams were checked and it was ensured that they all remained elastic during all the 14 time history analyses for all case studies.

The force-deformation response of all diagonals were recorded during the time history analysis and peak axial displacement imposed on diagonals of each story was identified by a post-processing code developed in MATLAB (Mathworks Inc.). The peak ductility demand of diagonals of each story were calculated under individual ground motions and the average of ensemble of results under 14 ground motions were calculated. For the original prototype building the maximum ensemble average of peak ductility demand was 0.88 occurred at 13^{th} story and the highest ductility demand of 0.98 was recorded under LA12 at 1^{st} story diagonal as shown in Figure 3-12.

Figure 4- 3 (a) and (b) show the peak ductility demands of diagonals of each story under each earthquake record for cases SL-1 and SL-2. The ductility demands of diagonals at first story decreased for case SL-1 and increased slightly for case SL-2 but remained almost the same for all other stories in both cases with the maximum

ensemble average of value of about 0.88 at the 13th story similar to original prototype building. All the diagonals remained elastic under all earthquake records for both cases except for the diagonal at the 1st story of case SL-2 which has a ductility demand of 1.02, just slightly larger than one.

The diagonals' peak ductility demands of cases DS-1 and DS-1 are shown in Figure 4- 4 (a) and (b). The ductility demand of diagonals of almost all stories were increased significantly for case DS-1. The increase in diagonals ductility demand was less significant for case DS-2. The maximum ensemble average of peak ductility demand observed at 13th story was increased by 25% for case DS-1 to a value of about 1.1 and remained almost the same for case DS-2 with a values of 0.88. The largest ductility demand in case DS-1 was about 1.45 at 13th story under LA12. For case DS-2, the largest ductility demand of 1.15 occurred under LA20 in diagonals of first story.

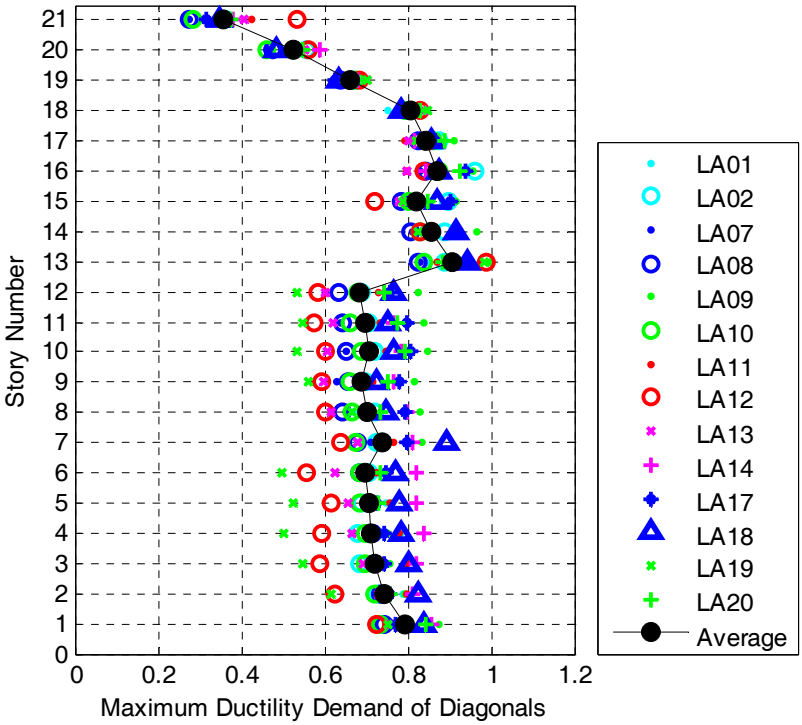

(a)

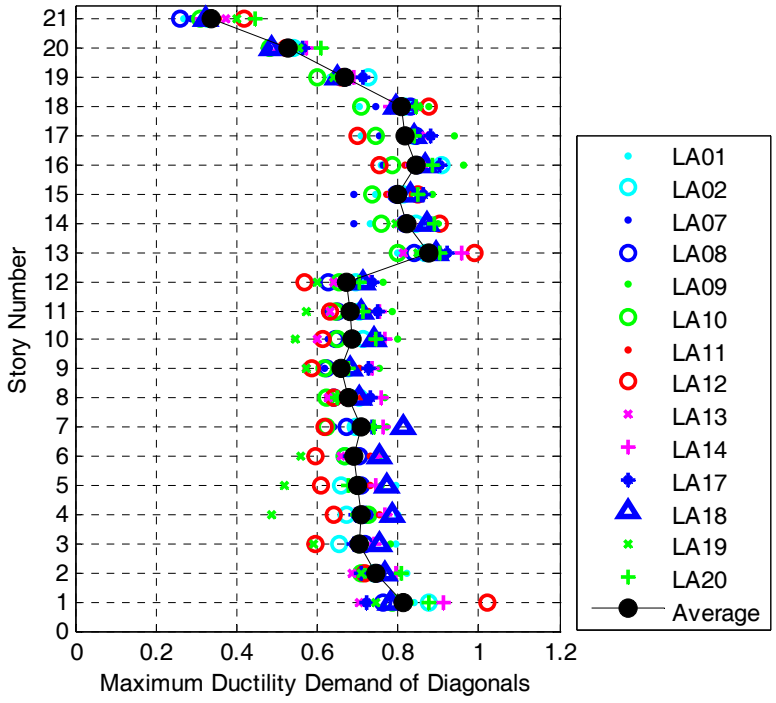

(b)

Figure 4- 3. Maximum ductility demand of diagonals of each story under 14 earthquake records: (a) Case SL-1; (b) Case SL-2

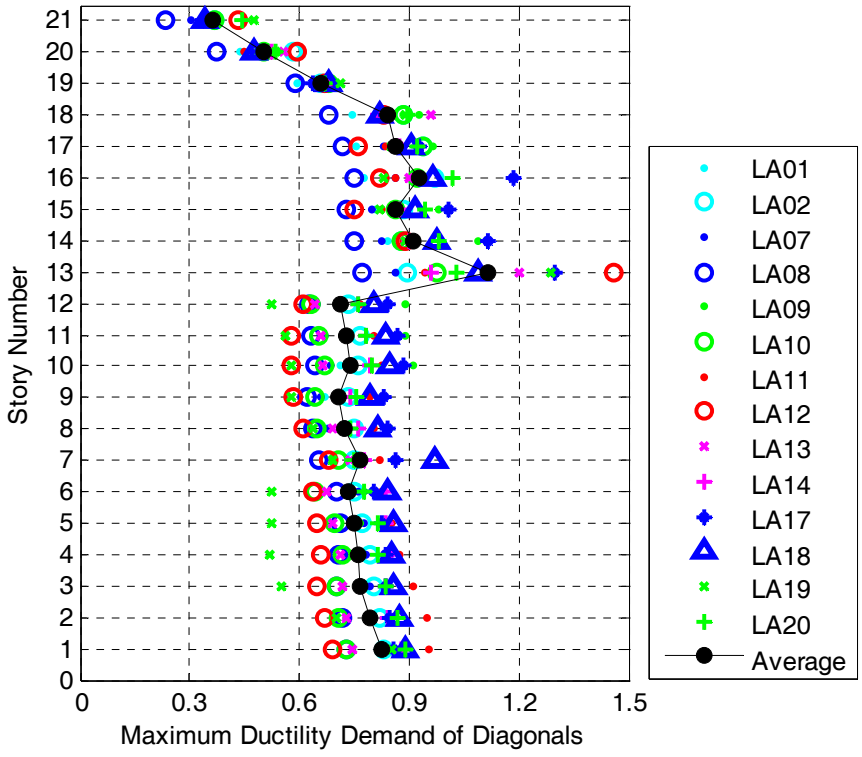

(a)

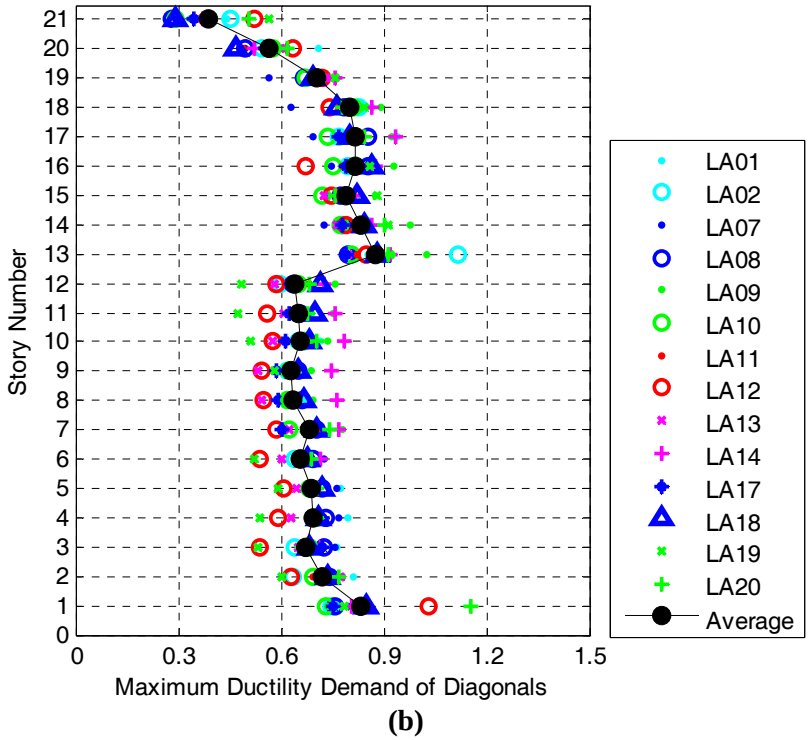

(b)

Figure 4- 4. Maximum ductility demand of diagonals of each story under 14 earthquake records: (a) Case DS-1; (b) Case DS-2

4.6.2. Global Deformation Demands

Figure 4- 5 (a) and (b) show the roof drift ratios and roof residual drift ratios of the case studies SL-1 and SL-2, respectively. The roof drift ratios and roof residual drift ratios of cases DS-1 and DS-2 are shown in Figure 4- 6 (a) and (b). The ensemble average of peak roof drift ratio and residual roof drift ratio of the original prototype building were 0.58% and 0.04%, respectively. The most significant change was observed in global displacement demands of case DS-2 (i.e. the building with higher diagonals inclination angle).

For case SL-1 (i.e. the building with shorter links), the ensemble average of peak roof drift ratio remained unchanged (0.58%) while the residual roof drift ratio increased from 0.04% to 0.05% as shown in Figure 4- 5 (a). The maximum roof drift ratio and roof residual drift ratio were observed under LA20 and LA01 respectively, with almost the same values as obtained for original prototype building.

As observed from Figure 4- 5 (b), the ensemble average of peak roof drift ratio and ensemble average of roof residual drift ratio for case SL-2 were increased to 0.6% and 0.06%, respectively. The maximum roof drift ratio was observed under LA20 with and the maximum roof residual drift ratio was observed under LA14 with value similar to that of the original prototype building.

Figure 4- 6 (a) shows that the value of 0.57% was obtained for ensemble average of peak roof drift ratio of case DS-1. The ensemble average of roof residual drift ratio was increased by about 50% to the value of 0.061%. The maximum roof drift ratio and roof residual drift ratio occurred under LA17 with the values of 0.74% and 0.21%, respectively.

Figure 4- 6 (b) shows a more significant change in global deformation demands of case DS-2. The ensemble average of peak roof drift ratio was increased by 0.19% from 0.58% for original prototype building to 0.69%. The ensemble average of roof residual drift ratio was also increased by about 0.85% to a value of 0.073%. The maximum roof drift ratio and roof residual drift ratio occurred under LA09 with the value of 0.94% and LA01 with the value of 0.17%, respectively.

In summary, no improvement in roof drift ratio and especially roof residual drift ratio was observed in the parametric study cases. While the changes in the results of cases SL-1 was not dramatic, the ensemble average of residual inter-story drift ratio was increased by approximately 50% for both SL-2 and DS-1 cases. The increase in both peak roof drift ratios and residual roof drift ratios was the most significant in case DS-2.

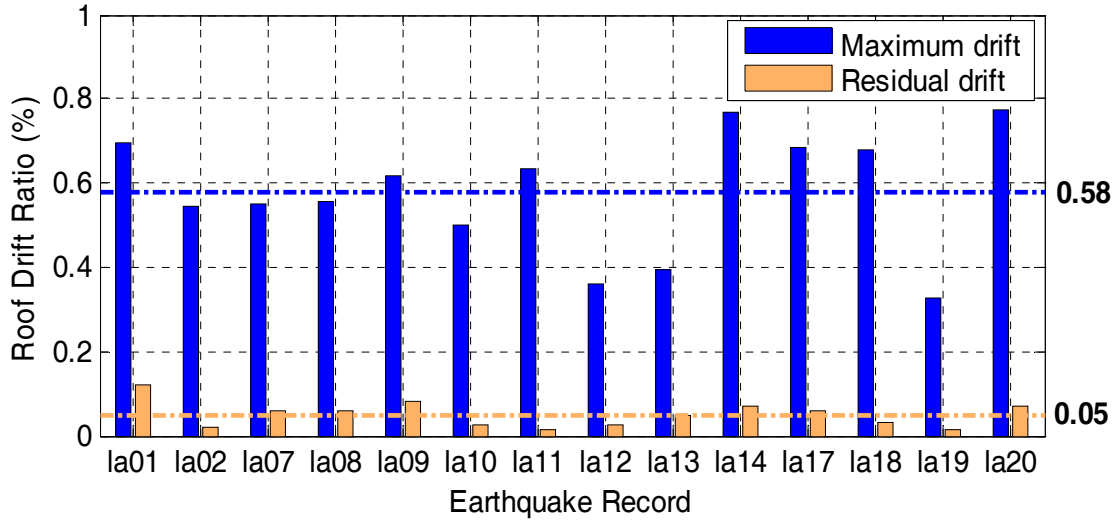

(a)

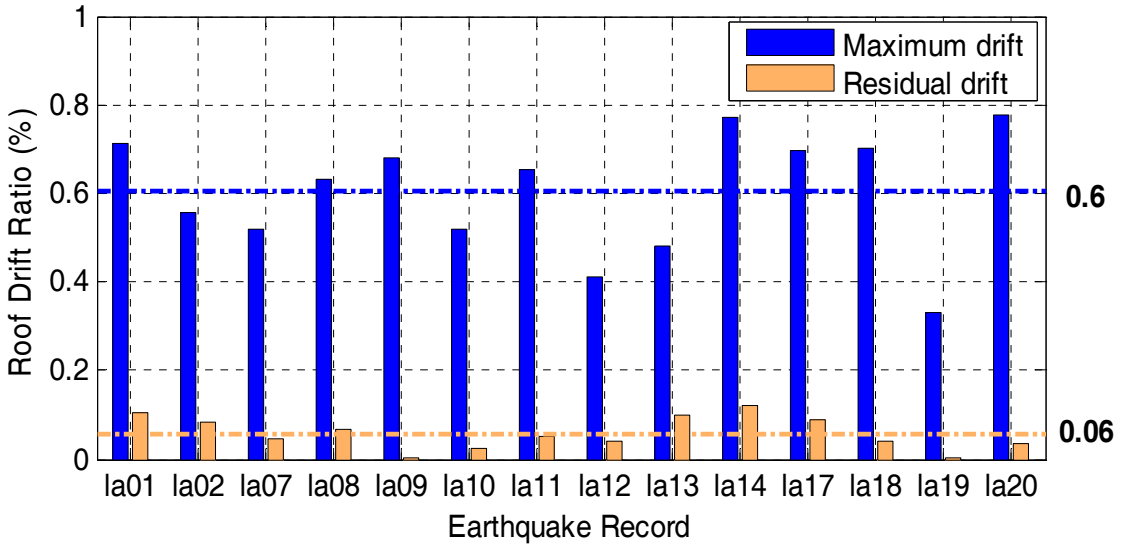

(b)

Figure 4- 5. Maximum roof drift ratio and residual roof drift ratio of the 21-story HED diagrid building under 14 earthquake records: (a) Case SL-1; (b) Case SL-2

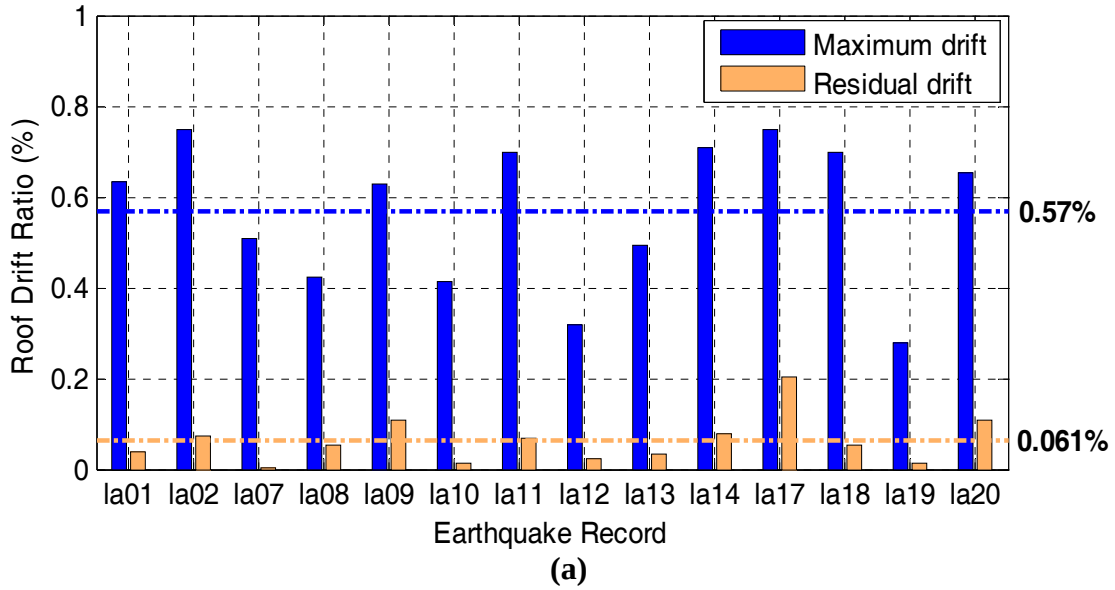

(a)

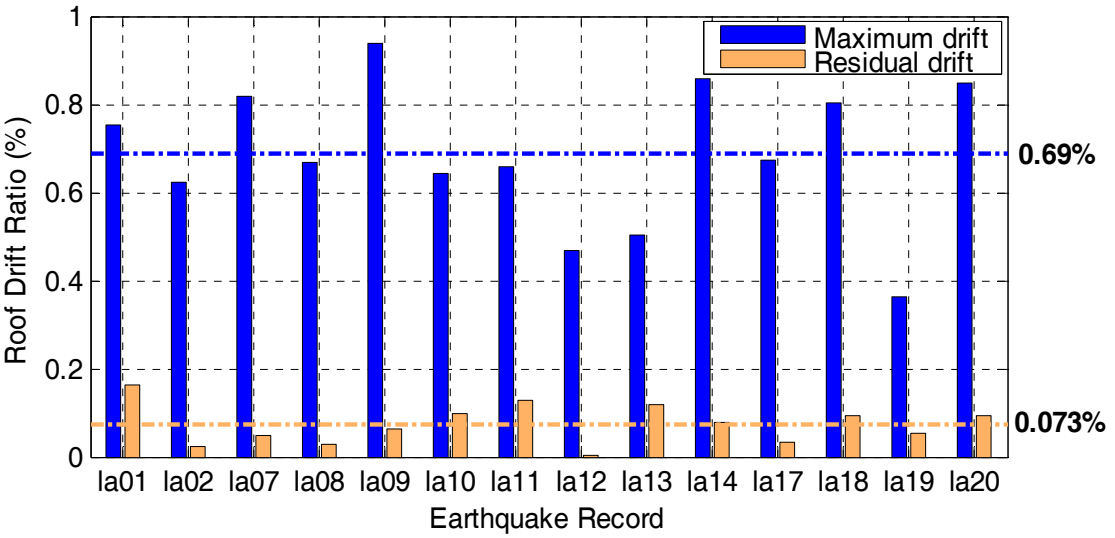

(b)

Figure 4- 6. Maximum roof drift ratio and residual roof drift ratio of the 21-story HED diagrid building under 14 earthquake records: (a) Case DS-1; (b) Case DS-2

4.6.3. Local Deformation Demands

It was shown in Figure 3- 24 that the maximum ensemble average of inter-story drift ratio of the original prototype building was about 1.4% at the 16th story. The maximum inter-story drift ratio was observed under LA17 at the 16th story with a value of 2%. The maximum ensemble average of inter-story residual drift ratio was about 0.2% for both 15th and 16th story. The inter-story drift ratios and residual inter-story drift ratios of parametric study cases are presented in this section.

The peak inter-story drift ratio and residual inter-story drift ratio for all stories of building studied in case SL-1 are shown in Figure 4- 7 (a) and (b), respectively. The maximum ensemble average of peak inter-story drift ratio for case SL-1 occurred at 13th story with the value of about 1.32% which is lower than the corresponding value for the original prototype building. The value of maximum peak inter-story drift ratio was about 1.99% similar to the original prototype building occurring under LA01 at 12th story. The residual inter-story drift ratios were smaller for some earthquake records and larger for others with all values below 0.5% except under LA11 and LA17 with maximum residual inter-story drift ratio of 0.62% occurred at 9th story. The maximum ensemble average of inter-story residual drift was increased to 0.22% which occurred at 10th story. From the abovementioned observations, it can be concluded that a 20% decrease in length of shear link decreased the inter-story drift ratios but increased the residual inter-story drift ratios.

Figure 4- 8 (a) and (b) show the inter-story drift ratios and residual inter-story drift ratios of case SL-2, respectively. The peak inter-story drift ratios were increased for case SL-2. The maximum ensemble average of peak inter-story drift ratio

occurred at 13th story with the value of about 1.46%. The maximum peak inter-story drift ratio occurred under LA01 at 10th story with a value of 2.22%. The maximum ensemble average of residual inter-story drift ratio of 0.18% occurred at 16th story, which is less than the corresponding value of 0.2% for the original prototype building. Also, the maximum residual inter-story drift ratio was 0.48% at 6th story under LA14 which is smaller than corresponding values for original prototype building. From the observations, it is concluded that even though the peak inter-story drift ratio values increased for case SL-2, but the residual inter-story displacements were decreased slightly.

The inter-story drift ratio and residual inter-story drift ratio values along the height of the building for case DS-1 are shown in Figure 4- 9 (a) and (b), respectively. The maximum ensemble average of peak inter-story drift ratio that occurred at 10th story was about 1.38% which is close to the corresponding value obtained for the original prototype building that was 1.4%. The maximum peak inter-story drift ratio was about 2.25% at 16th story that occurred under LA09. The maximum ensemble average of residual inter-story drift ratio for case DS-1 was about 0.78% occurring at 16th story which is higher than the corresponding value for the original prototype building that was 0.6% at 6th story; however, the maximum ensemble average of residual inter-story drift ratio of 0.21% at 16th story which is only 5% larger than the corresponding value of the original prototype building. In summary the slight increase in the value of peak inter-story drift ratio and residual inter-story drift ratio values were observed for case DS-1 compared to original prototype building.

Figure 4- 10 (a) and (b) show the peak inter-story drift ratios and residual inter-story drift ratio values of case DS-2, respectively. The inter-story deformation demands were increased significantly for case DS-2. The maximum ensemble average of peak inter-story drift ratio occurred at 16^{th} story shows a value of 1.66% which is about 20% higher than the corresponding value obtained from time history analysis of original prototype building. The maximum peak inter-story drift ratio reached to a value of about 2.38% at 4^{th} and 18^{th} story under LA20 and LA09, respectively. The maximum ensemble average of residual inter-story drift ratio of 0.28% at 18^{th} story and maximum residual inter-story drift of 0.73% at 16^{th} story under LA18 indicate the significant increase in residual displacements for case DS-2 compared to original prototype building. In summary, the analysis results showed 20% increase in ensemble average of peak inter-story drift ratio and 40% increase in maximum ensemble average of residual inter-story drift ratios for case DS-2.

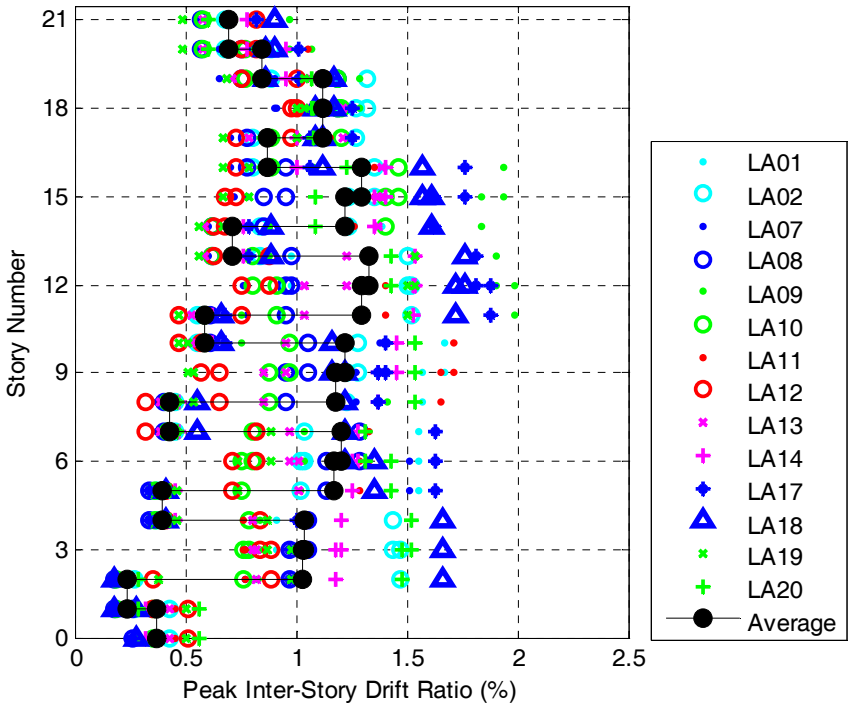

(a)

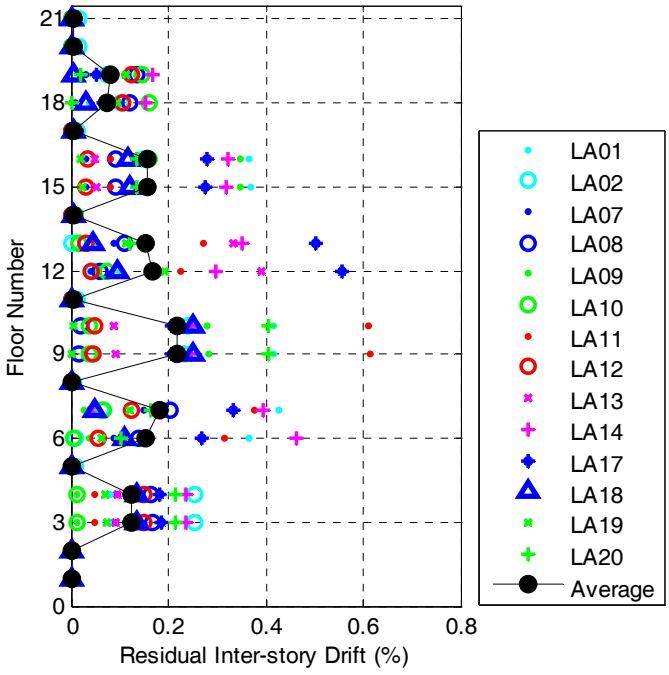

(b)

Figure 4- 7. Case SL-1: (a) Peak inter-story drift ratio; (b) Residual inter-story drift ratio

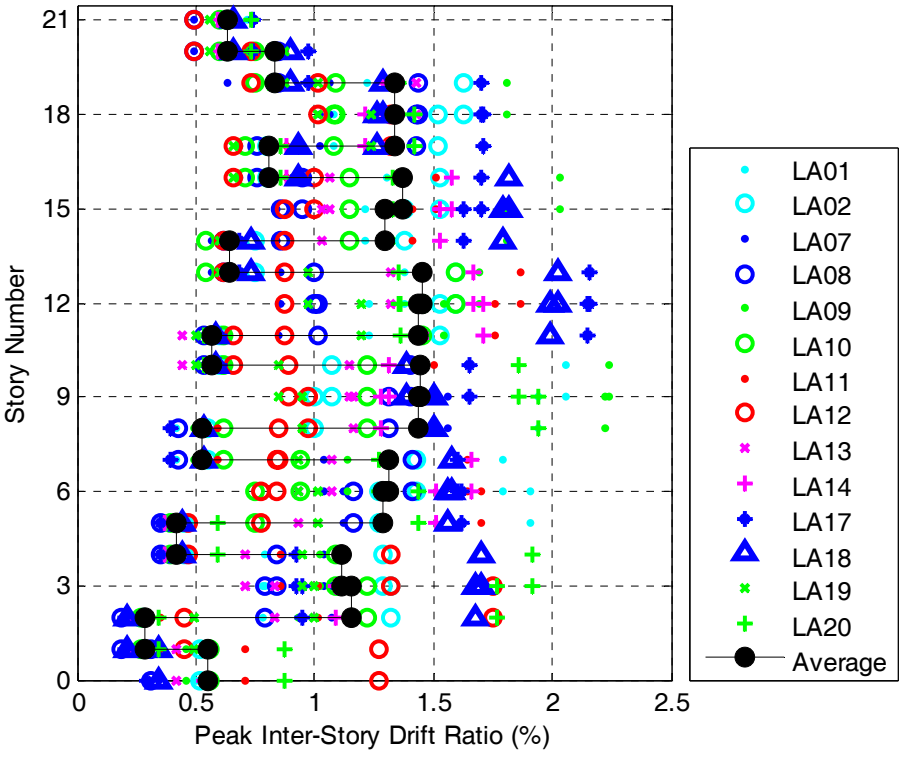

(a)

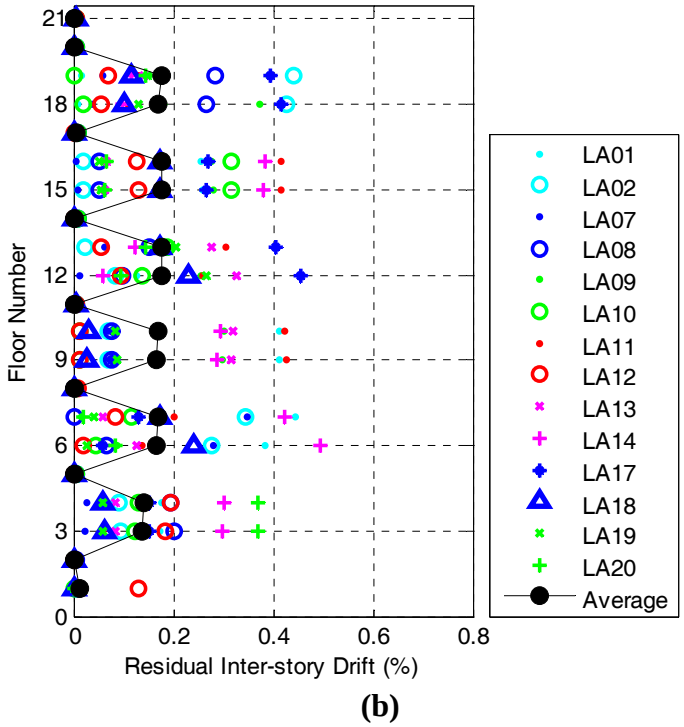

(b)

Figure 4- 8. Case SL-2:(a) Peak inter-story drift ratio; (b) Residual inter-story drift ratio

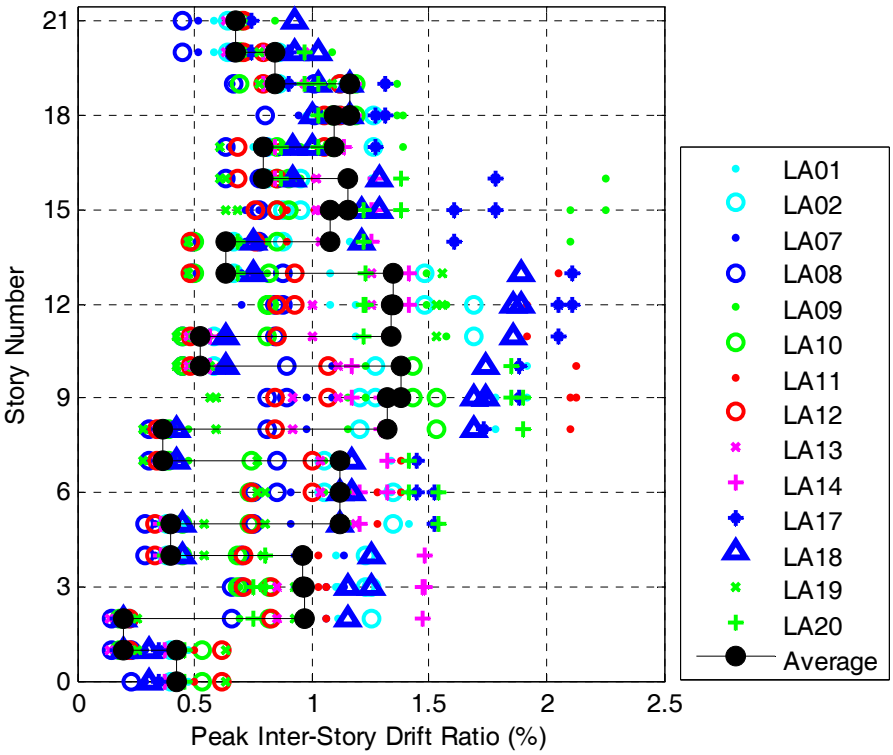

(a)

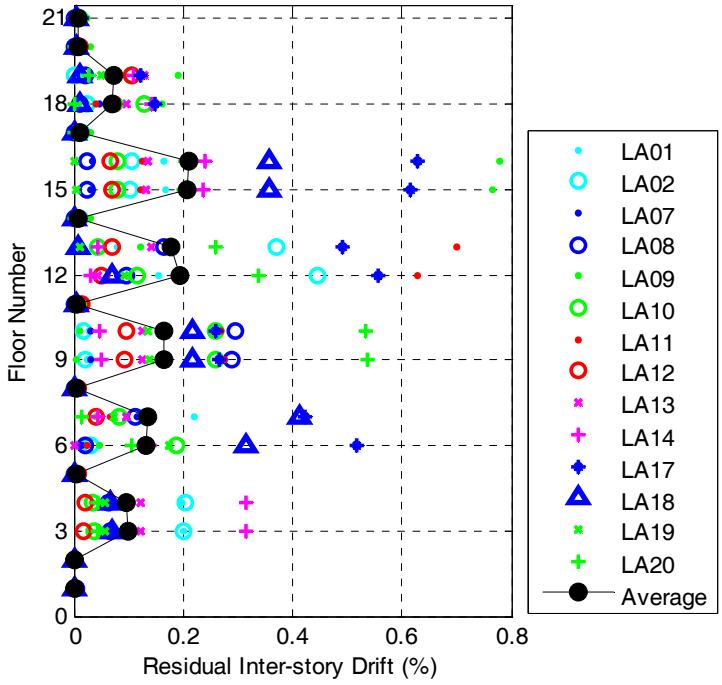

(b)

Figure 4- 9. Case DS-1: (a) Peak inter-story drift ratio; (b) Residual inter-story drift ratio

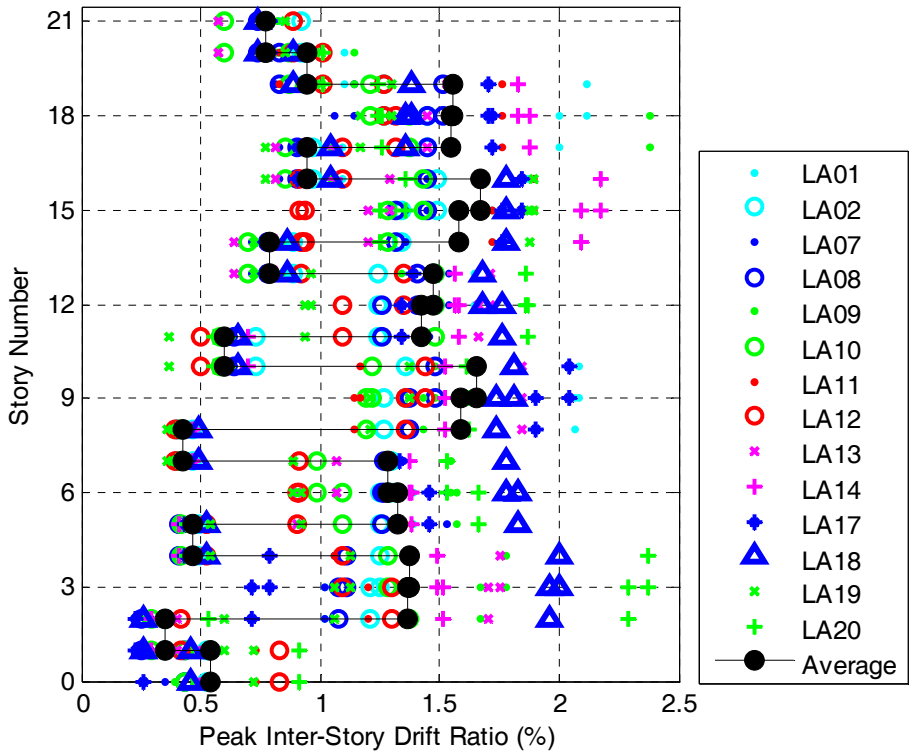

(a)

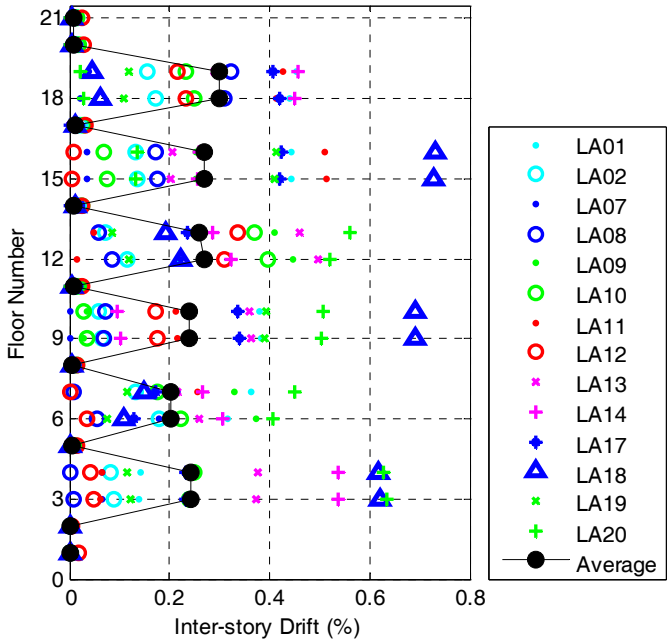

(b)

Figure 4- 10. Case DS-2: (a) Peak inter-story drift ratio; (b) Residual inter-story drift ratio

4.6.4. Link Rotation Demands

The rotation of all shear links was recorded during all time history analyses. The highest value of rotation among the links located at the end of each module is termed peak link rotation in this section. The maximum ensemble average of peak links rotation of 0.0225 radians at link of the 9th floor was observed for the original prototype building in Chapter 3. Also, the maximum rotation of 0.037 radians occurred at the 1st module under the LA20 ground motion. In this section the link rotation demands of parametric study cases are presented. The ensemble average of links rotation of the prototype building is shown with a dashed line in each figure to visualize the comparison.

Figure 4- 11 (a) and (b) show the maximum rotation demand of the links of cases SL-1 and SL-2 under individual ground motions. The link rotation demands are higher for case SL-1 and lower for case SL-2 compared to the original prototype building. These results could be predicted since the link rotation has reverse relation with the link length. The maximum ensemble average of link rotation was observed at the 9th floor similar to the original prototype building but with a higher value of about 0.0265 radians for case SL-1 and lower value of about 0.025 radians for case DS-2. Figure 4- 12 shows the hysteretic behavior of the shear links at the 3rd floor of case SL-1 under the LA18 ground motion, which have the largest link rotation demand among 14 earthquake records. The hysteresis loops of shear links at 9th floor of case SL-2 under LA09 which has the largest rotation demand is shown in Figure 4- 13.

Figure 4- 14 (a) and (b) show the maximum deformation demands of the links of case DS-1 and DS-2 under individual ground motions. The rotation of most of the

shear links are increased for case DS-1 and decreased for case DS-2. The maximum ensemble average of link rotation at 9th floor was about 0.03 radians for case DS-1 and 0.023 radians for case DS-2. Figure 4- 15 shows the hysteresis curve of the shear links at the 9th floor of case DS-1 under the LA01 ground motion. The hysteresis behavior of shear links at 3rd floor of case DS-2 under LA20 which has the largest rotation demand among all time history analyses results is shown in Figure 4- 16.

As a summary of analysis results, it was observed that increasing the length of shear links resulted in lower shear link rotations in case LS-2. For all other cases, the links experienced larger rotations with the most significant increase observed in case DS-1.

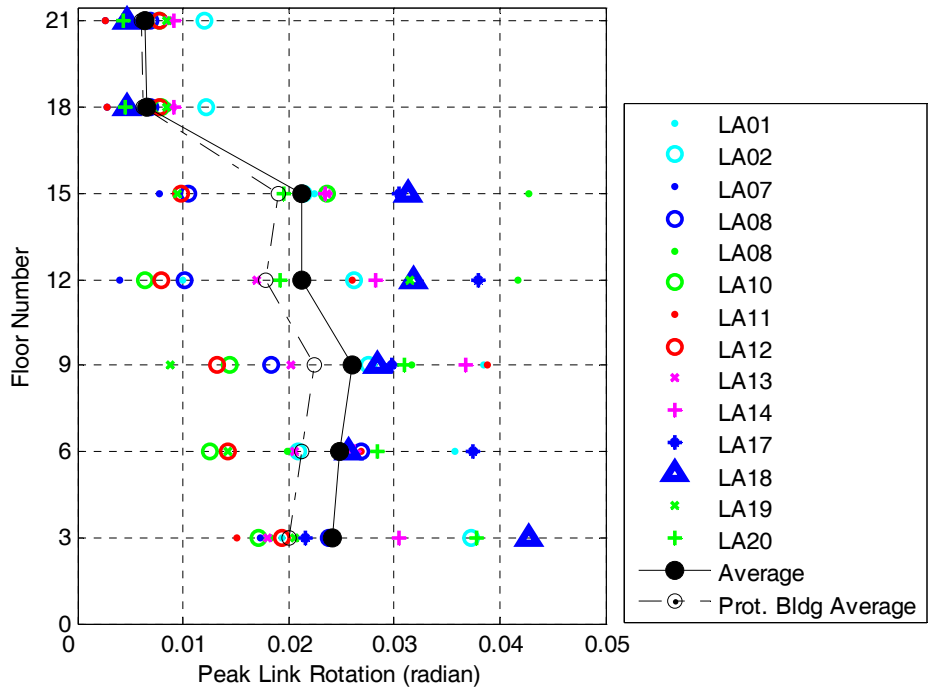

(a)

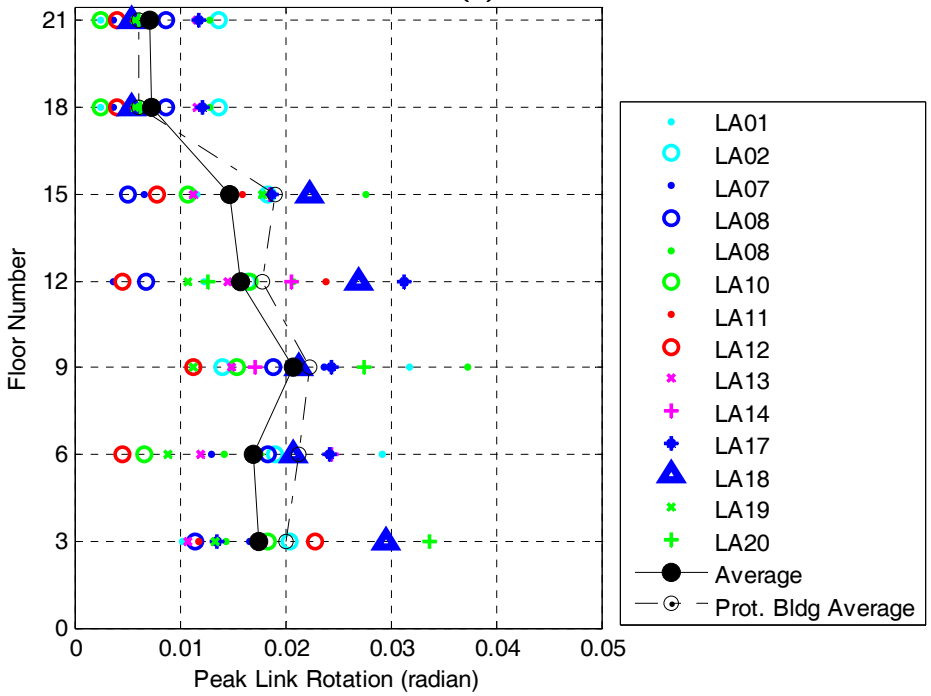

(b)

Figure 4- 11. Distribution of peak rotation demand of shear links under 14 earthquake records: (a) Case SL-1; (b) Case SL-2

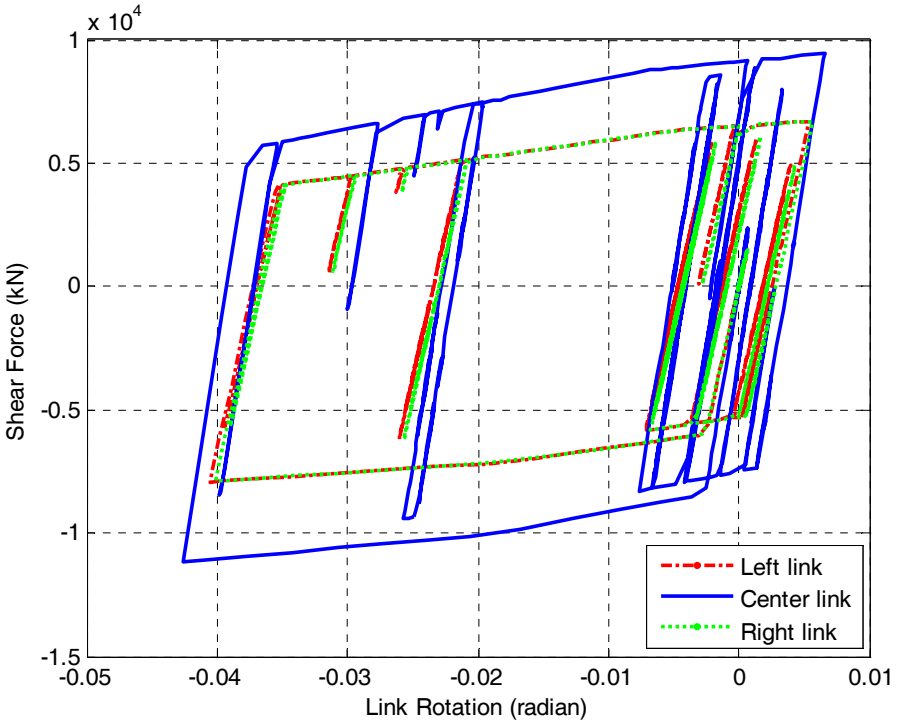

Figure 4- 12. Hysteresis loops of the shear links at the 3rd floor of case SL-1 under LA18

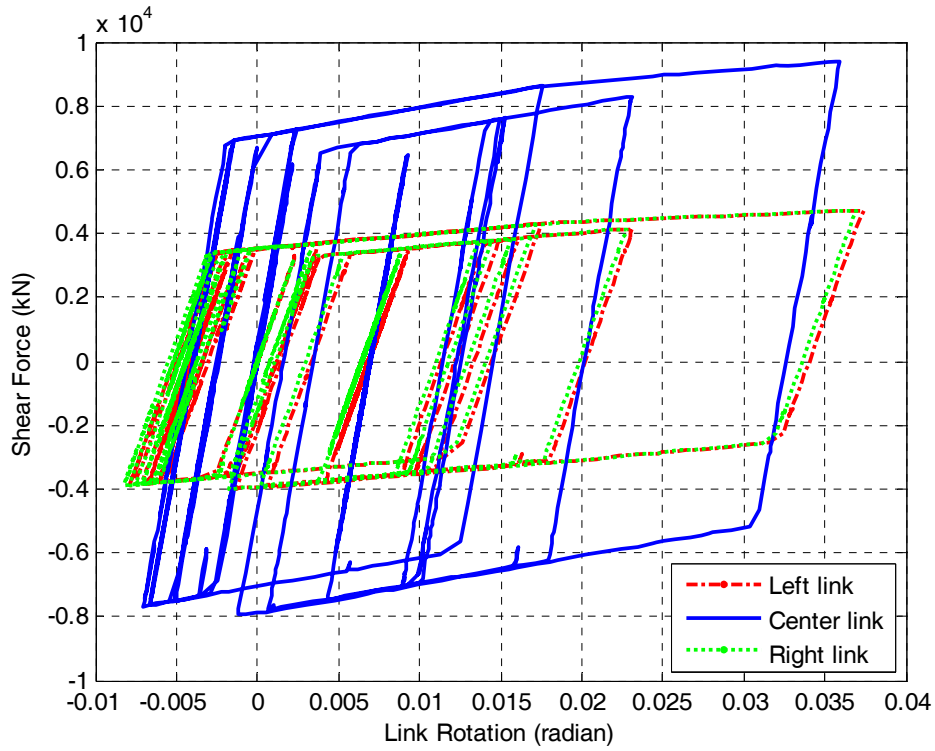

Figure 4- 13. Hysteresis loops of the shear links at the 9th floor of case SL-2 under LA09

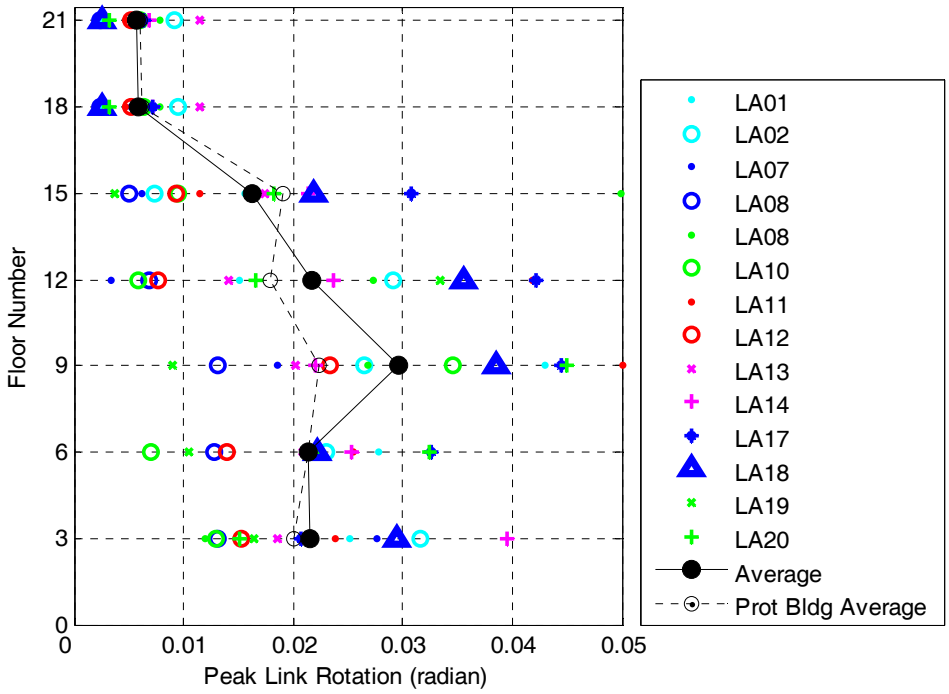

(a)

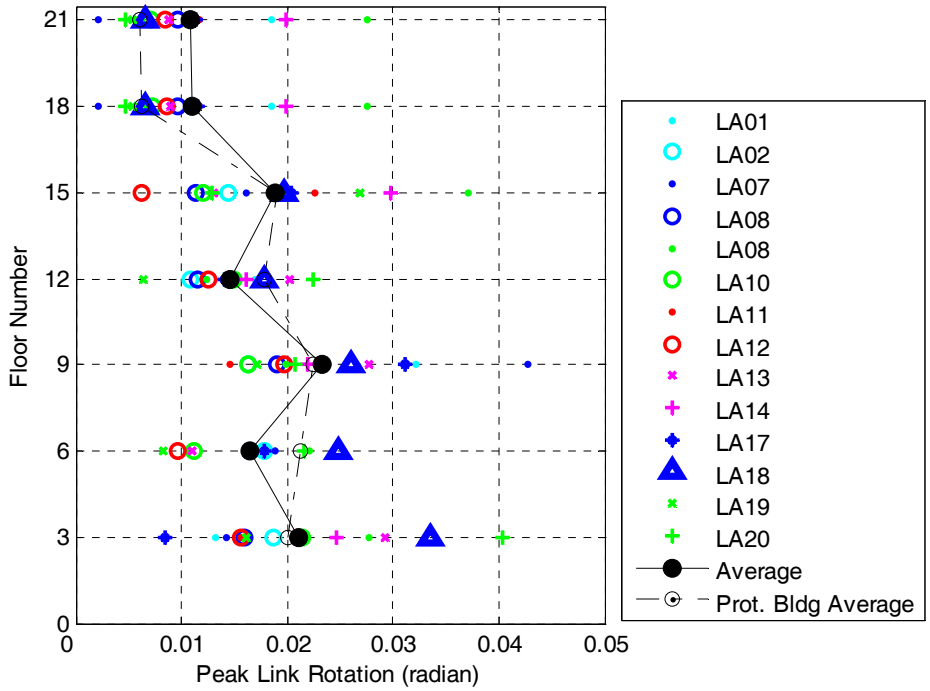

(b)

Figure 4- 14. Distribution of peak rotation demand of shear links under 14 earthquake records: (a) case DS-1; (b) case DS-2

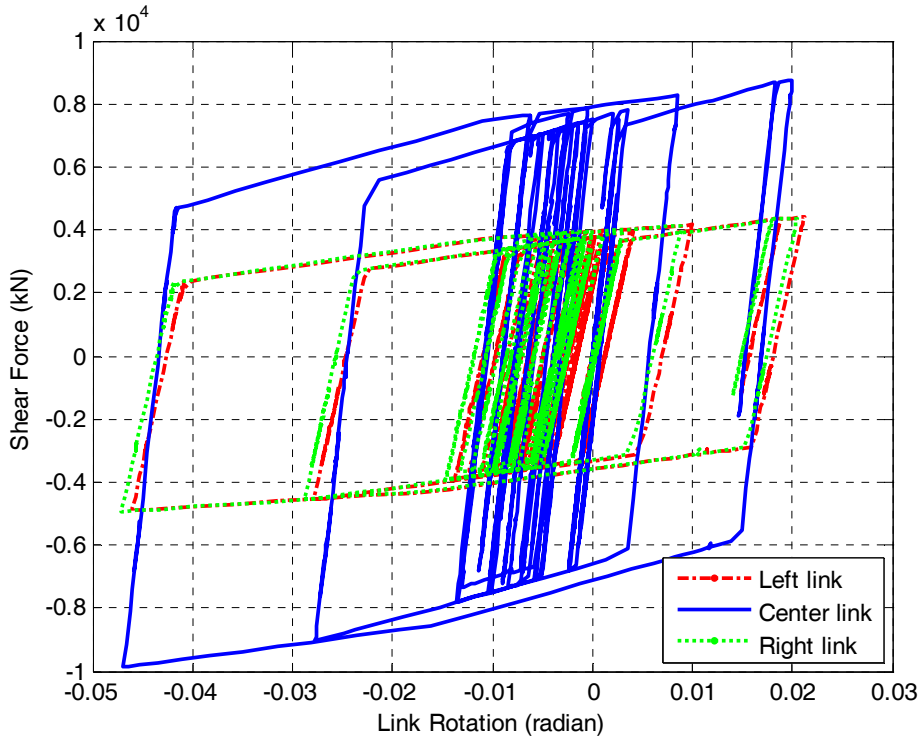

Figure 4- 15. Hysteresis loops of the shear links at the 9th floor of case DS-1 under LA01

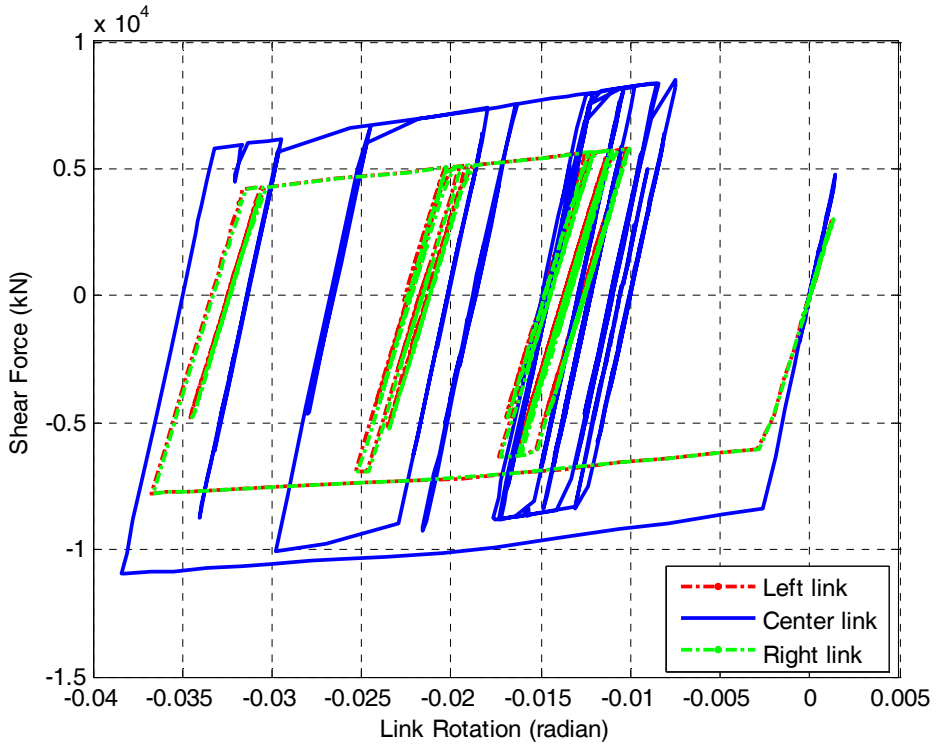

Figure 4- 16. Hysteresis loops of the shear links at the 3rd floor of case DS-2 under LA20

4.6.5. Base Shear Demands

For the prototype building in Chapter 3, the average maximum base shear ratio of the building was around 0.26 and the maximum and minimum base shear ratio of 0.42 and 0.19 occurred under LA12 and LA07, respectively.

The base shear ratios under each earthquake record for cases SL-1 and SL-2 are shown in Figure 4- 17 (a) and (b) . The ensemble average of base shear ratio of case SL-1 is decreased by 12% while it has a higher elastic stiffness compared to the original prototype building. This value increased by 4% for case SL-2 while it has a lower elastic stiffness. The maximum base shear ratio was about 0.34 under LA20 for case SL-1 while the maximum base shear ratio of case SL-2 was 0.47 under LA12. It was observed in Figure 4- 3 (a) that the ductility demand on diagonals of first story decreased for case SL-1 which conforms with the lower base shear ratio results shown in Figure 4- 17 (a). The similar but converse conclusion could be derived for higher base shear ratio for case SL-2.

The base shear ratios under each earthquake record for cases DS-1 and DS-2 are shown in Figure 4- 18 (a) and (b). The ensemble average of base shear ratio of case DS-1 is increased by about 8% compared to corresponding value of original prototype building while it has decreased by about 12% for case DS-2 which has a lower elastic stiffness. The maximum base shear ratio was 0.37 under LA19 for case DS-1. The maximum base shear for case DS-2 was observed under LA20 with a lower value of 0.32. Regular buildings with higher stiffness demand higher base shear. The higher and lower base shear ratios (compared to corresponding values of original prototype

building) obtained for cases DS-1 and DS-2, respectively are in agreement with Eigen value analysis results.

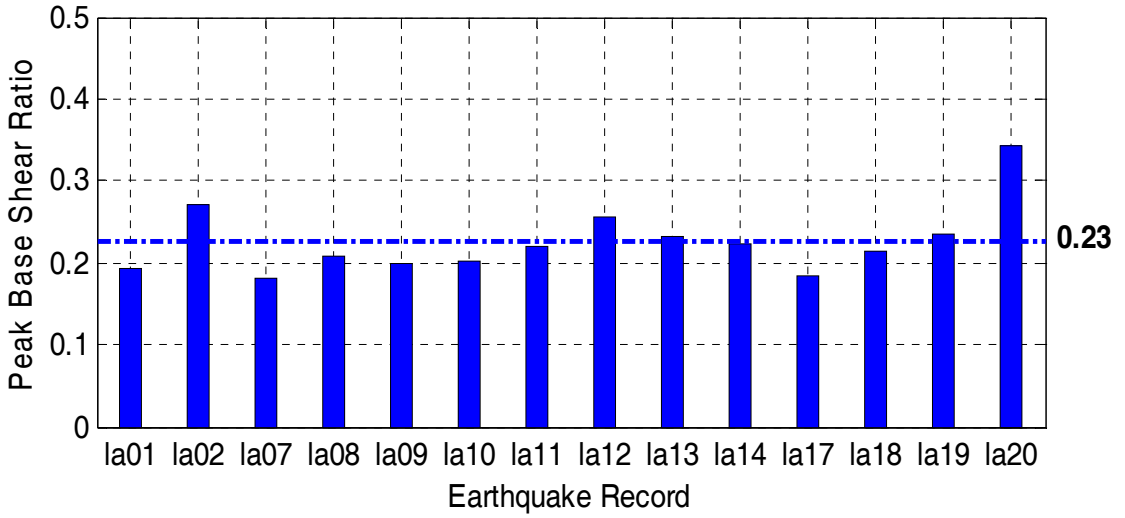

(a)

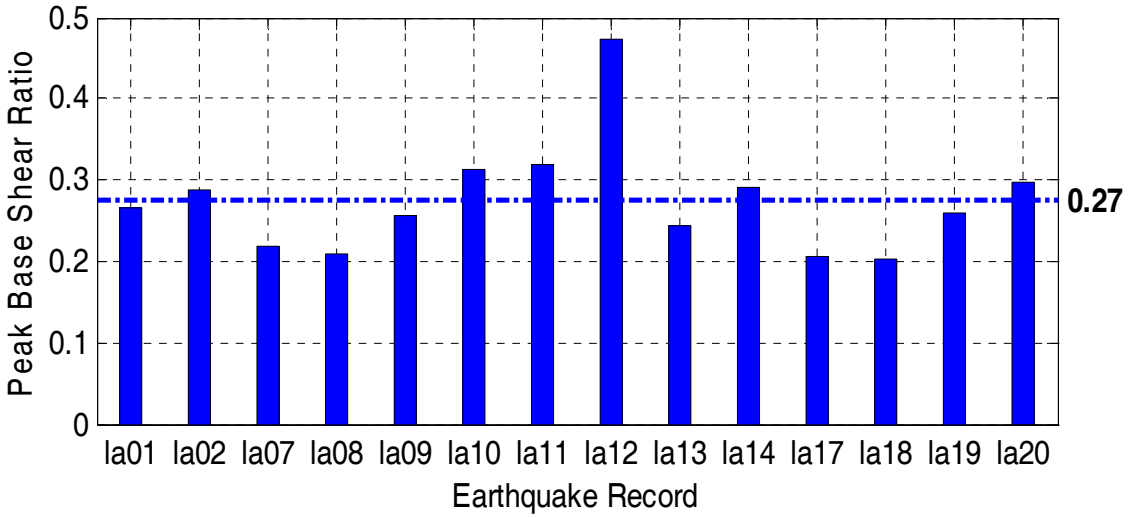

(b)

Figure 4- 17. Maximum base shear of the 21-story HED diagrid frame under 14 earthquake records: (a) Case SL-1; (b) Case SL-2

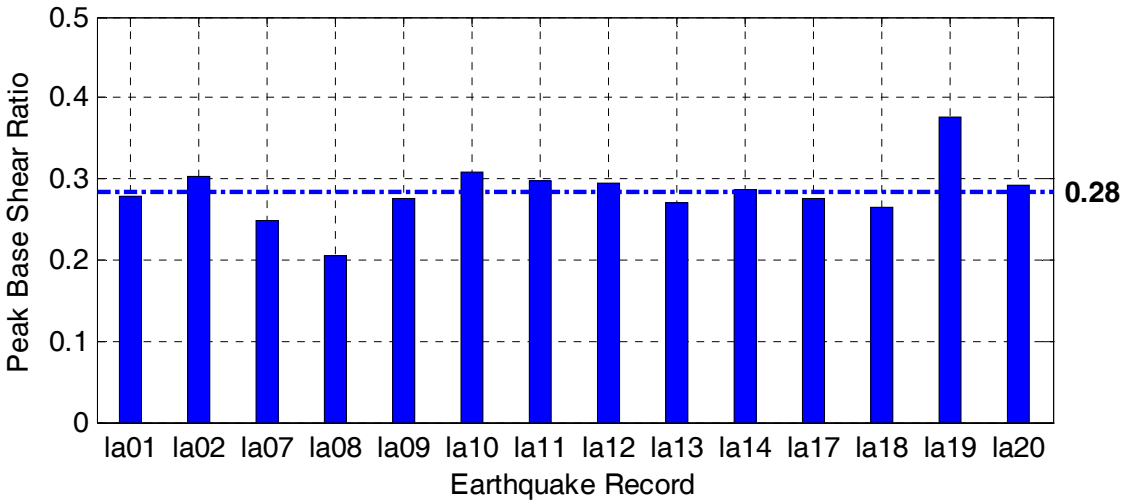

(a)

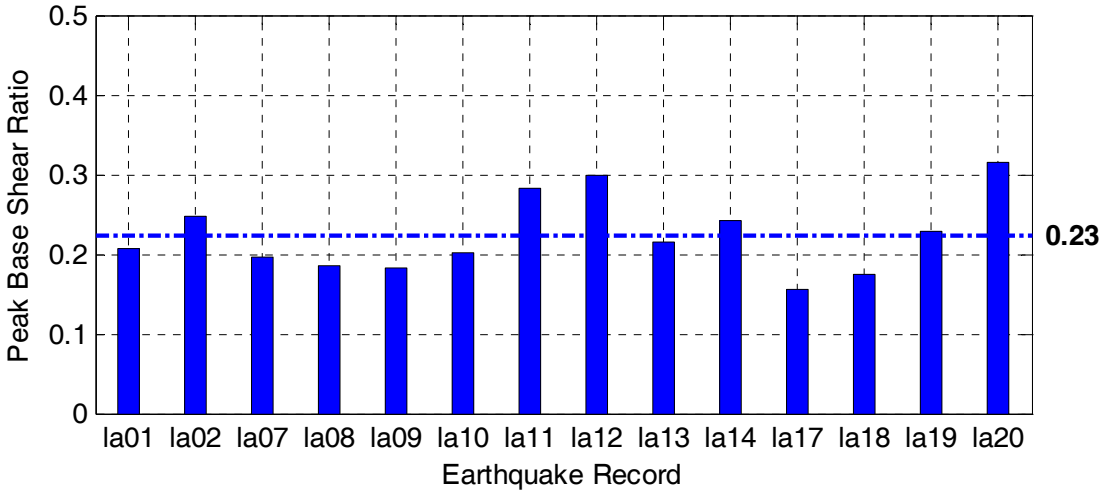

(b)

Figure 4- 18. Maximum base shear of the 21-story HED diagrid frame under 14 earthquake records: (a) Case DS-1; (b) Case DS-2

4.6.6. Floor Acceleration

Figure 4- 19 and Figure 4- 20 show the distribution of peak floor acceleration of the parametric study buildings. The maximum ensemble average of peak floor acceleration of original prototype building previously shown in Figure 3- 30, was about 2.05g recorded at 2nd floor. The maximum peak floor acceleration of was 2.9g recorded at 1st story. Similar patterns were obtained for floors acceleration distribution for all cases with different values for ensemble average of floor accelerations. In all cases the maximum ensemble average of peak acceleration was observed at 2nd floor and the maximum peak floor acceleration was observed at 1st story in most of the cases, similar to the original prototype building.

As shown in Figure 4- 19 (a), the results indicate lower floor accelerations for case SL-1 with the maximum ensemble average of peak floor acceleration of about 1.85g and the maximum peak floor acceleration of 2.85g. On the other hand, higher floor accelerations were obtained for the case SL-2 as shown in Figure 4- 19 (b) with the maximum ensemble average of peak floor acceleration of about 2.4g and the maximum peak floor acceleration of 3.0g.

The fluctuation of floor accelerations were less significant for cases DS-1 and DS-2. It can be seen from Figure 4- 20 (a) that floor accelerations obtained for case DS-1 were similar to original prototype building with the maximum ensemble average of peak floor acceleration of about 2.08g and the maximum peak floor acceleration of 2.84g both occurred at the 2nd floor. For case DS-2, these numbers were 2.35g at 2nd floor and 2.84g at 1st floor, respectively.

In summary of the presented results, only building of case LS-1 showed lower floor accelerations. The cases LS-2 and DS-1 showed higher floor accelerations and the floor accelerations of case DS-1 was similar to that of the original prototype building.

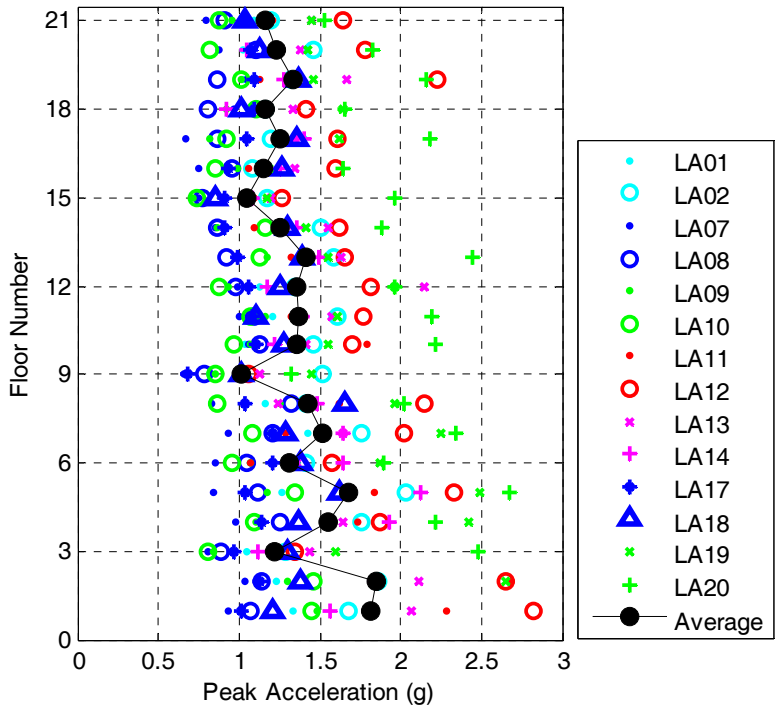

(a)

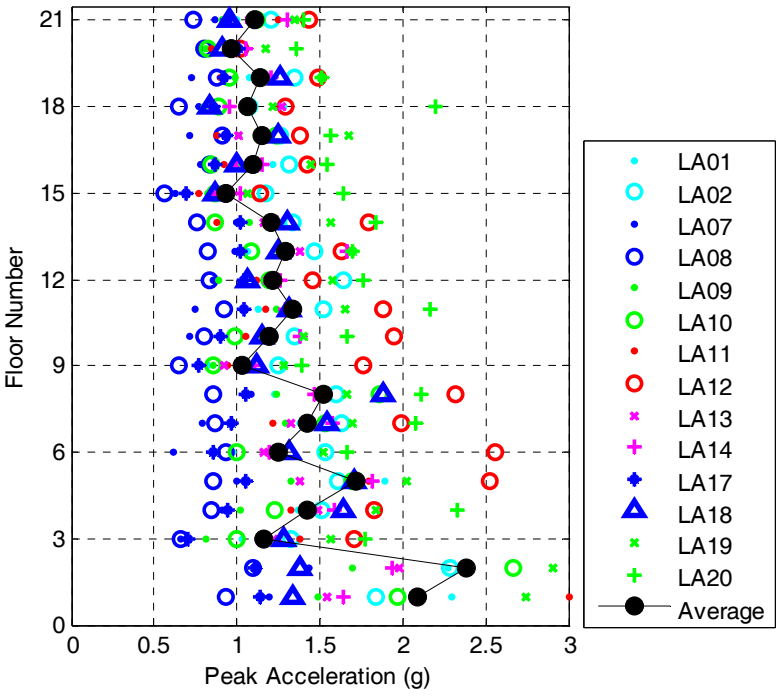

(b)

Figure 4- 19. Distribution of peak floor acceleration of the 21-story HED diagrid building under 14 earthquake records: (a) Case SL-2; (b) Case SL-2

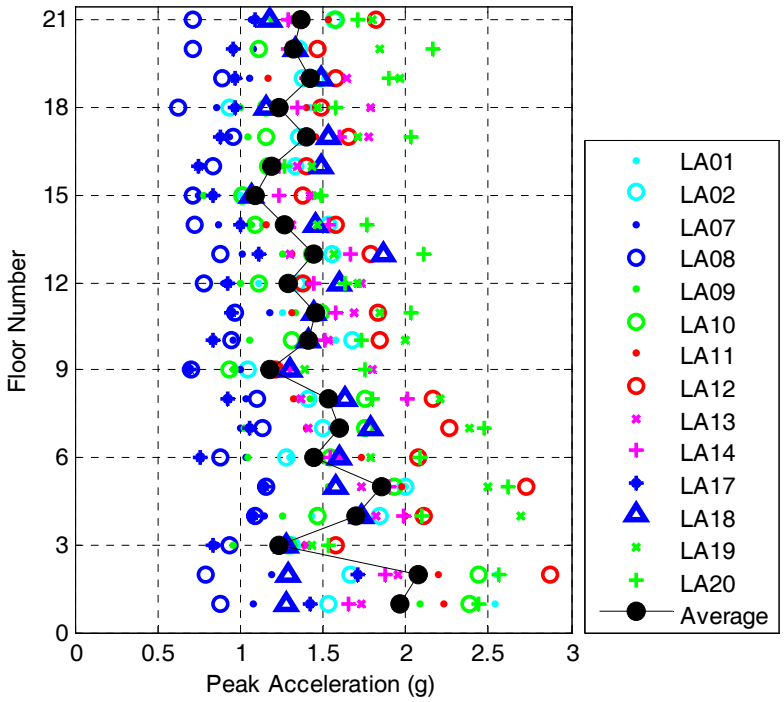

(a)

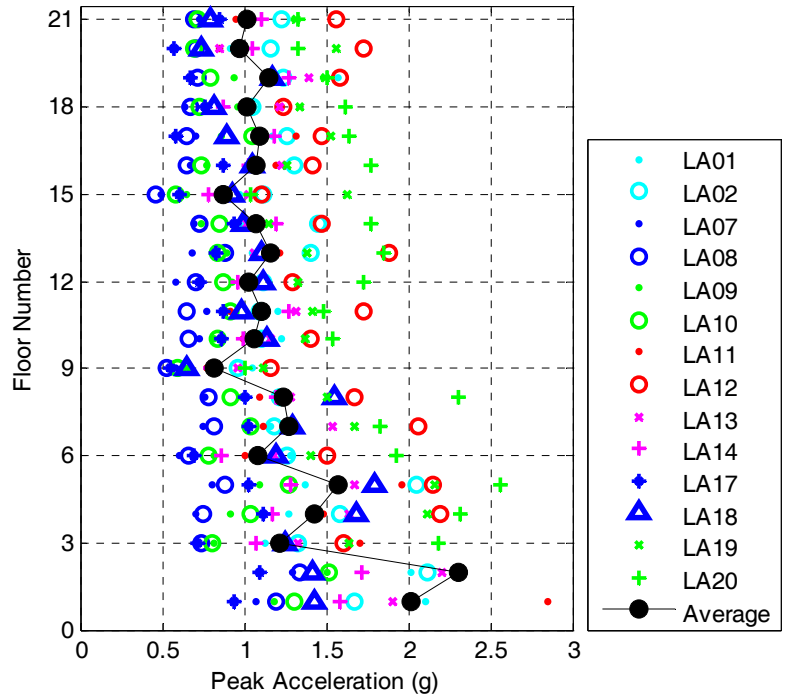

(b)

Figure 4- 20. Distribution of peak floor acceleration of the 21-story HED diagrid building under 14 earthquake records: (a) Case DS-2; (b) Case DS-2

4.7. Comparison of Performance of the Case Studies

The nonlinear static analysis results showed that shear links of cases LS-1 and DS-1 undergo larger rotations at a specific roof drift level compared to the original prototype building. Cases LS-2 and DS-2 with higher fundamental vibration period, showed a reverse behavior meaning that their shear links experienced larger rotations at a specific roof drift level compared to original prototype building.

A summary of the nonlinear time history analysis results of the original prototype building and parametric study cases is given in Table 4- 3. The best results among the five studied buildings are indicated with bold fonts.

No significant change was observed in diagonals ductility demand for cases SL-1 and SL-2, since the ensemble average of peak diagonal ductility demand of the original prototype building with the value of 0.88 at 13^{th} story remained almost unchanged for these two cases. Considerably higher diagonal ductility demands were obtained for case DS-1 with about 27% increase in the ensemble average of peak ductility demand. For case DS-2, the ensemble average of peak diagonal ductility demand did not change; however a ductility demand value larger than one was observed for the diagonals in the 1^{st} and 13^{th} story under LA20 and LA02, respectively.

Slight changes in roof drift ratio for cases SL-1 and SL-2 could be related to the slight difference in the stiffness of these cases as observed from their Eigen value analysis results. The ensemble average of residual roof drift ratio increased by 25% and 50% respectively for cases SL-1 and SL-2. The change in ensemble average of peak roof drift ratios was insignificant for case DS-1 but increased by about 19% for

case DS-2, compared to the corresponding value of 0.58% for the original prototype building. The residual roof drift ratio increased by about 50% and 85% for cases DS-1 and DS-2, respectively. Therefore, no improvement in global displacement demand of HED diagrid building was observed for cases study buildings.

The analysis results showed that the largest ensemble average of peak inter-story drift ratio at 13th story decreased by 6% for case SL-1 and increased by 4% for case SL-2. The ensemble average of residual inter-story drift ratio increased by 10% for case SL-1 with the value of about 0.22% while it decreased by 10% to 0.18% for case SL-2. Decreasing the length of shear link in case SL-1, reduced the inter-story drift ratios while increased the residual inter-story drifts. The ensemble average of peak inter-story drift ratios and residual inter-story drift ratios did not change much for case DS-1 having values of 1.38% and 0.21%, respectively while these values increased considerably by about 19% and 33%, respectively for case DS-2. The significant increase in inter-story drift ratio values of case DS-2 shows that the efficiency of the HED diagrid building decreased with the increase in slope of diagonals which results in lower lateral stiffness.

All cases except SL-2, showed larger link rotations compared to the original prototype building (see row 6th of Table 4- 3). Since the link rotation has reverse relation with the length of the link, longer links in case SL-2 resulted in smaller link rotation. The most significant increase in links rotation was observed in case DS-1 where the 5% decrease in inclination angle of diagonals resulted in 33% increase in ensemble average of peak link rotations and the maximum links rotation reached to 0.05 radians at links of 9th and 15th story under LA11 and LA08, respectively.

From the base shear ratio results, about 12% decrease in base shear ratio was observed for cases SL-1 and DS-2. Cases SL-2 and DS-1 showed a 4% and 8% increase in ensemble average of base shear ratios, respectively compared to that of the original prototype building.

The floor acceleration results showed lower ensemble average of peak floor acceleration for cases SL-1. Floor accelerations generally increased for all other cases.

Table 4- 3. Summary of parametric study results

	Parameter		Original prototype building	SL-1	SL-2	DS-1	DS-2
1	Peak diagonal ductility	Average	**0.88**	0.89	0.88	1.12	0.88
		Maximum	0.98	0.98	1.02	1.45	1.14
2	Peak roof drift ratio (%)	Average	0.58	0.58	0.6	**0.57**	0.69
		Maximum	0.77	0.77	0.78	0.74	0.94
3	Residual roof drift ratio (%)	Average	**0.04**	0.05	0.06	0.061	0.073
		Maximum	0.11	0.12	0.12	0.21	0.17
4	Peak inter-story drift ratio (%)	Average	1.4	**1.32**	1.46	1.38	1.66
		Maximum	2.0	1.99	2.22	2.25	2.38
5	Residual inter-story drift ratio (%)	Average	0.2	0.22	**0.18**	0.21	0.28
		Maximum	0.6	0.61	0.48	0.78	0.73
6	Peak link rotation (radian)	Average	0.0225	0.0265	0.0205	0.03	0.023
		Maximum	0.037	0.0425	0.037	0.05	0.0425
7	Peak base shear ratio	Average	0.26	**0.23**	0.27	0.28	0.23
		Maximum	0.42	0.34	0.47	0.37	0.32
8	Peak floor acceleration (g)	Average	2.05	**1.85**	2.4	2.08	2.35
		Maximum	2.9	2.8	3	2.84	2.84

4.8. Summary and Conclusions

A parametric study on the effect of shear links' length and slope (i.e., inclination angle) of diagonals on seismic performance of the HED diagrid building was conducted in this chapter. The nonlinear static and nonlinear time history analysis were performed on four case studies under 14 strong earthquake records (scaled for the design basis earthquake level for Los Angles, California) using the finite element model developed in OpenSees. The length of shear links was decreased by 20% for case SL-1 and increased by 20% for case SL-2. The diagonals angle was decreased by about 5% for case DS-1 and increased by 5% for case DS-2. The results of each engineering demand parameter for all study cases were presented and compared with the original prototype building of Chapter 3.

There are different engineering demand parameters that can be considered to assess the seismic performance of a building. The seismic performance of HED diagrid building is affected by different parameters such as the capacity and length of shear links as main energy dissipation components, geometry and configuration of the building including the aspect ratio of the building and slope of diagonals and the size of the diagonals. The link rotation demand seems to be the most influential factor affecting the seismic performance of the building which itself depends on the length of the links and geometry of the building. Therefore the shear links should be designed properly to satisfy the desired performance objectives based on the most important engineering demand parameters of any specific design case.

Decreasing the length of shear links in case SL-1, seemed to have a positive effect on performance of the HED diagrid building. A 6% decrease in ensemble

average of peak inter-story drift ratios, lower base shear demand, lower floor accelerations and almost no significant negative effect on other local and global deformation demands and diagonals ductility demands is the basis for such conclusion.

There was no considerable improvement in EDPs results of case SL-2 except for residual inter-story drift ratio which showed 10% decrease in ensemble average value.

No improvement in any of engineering demand parameters was observed for cases D-S-1 and DS-2 which had different inclination angle of diagonals. The most significant changes in performance of case DS-1 with decreased inclination angle of diagonals were observed in ensemble average values of residual roof drift ratio and peak link rotation both increased by 50% and 33%, respectively.

CHAPTER 5 : GFRP-TUBE CONFINED CONCRETE CYLINDERS WITH HIGH CONFINEMENT VOLUMETRIC RATIO: CONSTITUTIVE BEHAVIOR

5.1. Introduction

The effect of lateral confinement on increasing the strength and ductility of concrete elements is known for years and applied in different forms with the most well-known form of transverse reinforcement with steel rebar. This chapter presents the results of an experimental study on glass fiber reinforced polymer (GFRP)-tube confined concrete with higher GFRP volumetric ratio under monotonic and cyclic compressive loading, as well as constitutive modeling. The performance of lightweight concrete encased in such GFRP-tube was also experimentally studied. The confinement volumetric ratio of GFRP in this study is higher than the data range reported in previous experimental studies on GFRP confined concrete conducted by different researchers. The hardening behavior of confined concrete intensifies as the volumetric ratio of FRP (fiber reinforced polymer) increases. Also the rupture of the FRP tube that is the mostly observed failure mode of FRP confined concrete and other possible failure modes are postponed in thicker tubes.

A monotonic as well as a hysteretic constitutive model are proposed for GFRP confined concrete with high confinement volumetric ratio and calibrated with the experimental data. The constitutive model was implemented into a finite element

analysis platform in the form of a uniaxial material to enable nonlinear analysis of complex structures utilizing this type of confined concrete elements.

5.2. Research Background

ACI 440.2R-08 classifies the strain-stress behavior of concrete compression elements to unconfined, lightly confined (e.g. transverse reinforcement), heavily confined with softening behavior (e.g. steel tube) and heavily confined with hardening behavior (e.g. fiber reinforced polymer (FRP) confinement), as shown in Figure 5- 1. In this figure, f'_{co} is the plain concrete strength and f_{cc} is the ultimate strength of confined concrete. The research on concrete filled steel tube (CFT) started at 1961 in Japan (Morino and Tsuda, 2001) and several buildings in Seattle, Washington exploited certain advantages of CFT in their columns in the mid-1980s (Hajjar et al. 1998; Schneider, 1998). Application of FRP materials as confining devices started in 1990s for retrofitting of concrete columns (Saadatmansh et al. 1994). Since then, FRP materials are used extensively in construction industry in forms of filaments, wraps or tubes depending on type of application.

FRP confined concrete shows a hardening stress-strain behavior and enhances strength, ductility, durability and energy absorption capacity of the element. The stress-strain behavior of concrete confined with FRP is different from steel confinement; in CFT elements, once the steel yields the tube exerts only a limited constant confining pressure to the concrete equal to:

$$\sigma_R = \frac{2f_y t}{D} \tag{5.1}$$

where f_y is the yield strength of steel and t and D are the thickness and inside diameter of the steel tube. On the other hand, FRP material has elastic confinement action which continuously increases the confinement pressure until rupture of the fibers (Samaan et al. 1998). Dissimilar to steel, FRP limits the dilation tendency of concrete, as it reverses the direction of volumetric strains (Mirmiran and Shahawy, 1997).

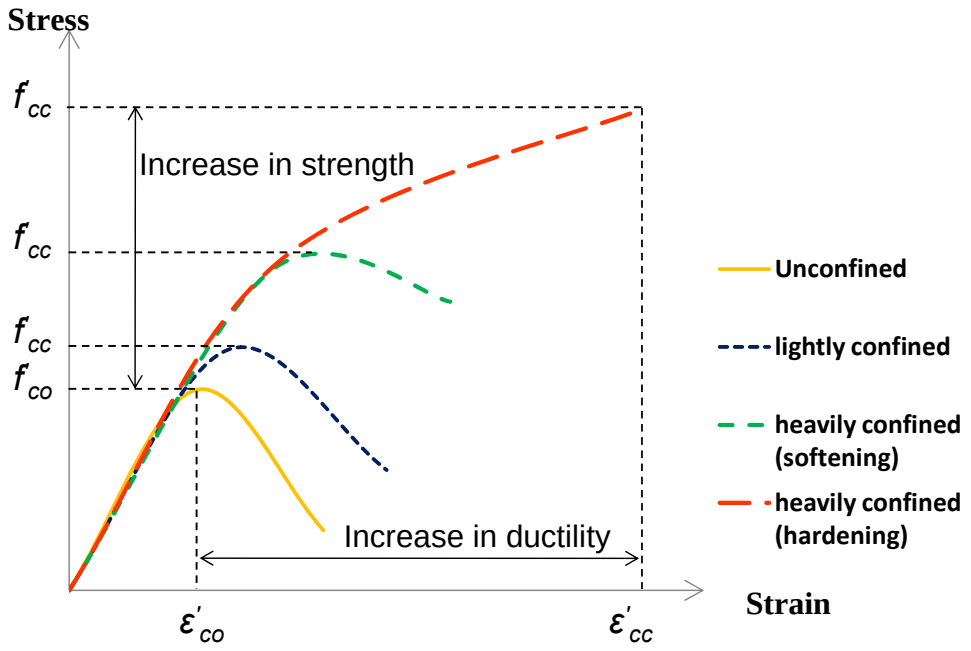

Figure 5- 1. Schematic stress-strain behavior of concrete under compression

In retrofitting and strengthening of damaged concrete, thin layers of FRP materials are used to wrap the element (Nanni and Bradford, 1995; Buyukozturk and Hearing, 1998; Parvin and Wang, 2001). In new construction applications, FRP tubes in which the fibers are mainly oriented in hoop direction to provide the maximum stiffness and strength for confinement are used (Fam and Rizkalla, 2001a; Li, 2006;

Zhu, 2006). FRP tube has certain advantages as confining device in hybrid concrete construction including: extremely high strength-to-weight ratio; high durability; high resistance to corrosion, chemicals and abrasion; structurally integrated stay-in-place formwork; ; improving flexural stiffness of concrete because of bonding action and axial stiffness of FRP tube. Because of these benefits, FRP tube has become popular as confining device for concrete to enhance ductility and strength (e.g., Teng et al. 2007b)

While the most observed failure mode of FRP tubes under compression is rupture of the fibers, results of experimental studies show that the maximum deformation of glass fiber reinforced polymer (GFRP) tube is almost twice as large as similar carbon fiber reinforced polymer (CFRP) tube which has an ultimate confinement pressure of only about 50% higher than GFRP confinement. This fact makes GFRP tubes a promising choice for structural members desired to have high ductility especially in seismic regions. In the study conducted by Shao and Mirmiran (2004), it is shown that with a proper design, GFRP tubes can be used as primary and sole reinforcement of concrete filled FRP-tube (CFFT) columns for concrete structures in seismic regions providing a ductility level comparable to conventional reinforced concrete columns.

5.3. Research Motivation

The volumetric ratio of confinement has similar values in most of the studies conducted on CFFT in the past with the ratio of tube thickness to core diameter (t/D) ranging between 0.3% to 4.2% (e.g. Mirmiran and Shahawy, 1997; Saafi et al., 1999; Fam and Rizkalla, 2001; Lam et al., 2006; Shao et al., 2006; Mohamed and Masmoudi, 2010). Also there are limited experimental data on behavior of GFRP-tube confined concrete under cyclic axial loading. As part of this research, the behavior of light weight and normal concrete encased in relatively thicker GFRP tubes under static and cyclic axial loading is experimentally investigated. The rupture of tube fibers which is the main failure mode of FRP-tube confined concrete can be postponed by increasing the volumetric confinement ratio. This type of endurable axial element with high ductility and strength is promising for use in seismic resistant structures as braces or columns. With the aim of using such confined concrete elements as diagonals in diagrid structure, the hysteretic behavior of GFRP-tube confined concrete with high confinement ratio is studied experimentally and analytically.

For performance based earthquake engineering, ability of accurate numerical simulation is essential. It is thus critical to be able to accurately model the hysteretic behavior of these elements for seismic analysis of the structures utilizing these elements. With the purpose of developing such analytical tool, the proposed constitutive model for GFRP tube confined concrete in this study has been implemented in the general finite element software program, OpenSees.

5.4. GFRP-Tube Confined Concrete

FRP tube provides passive confinement for confined concrete core since the confining action comes to play through lateral expansion of concrete under axial loading. The lateral strain initiated and increased by axial stress imposed on concrete, activates the confining device and FRP tube resists the expansion of the core concrete. Drawing the free body diagram of confined concrete (see Figure 5- 2), the equilibrium requires the tensile hoop stress to be balanced by the uniform radial pressure (Lorenzis, 2003).

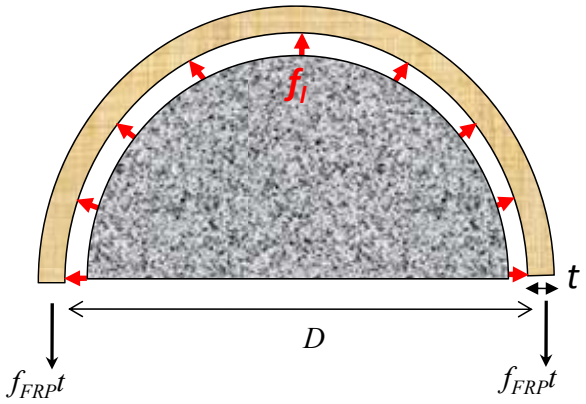

Figure 5- 2. Confined concrete-tube interface interaction

The confinement pressure exerted by FRP tube before rupture of the fibers is evaluated by the following equation:

$$f_{lu} = \frac{2f_{FRP}t}{D} \tag{5.2}$$

where f_{FRP}, t and D are the hoop tensile strength, thickness and inner diameter of the FRP tube, respectively. The confinement is shown to be effective in increasing the

strength of the concrete if the confinement effectiveness is greater than 0.3 (Shao et al, 2006). The confinement effectiveness, *CE*, is the ratio of lateral pressure exerted by FRP tube to plain concrete strength:

$$CE = \frac{f_{lu}}{f'_{co}} \tag{5.3}$$

The confinement effectiveness is mainly affected by confinement volumetric ratio that is calculated from the following equation for fully FRP-encased concrete specimens:

$$\rho_f = \frac{A_{tube}}{A_{core}} = \frac{4t}{D} \tag{5.4}$$

Most of previous research works on FRP-tube confined concrete have the confinement effectiveness ratio ranging between 0.1 and 0.8 and are mainly focused on monotonic compressive behavior of confined concrete, while there is not much research on hysteresis behavior of such elements under cyclic loading (Varma et al. 2009). The main goal of this study is to investigate the performance of GFRP-tube confined concrete with higher confinement volumetric ratio than typically used in previous researches. A larger increase in strength and ductility of the concrete is anticipated with increasing the confinement volumetric ratio through increasing the tube thickness to diameter ratio (*t/D*). In addition, the main and almost only failure mode of GFRP-tube confined concrete specimens observed in experimental researches which is the rupture of the tube (Lam and Teng, 2002) can be postponed. Also ticker tube provides additional bending resistance under eccentric loading that usually happens in the axially loaded elements.

In this study, experimental tests were conducted to evaluate the performance of concrete encased in GFRP-tube with high volumetric ratio under static and cyclic axial loading. The performance of lightweight concrete confined with these tubes is also investigated in which the core load transfer element is weaker than other specimens because of the low strength concrete. The appropriate equations to predict the ultimate stress and strain of tested specimens and a constitutive model to simulate their monotonic and hysteretic behavior is presented and implemented into the OpenSees to provide an analytical tool for analysis of structures having axial elements of this type.

5.5. Experimental Study

5.5.1. Specimen Specifications

A total of 12 GFRP-tube confined concrete specimens and eight plain concrete cylinders were casted for monotonic and cyclic axial compression testing. The GFRP tubes specifications are as follows: eight GFRP tubes with inner diameter of 158 mm (6.21 inches) and height of 280 mm (11 inches), four of which were filled with light-weight concrete and the other four were filled with normal concrete. Four other GFRP tubes had an inner diameter of 101 mm (3.98 inches) and height of 168 mm (6.6 inches) filled with normal concrete. Experimental results of studies on FRP confined concrete confirmed the findings that the confinement effectiveness of FRP tubes depends little on the size and length-to-diameter ratio of test specimens, as reported by Lam and Teng (2002).

Table 5- 1 shows the properties of the specimens. The GFRP-tube filled with light-weight concrete was labeled as GLC and the large and small tube-confined normal concrete specimens were labeled with GNC-1 and GNC-2, respectively.

Table 5- 1. Properties of GFRP-tube confined concrete cylinder specimens

Specimen name	# of samples	Inner diameter (mm)	Height (mm)	f'_{co} (MPa)	t_f (mm)	t/D	$\frac{f_{lu}}{f'_{co}}$
GLC	4	158	280	9.6	11.43	0.072	3.24
GNC-1	4	158	280	28	11.43	0.072	1.11
GNC-2	4	101	168	28	8.64	0.085	1.32

5.5.2. Material Properties

The GFRP tubes used in this study are machine-made composite material produced by filament winding high strength continuous glass fiber filaments in 6 and 60 degrees saturated with corrosion resistant epoxy resin. The epoxy resin is an aromatic amine, heat cured system that has a high mechanical strength and thermal and corrosion resistance. The value of *t/D* for large and small tubes is 7.2% and 8.5% respectively. The thickness of the tubes is 11.43 mm and 8.64 mm for large and small tubes respectively, which is large enough to get the confinement effectiveness ratio larger than 1. The tensile hoop strength and rupture strain of tubes due to internal pressure are 216 MPa (31.3 *ksi)* and 0.02 respectively (manufacturer supplied data) and the same for both tube sizes since their winding angle configuration is slightly different.

The light-weight concrete was designed as a ductile concrete using fibermesh and mixed in one batch. The normal concrete was made using a supplier ready mix and was mixed in three batches. The density of light-weight and normal concrete were 900 kg/m^3 and 2320 kg/m^3, respectively. The ultimate strength and strain of plain concrete, (f'_{co}, ε_{co}), obtained from testing the 28-days cylinders were 9.5 MPa (1.38 ksi*)* and 0.006 for light-weight concrete and 30±2 MPa (4.33 ksi*)* and 0.005 for normal concrete. The modulus of elasticity of the lightweight and normal concrete were 2.24 GPa (325 ksi) and 7.24 GPa (1050 ksi) respectively.

5.5.3. Instrumentation and Test Procedure

The 400-kips capacity SATEC universal test machine was used to test the specimens under compression. The load was transferred to the concrete core through two thick steel disks placed at both ends of the specimen (Figure 5- 3) and hence GFRP tube was not exposed to any axial load since it is known that loading of tube reduces the confinement effectiveness (Fam & Rizkalla, 2001a). The diameter and height of the steel disks used to transfer the load to the concrete core were 153x38 mm for the large specimens and 99x38 mm for the smaller specimens.

The data acquired by the testing machine was used for axial strain and stress. Two strain gages installed at the mid-height of the specimens on GFRP tube surface to obtain the hoop strain. The monotonic and cyclic loading was imposed on the specimens under force control with stress rate of 15 MPa/min. Two different cyclic loading histories were designed, one with three repetitive cycles at three load levels corresponding to unconfined concrete strength and 40% and 75% of maximum capacity of the testing machine to observe the strength degradation and the other with ascending load cycles at 134 kN (30 kips) load amplitude increment.

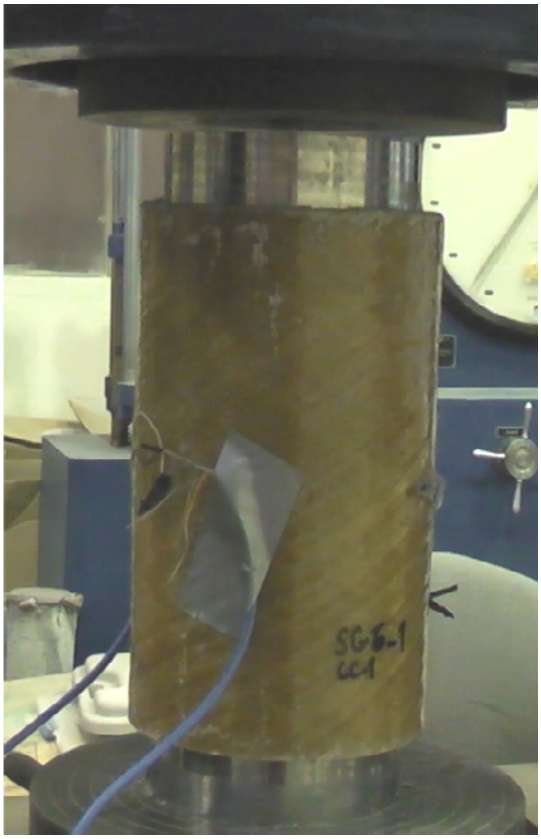

Figure 5- 3. Test setup

5.6. Test Results

5.6.1. Lightweight Concrete

Figure 5- 4 shows the experimental results of GFRP-tube confined lightweight concrete under monotonic compression. Low dilation of lightweight concrete because of its low strength results in low internal pressure exerted to the GFRP tube; hence the GFRP-tube confined concrete does not show a sharp hardening behavior. The stress-strain curve is almost bilinear and the intersection point of two linear branches denotes the initial failure of the unconfined concrete core (Saafi et al., 1999).

The failure of load carrying capacity of concrete core is increased by approximately 35% and after that there is a significant increase in ductility but a limited increase in load carrying capacity of the specimen. The lightweight concrete as a load transfer element was condensed under axial load because of its loose structure and low strength and therefore failed to pressurize the tube effectively. With normal concrete core, it was observed in the experiments of other researches that the concrete starts to expand excessively at a stress level of approximately 87% of the unconfined strength (Fam and Rizkalla, 2001b) and at that point the GFRP starts its confinement action due to the hoop pressure exerted by concrete.

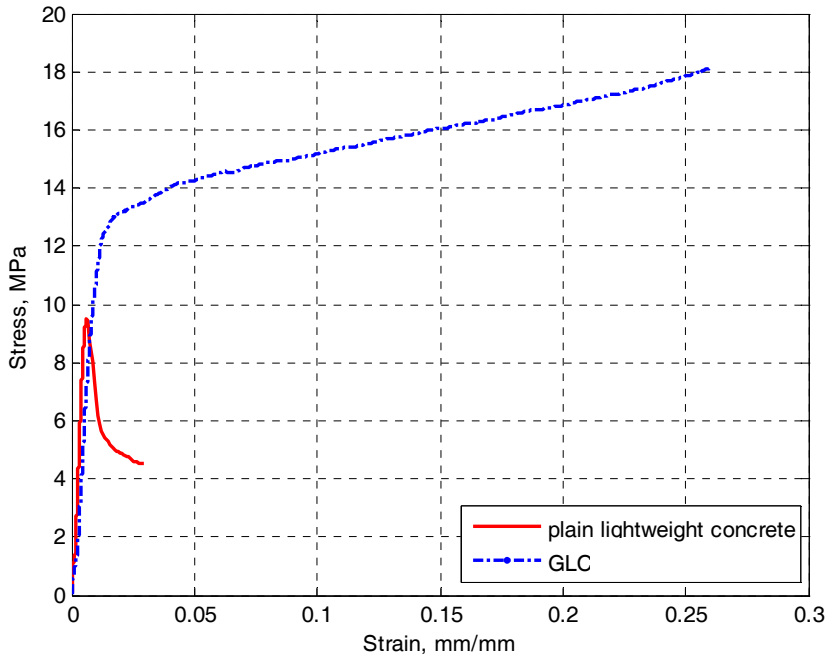

Figure 5- 4. Uniaxial response of GFRP-tube confined lightweight concrete under monotonic loading

5.6.2. Normal Concrete

5.6.2.1. Monotonic Loading

Figure 5- 5 shows the axial stress-strain curve of plain concrete and GFRP-tube confined specimens with normal concrete. The lateral strain of the specimen with 101-mm inner diameter tube is also shown at negative side of the strain axis which is the average of the data obtained from two strain gages installed at the mid-height of the GFRP tube. The initial stiffness of the confined specimens are expected to be similar to that of the plain concrete specimen as observed in most of other researches

on FRP-confined concrete, however the test results on tested specimens display a lower initial stiffness value which is believed to result from not perfectly flat end surfaces of concrete core of the test specimens since capping was not possible because of confinement.

A significant increase in strength of the concrete is observed as a result of sharp hardening slope of the test specimens. The tests were stopped at the load capacity limit of the SATEC testing machine and no physical damage was observed in the GFRP tubes. Only two of the GNC-1 specimens were tested under monotonic compression loading since at the load capacity limit of the 400-kips SATEC testing machine, the ultimate stress of the test specimen cannot be reached. The hardening slope of GNC-1 specimens are lower than GNC-2 since the latter has a higher volumetric ratio of GFRP tube.

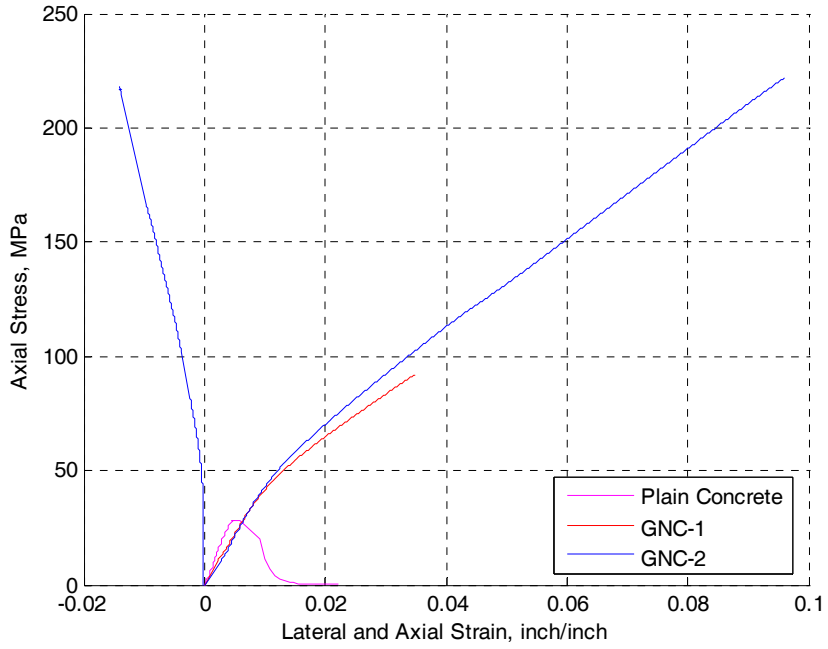

Figure 5- 5. Uniaxial response of unconfined and GFRP-tube confined normal concrete under monotonic loading

Figure 5- 6 shows a comparison between the test results of this study with two other concrete-filled GFRP tube experimental tests by Mirmiran and Shahawy (1997) and Mohamed and Masmoudi (2010). The experimental results of these two studies are selected for comparison because they have used relatively higher FRP confinement ratio among previously reported research works on GFRP-tube confined concrete. In the selected test specimens from the above mentioned studies, the plain concrete strength was similar to the test specimens of this study, with the value of 32 MPa for the specimens of Mirmiran and Shahawy (1997) and 30 MPa for the specimens of Mohamed and Masmoudi (2010).

In the tests performed by Mirmiran and Shahawy (1997), a total of 24 concrete-filled GFRP tube specimens with three different volumetric ratios of GFRP were tested under compression. The monotonic stress-strain curve of specimens with highest FRP volumetric ratio ($t/D = 3/152.5 = 2\%$) and confinement effectiveness of 0.79 is shown in Figure 5- 6. The load carrying capacity and ductility of the specimens were increased by approximately 2.6 and 14 times respectively compared to plain concrete.

In the experimental study of Mohamed and Masmoudi (2010), a total of 23 CFFT specimens with different concrete strength and some with steel reinforced concrete were subjected to compression loading. The result of concrete-filled GFRP tube specimen (no steel reinforcement, f'_c=30 MPa) with highest confinement ratio ($t/D = 6.4/152 = 4.2\%$) and confinement effectiveness ratio of 1.1, indicates that the concrete strength was increased by 4.23 times as shown in Figure 5- 6.

The ultimate stress and strain of the test specimens of this study are calculated from the equation presented in the following sections because the specimen did not fail when the machine load limit was reached. The stress-strain curve of the GNC-1 specimen with almost the same confinement effectiveness ratio as the specimens tested by Mahamed and Masmoudi (2010) shows a similar hardening slope but a significantly higher ductility (about 325%) because of 70% more confinement volumetric ratio. The hardening slope of both GNC-1 and GNC-2 specimens are significantly higher than the test results of Mirmiran and Shahawy (1997) because of their higher confinement effectiveness ratio. Their ductility is also much larger as a result of higher confinement volumetric ratio.

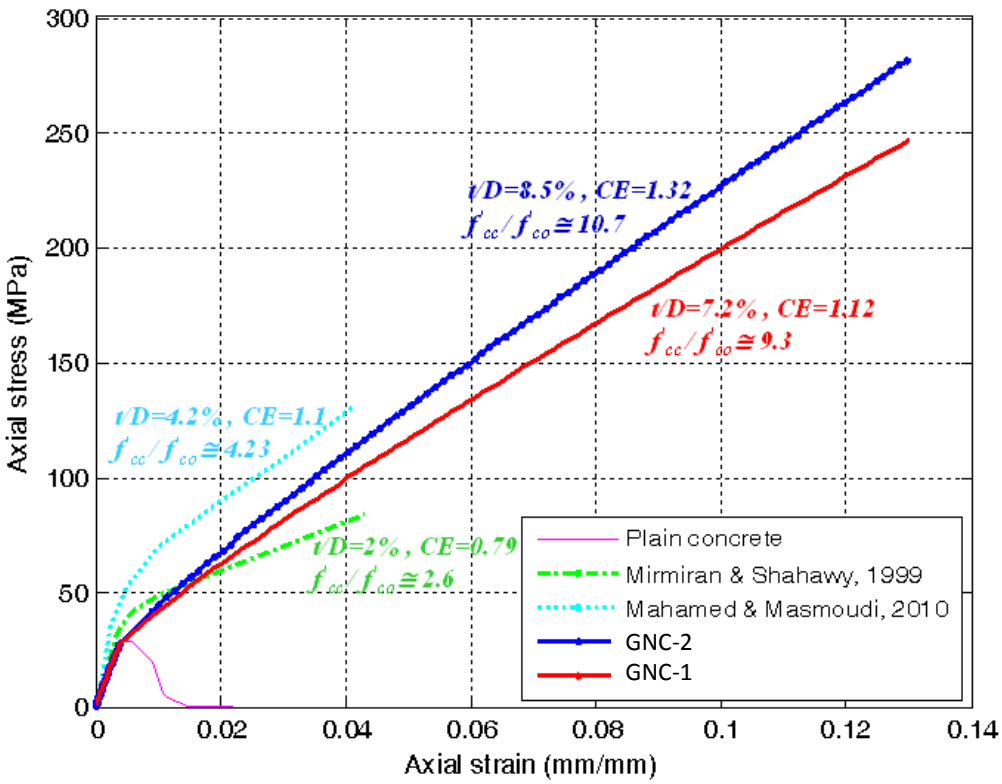

Figure 5- 6. Comparison of stress-strain behavior of GFRP-tube confined concrete with different volumetric ratios under monotonic axial loading

5.6.2.2. Cyclic Loading

The hysteretic behavior of the GNC-2 specimens subjected to two different loading histories are shown in Figure 5- 7 (a) and (b). The degradation of secant stiffness of loading and unloading branches observed from the experimental results is not significant and diminishes as the axial strain increases and the concrete becomes condensed.

It is known that the monotonic stress-strain curve of FRP confined concrete can be used as the backbone curve for describing the hysteretic behavior of specimens under cyclic quasi-static loading (Mirmiran and Shahawy, 1997) which is also observed for the tested specimens.

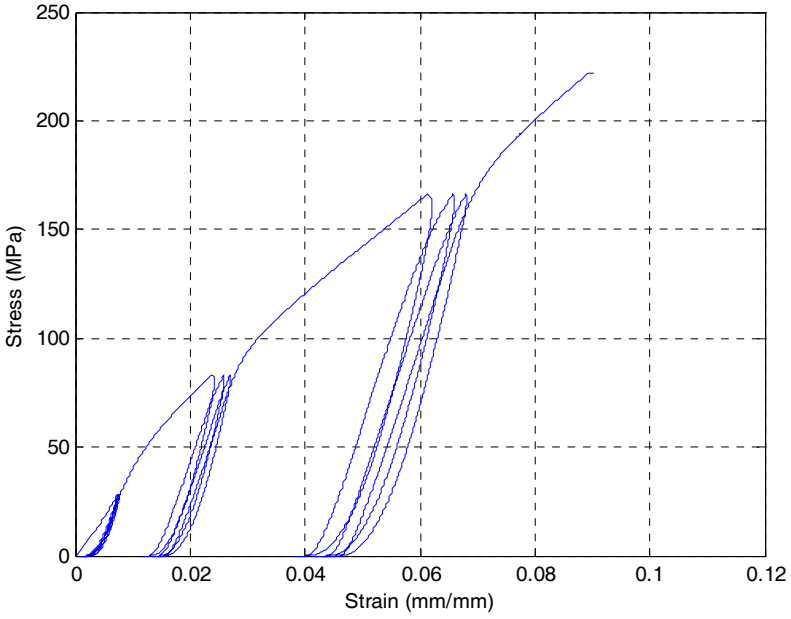

(a)

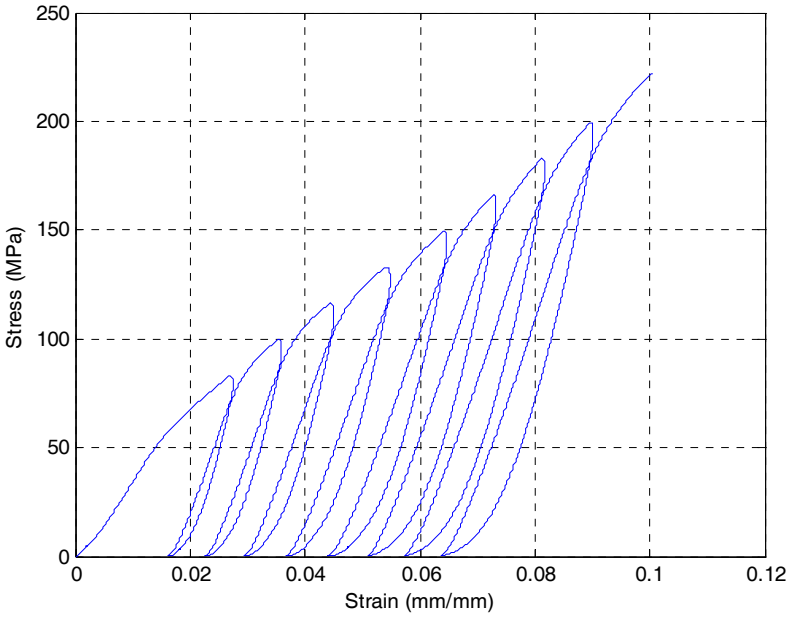

(b)

Figure 5- 7. Cyclic stress-strain curves of GFRP confined concrete cylinders: (a) Load history 1; (b) Load history 2

5.7. Monotonic Analytical Model

5.7.1. Introduction

There are two general types of stress-strain models developed for confined concrete: design-oriented models in which the ultimate compressive strength and axial strain, and the stress-strain behavior is mainly obtained by best-fitting equation with experimental data; and analysis-oriented which generates the stress-strain response more rigorously using an incremental numerical procedure through equilibrium and radial displacement compatibility (Li, 2006; Harajli et al., 2006; Rocca et al. 2008).

Most of the FRP confined concrete models are based on models presented by Richart et al. (1928) or Mander et al. (1988). In Mander's model which is based on multiaxial failure surface of concrete, the confined concrete compressive strength f_{cc} and corresponding strain ε_{cc}, is calculated as a function of lateral confining pressure, f_l:

$$f_{cc} = f'_{co}(-1.254 + 2.254\sqrt{1 + \frac{7.94f_l}{f'_{co}}} - 2\frac{f_l}{f'_{co}}) \tag{5.5}$$

$$\varepsilon_{cc} = \varepsilon_{co}[1 + 5\left(\frac{f_{cc}}{f'_{co}} - 1\right)] \tag{5.6}$$

The General equation proposed by Richart et al. (1928) for confined concrete is defined as:

$$\frac{f_{cc}}{f'_{co}} = 1 + k\left(\frac{f_l}{f'_{co}}\right)^m \tag{5.7}$$

$$\varepsilon_{cc} = \varepsilon_{co}[1 + k\left(\frac{f_{cc}}{f'_{co}} - 1\right)] \tag{5.8}$$

where, *k* and *m* are effectiveness coefficient and power coefficient of the confinement ratio, respectively. In the study performed by Lam and Teng (2002) on a database of 199 test results of FRP-confined concrete, it was shown that the above equation with *k=2* and *m=1* is acceptable for use in the design of concrete-filled FRP tubes if confinement effectiveness ratio is less than one.

The monotonic stress-strain model presented in this study is based on a combined design-oriented and analysis-oriented approach adapted from the Richart's model (Richart et al., 1928).

5.7.2. Ultimate Strain and Stress of GFRP-Tube Confined Concrete

In the experimental tests of this study, no failure was observed for the test specimens by the end of the tests that were terminated because the load capacity of the testing machine was reached; however the ultimate axial strain and stress of tested specimens can be predicted according to the lateral strain of the GFRP tube.

The lateral strain-axial stress of the test specimen can be modeled by a bilinear curve with an initial sharp branch before the tube confinement is completely activated

(Figure 5- 1) and a second linear branch controlled by the elastic behavior of FRP tube. Knowing the rupture strain of the tube, the ultimate axial strain of the specimens can be estimated by extrapolating the lateral strain-axial strain curve. ACI 440.2R-08 proposes the following equation for the maximum confined concrete compressive strength, f_{cc}, in circular columns:

$$f_{cc} = f_{co} + \psi_f 3.3 f_{lu} \tag{5.9}$$

where $\psi_f = 0.95$ is an additional reduction factor and f_{lu} *i*s the maximum confining pressure exerted by FRP tube calculated from Eq. (5.2). This equation follows the general equation of Richart with effectiveness coefficient of 3.3. This equation significantly underestimates the maximum confined concrete compressive strength for the test specimens. In this study, the following equation is proposed to predict the maximum axial stress and strain of tested GFRP-tube confined concrete cylinders from the data fitting of the tested specimen strain-stress results:

$$f'_{cc} = f'_{co}\left(1 + 7\left(\frac{f_{lu}}{f'_{co}}\right)^{0.9}\right) \tag{5.10}$$

$$\varepsilon'_{cc} = \varepsilon_{co}\left[1 + \left(\frac{7}{\rho_f}\right)\left(\frac{f_{lu}}{f'_{co}}\right)\right] \tag{5.11}$$

In the above equations, the value of 0.9 for m, reflects the effect of higher confinement effectiveness ratio and the effect of higher confinement ratio in increasing the ductility is considered through direct implementation of confinement volumetric ratio, ρ_f, in Eq. (5.11).

5.7.3. Compression Monotonic Curve

The stress-strain curve of the test specimens under compression exhibits almost bilinear shape that divides into two zones (see Figure 5- 1): zone I is a linear initial section which follows the unconfined concrete stiffness transiting through a small curvature to zone II, the second linear branch.

The procedure shown in Figure 5- 8 is used to calculate the lateral and axial strain and stress of the test specimens. In FRP-confined concrete elements, axial stress of concrete strongly depends on lateral strain and confinement ratio (Teng et al., 2007a). In the presented model the calculated strains are constantly updated based on the lateral strain-axial strain relationships; in other words, the strength of confined concrete at each load step is a function of current confining pressure. It was observed from the test data that first linear branch ends at the axial stress corresponding to approximately 90% of unconfined strength, when the tube was completely engaged in load carrying through its confinement action. An iterative procedure similar to the approach proposed by Spoelstra and Monti (1999) was used here to predict the strain-stress behavior of the test specimens for zone I. In this procedure for each value of imposed axial strain, ε_c, the axial stress is calculated with the current confining pressure. The lateral strain of concrete that is used to calculate the confining pressure is obtained through an iterative procedure. At each step of imposed axial strain, the value of confining pressure, f_l, in considered equal to its value at previous step with an initial value of zero. The confined stress is calculated using the following equation:

$$f_{cc} = f'_{co}(1 + 2\frac{f_l}{f'_{co}}) \tag{5.12}$$

The current stress is calculated based on the formula proposed by Popovics (1973) and modified in this study for the test specimens as:

$$f_c'(f_{cc}) = \frac{f_{cc}.x.r}{r-1+x^r} \tag{5.13}$$

where,

$$x = \frac{\varepsilon_c}{\varepsilon_{cc}}; \quad \varepsilon_{cc} = \varepsilon_{co}\left[1 + 1.8\frac{f_{cc}}{f_{co}'}\right] \tag{5.14}$$

$$r = \frac{E_{co}}{E_{co}-E_{sec}}, E_{sec} = \frac{f_{cc}}{\varepsilon_{cc}} \tag{5.15}$$

In Eq. (5.14), ε_{co} is the ultimate strain of plain concrete. Also, in Eq. (5.15), E_{co} is the modulus of elasticity of plain concrete. The lateral stress is then calculated through the following constitutive model (Pantazopoulou and Mills, 1995):

$$\varepsilon_l(f_c') = \frac{E_{co}\varepsilon_c - f_c'}{2\beta f_c'} \tag{5.16}$$

In the above equation, β is plain concrete constant which depends on unconfined concrete properties (volume fraction of paste and the water cement ratio) and is calculated from the following equation (Spoelstra and Monti, 1999):

$$\beta = \left|\frac{E_{co}}{f_{co}'} - \frac{1}{\varepsilon_{co}}\right| \tag{5.17}$$

The confining pressure is updated with obtained value of ε_l using the following equation:

$$f_l = \frac{2tE_{FRP}\varepsilon_l}{D} \tag{5.18}$$

This updated value of f_l is then used as the new value for the loop starting at Eq. (5.12), and then the procedure is repeated until convergence of a stable value of f_l. The procedure shows a quick convergence for numerical tests performed to verify the model with experimental results.

Once the value of confined axial stress exceeds $0.9f'_{co}$, Eq. (5.18) is used to calculate the confining pressure, f_l, for each value of the lateral strain. The corresponding confined axial stress and strain are then calculated from Eq. (5.10) and (5.11) replacing f_{lu} with the confining pressure at each step, f_l. The calculation loop terminates at the lateral strain corresponding to the rupture strain of the tube.

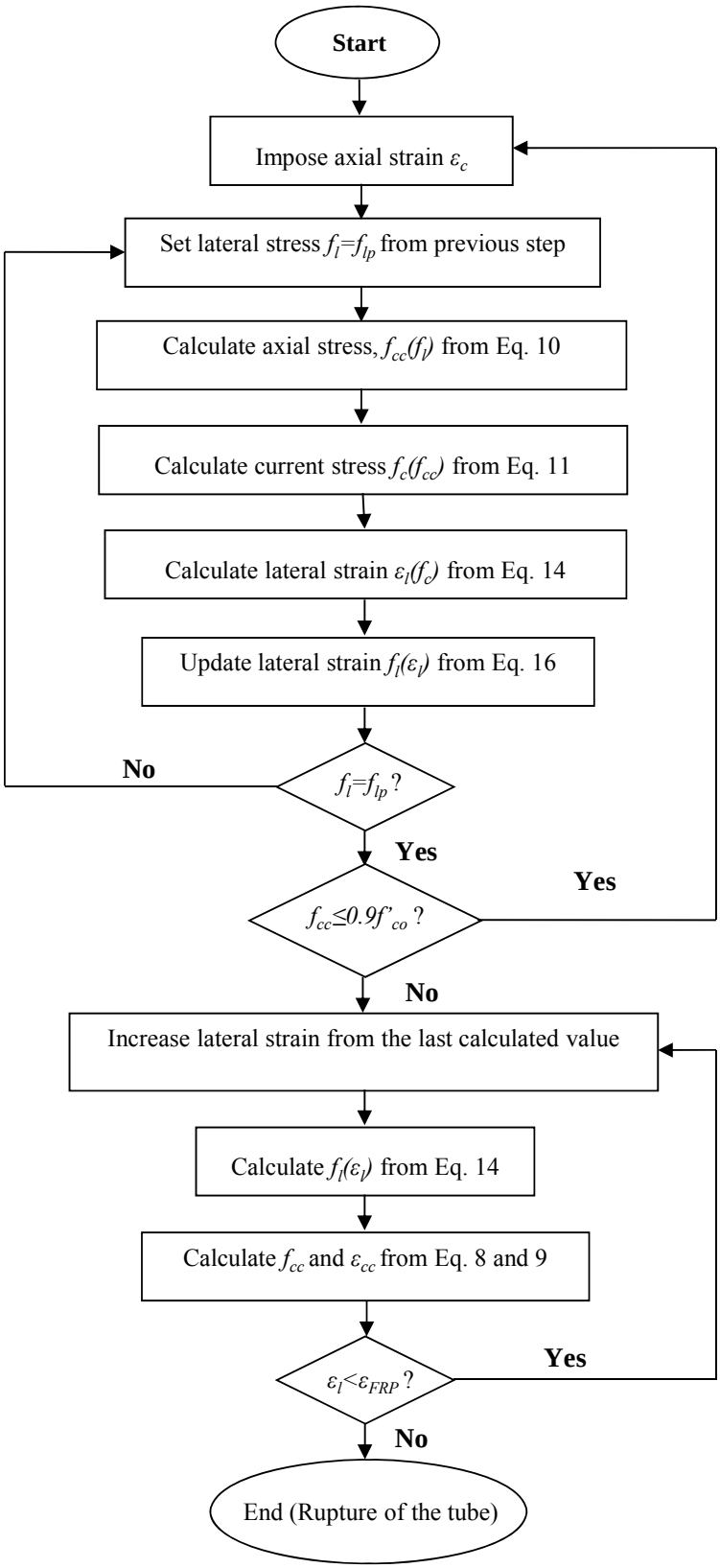

Figure 5- 8. Flowchart of monotonic stress-strain curve calculation

5.8. Hysteretic Model

A comprehensive hysteretic model that is capable of predicting the cyclic behavior of GFRP-tube confined concrete under different loading and unloading scenarios is required to simulate the performance of such axial elements under earthquake loading. The hysteretic stress-strain rules used by Varma et al. (2009) for confined concrete with CFRP sheets that is based on the analytical model of Chang and Mander (1994) is adapted in this study to simulate the behavior of the test specimens under cyclic axial loading. General transition type equations are used to model the curvature of the unloading and reloading branches. In the following sections, the possible loading and unloading histories with the equations used to calculate the hysteretic parameters are described.

5.8.1. Complete Unloading and Reloading

Unloading is termed complete if it occurs from envelope curve to zero stress. Similarly, complete reloading happens when the loading branch targets the envelope curve. The schematic cyclic behavior of the test specimens from this study along with the key parameters to predict the complete unloading and reloading are shown in Figure 5- 9.

As observed from the experimental results, the unloading secant stiffness E_{secun} is always greater than the corresponding reloading secant stiffness. This is due to the fact that in cyclic behavior of confined concrete there is a shift in strain for any cycle

that has the stress value equal to or larger than previous cycle, as can be seen in Figure 5- 7 of experimental results with repetitive cycles. The plastic strain, ε_{res}, defined as the residual strain of concrete when it is unloaded to zero stress (Lam et al. 2006) is one of the key points that is captured through cyclic tests. In the successive series of load cycles, a small change in stiffness of unloading and reloading branches was observed since the GFRP tube reverses the concrete expansion and acts elastically itself.

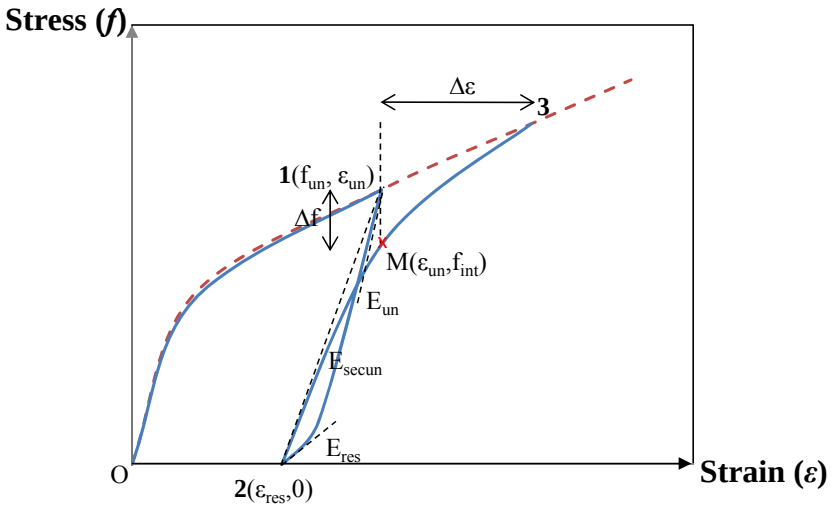

Figure 5- 9. Schematic of hysteretic model for complete unloading and reloading

The unloading and reloading paths are nonlinear curves. Knowing the stress, strain and tangential modulus of elasticity values of unloading and reloading points (i.e. point 1 and 2 in Figure 5- 9), the following general equations are used for transition curves (Varma *et al.*, 2009):

$$f_c(\varepsilon_c) = f_1 + (\varepsilon_c - \varepsilon_1)[E_1 + A|\varepsilon_c - \varepsilon_1|^R] \tag{5.19}$$

where,

$$R = \frac{E_1 - E_{sec}}{E_{sec} - E_2} \tag{5.20}$$

$$A = \frac{E_{sec} - E_1}{|\varepsilon_2 - \varepsilon_1|^R} \tag{5.21}$$

$$E_{sec} = \frac{f_2 - f_1}{\varepsilon_2 - \varepsilon_1} \tag{5.22}$$

The subscripts of 1 and 2 in the above equations point out the values of variables at the beginning and end points on the transition curve.

It is observed from experimental results that the initial reversal slope, E_{un}, at point 1(ε_{un}, f_{un}) equals to $2E_{co}$ (E_{co}: modulus of elasticity of unconfined concrete). It is shown in previous studies that plastic strain for unloading from envelope curve is related to unloading strain (Lam et al., 2006; Varma et al., 2009). At the end of unloading curve, point 2(ε_{res},*0*), the values of residual strain and target slope can be calculated through the following equations (Varma *et al.*, 2009):

$$\varepsilon_{res} = \varepsilon_{un} - \frac{f_{un}}{E_{secun}} \tag{5.23}$$

$$E_{res} = 0.1E_c \exp\left(-0.2\left|\frac{\varepsilon_{un}}{\varepsilon_{co}}\right|\right) \tag{5.24}$$

where,

$$E_{secun} = E_{co}\left(\frac{\varepsilon_{un}}{\varepsilon_{cu}}\right)^{-0.01} \qquad for \quad 0 \le \varepsilon_{cun} \le 0.3\varepsilon_{cu} \qquad \text{(a)}$$

$$E_{secun} = E_{co}\left(\frac{\varepsilon_{un}}{\varepsilon_{cu}}\right)^{-0.12} \qquad for \quad \varepsilon_{cun} > 0.3\varepsilon_{cu} \qquad \text{(b)} \tag{5.25}$$

Having the value for the above mentioned parameters, Eq. (5.19) is used for the transition curve to connect point 1 and 2 for complete unloading curve.

The complete reloading path can be modeled using two transition curves connected at an intermediate point which has the strain value equal to the immediate unloading strain (point M (ε_{un},f_{int})). The starting slope at point 2 (ε_{res},*0*) equals to E_{co}. The stress drop at point M from the envelope curve, Δf, is related to latest unloading strain (Varma et al. 2009). The following equation is calibrated with the experimental data of the test specimens under cyclic loading to obtain the stress at point M:

$$f_{int} = f_{un} - \Delta f_c \tag{5.26}$$

$$\Delta f = 0.08 f_{un}\left(\left|\frac{\varepsilon_{un}}{\varepsilon_{cu}}\right|\right)^{0.15} \tag{5.27}$$

A linear relationship between the shift in strain from point M to end of complete reloading curve that is used by Varma et al. (2009) is also observed for the test specimens. Therefore the slope at point M and $\Delta\varepsilon_c$ are calculated from the following equations (Varma *et al.*, 2009):

$$E_{cnew} = \frac{f_{int}}{\varepsilon_{un} - \varepsilon_{res}} \tag{5.28}$$

$$\Delta\varepsilon = 0.19\varepsilon_{un} \tag{5.29}$$

The value of strain at point 3(ε_{re}, f_{re}) is obtained by adding $\Delta\varepsilon$ to the unloading strain and the stress and target slope at that point is known from the envelope curve (Varma *et al.*, 2009):

$$\varepsilon_{re} = \varepsilon_{cun} + \Delta\varepsilon_c \tag{5.30}$$

$$E_{re} = E_c(\varepsilon_{re}); \quad f_{re} = f_c(\varepsilon_{re}) \tag{5.31}$$

Points 2, M and 3 are then connected with the two transition curves using Eq. (5.19).

5.8.2. Partial Unloading with Complete or Partial Reloading

Partial unloading is referred to the unloading path that ends at a stress level larger than zero. Partial reloading occurs when unloading happens before the loading path reaches the envelope curve. In the equations presented in this section, the variables for partial unloading or reloading points are shown with a star superscript. Figure 5- 10 shows a partial unloading followed by a complete reloading (1-2-3) and a partial reloading (3-4-5). Similar to complete unloading, points 1(ε_{un}, f_{un}) and 2(ε_{oun}, f_{pun}) (also 3 and 4) are connected with a transition curve. To predict the complete or partial reloading path after partial unloading, an intermediate point M' should be

located as a connecting point for two transition curves. Point $M'(\varepsilon_{un}, f^*_{int})$ is located at the vertical offset drawn from unloading point 1 or 3 and its stress and slope are calculated from a linear interpolation as follows (Varma *et al.*, 2009):

$$f^*_{int} = f_{un} - \Delta f \frac{\varepsilon_{un} - \varepsilon_{pun}}{\varepsilon_{un} - \varepsilon_{res}} \tag{5.32}$$

$$E^*_{int} = \frac{f^*_{int} - f_{pun}}{\varepsilon_{un} - \varepsilon_{pun}} \tag{5.33}$$

In the above equation, ε_{res} and Δf are calculated from Eq. (5.23) and (5.27), respectively. If a partial reloading occurs after a partial unloading $(3 - 4 - M' - 5)$, the strain shift calculated from Eq. (5.29) is used to calculate the strain at point $5(\varepsilon^*_{re}, f^*_{re})$ from following interpolation (Varma *et al.*, 2009):

$$\varepsilon^*_{re} = \varepsilon_{un} + \Delta\varepsilon \frac{\varepsilon_{un} - \varepsilon_{pun}}{\varepsilon_{un} - \varepsilon_{res}} \tag{5.34}$$

The target slope at point 5 is calculated by assuming that this point is located on a complete reloading curve ending on backbone curve.

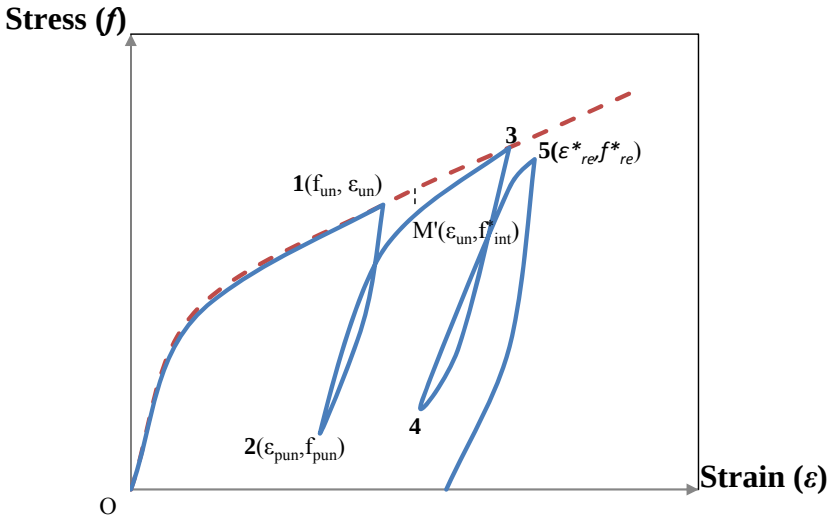

Figure 5- 10. Schematic of hysteretic model for partial unloading

5.8.3. Unloading After a Partial Reloading

The plastic strain (ε_{res}) and its corresponding plastic modulus (E_{res}) are dependent only on the unloading strain of the envelope curve. So, in the case of partial reloading as shown in Figure 5- 11, the unloading strain of point 3(ε^*_{un},f^*_{un}) cannot be used to calculate ε_{res} and E_{res}. Instead, a new unloading strain, ε'_{un}, is defined on the envelope curve on an imaginary point X, through a linear interpolation between unloading strains of point 1 and point 4. Considering the path 1-2-3-4 in Figure 5- 11, ε'_{un} is defined by:

$$\varepsilon_{un} = \varepsilon_{un,1} + \left(\frac{\varepsilon^*_{un,3} - \varepsilon_{un,1}}{\varepsilon_{re,4} - \varepsilon_{res,2}}\right)(\varepsilon_{re,4} - \varepsilon_{un,1}) \qquad (5.35)$$

The value of ε'_{un} is used as unloading strain for further calculation after the unloading branch, 3-4, initiated.

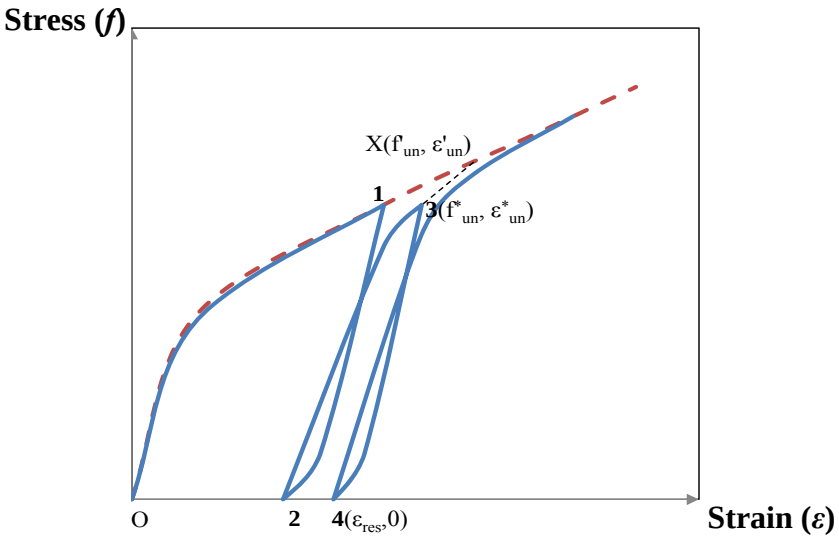

Figure 5- 11. Schematic of hysteretic model for partial reloading

5.9. Implementation of an Analytical Tool into Finite Element Simulation Platform

The numerical simulation of complex structures with similar GFRP-tube confined concrete elements under static and seismic loading demands an accurate analytical tool. OpenSees is an open source finite element analysis framework that accepts contributions from researchers to add new classes to the source code (Mosalam et al., 2007). It is possible to add new materials and elements into OpenSees through definition of new classes and hence it is a suitable platform to incorporate the constitutive model developed for the test specimens.

5.9.1. New GFRP-Tube Confined Concrete Material In OpenSees

The OpenSees interpreter is an object-oriented application that is linked with static libraries which contain all the necessary code for executing the program (McKenna, 2009). It is possible to use dynamic libraries to add new materials, new elements and new commands into the interpreter of OpenSees. This means that when interpreter encounters an unknown material, element or command in the OpenSees code that does not exist in the static libraries, it will look for a dynamic library that has the same name as the unknown material, element or command to load it. This dynamic library should be placed at the same directory that the OpenSees code in

located. The dynamic libraries for new material and elements can be created by a C++ class or a C or Fortran procedure.

Objects in object-oriented programming, consist of state (data) and related behavior (operations). OpenSees as an object-oriented program is comprised of independent modules which communicate and exchange information and commands across each other. A module can be implemented through a class in C++. The most important module in OpneSees is the "Domain", which maintains the information of the model throughout the analysis (Talaat and Mosalam, 2008). Domain has different classes such as "Node", "Element" and "Material" to create a model.

In OpenSees, materials are objects that determine the stress-strain relationship at a point in the element. There are three types of materials in OpenSees named "Uniaxial", "nD" and "Section ForceDeformation" materials. The Uniaxial material provides one-dimensional stress-strain relationship which is used in this study to introduce the new material into OpenSees.

An uniaxial material object termed "GFTCC" which stands for GFRP-tube confined concrete was developed to determine the stress-strain relationship in the elements with GFRP-tube confined concrete material. For this purpose a dynamic library named GFTCC was developed through a C++ class. Figure 5- 12 shows a partial class map of the Domain module under which the new material GFTCC is implemented. The model presented in Sections 5.7 and 5.8 is used in this class to model the monotonic and hysteretic stress-strain behavior. The input parameters for this implemented material include concrete properties ($f'_{co}, \varepsilon_{co}, E_{co}$), FRP tube properties ($f_{FRP}, \varepsilon_{FRP}$) and confinement ratio (t, D).

The advantage of such material implementation is the ease of applying different equations for envelope as well as modifications to hysteretic stress-strain model appropriate for desired confinement in the C++ class to generate a new dynamic library.

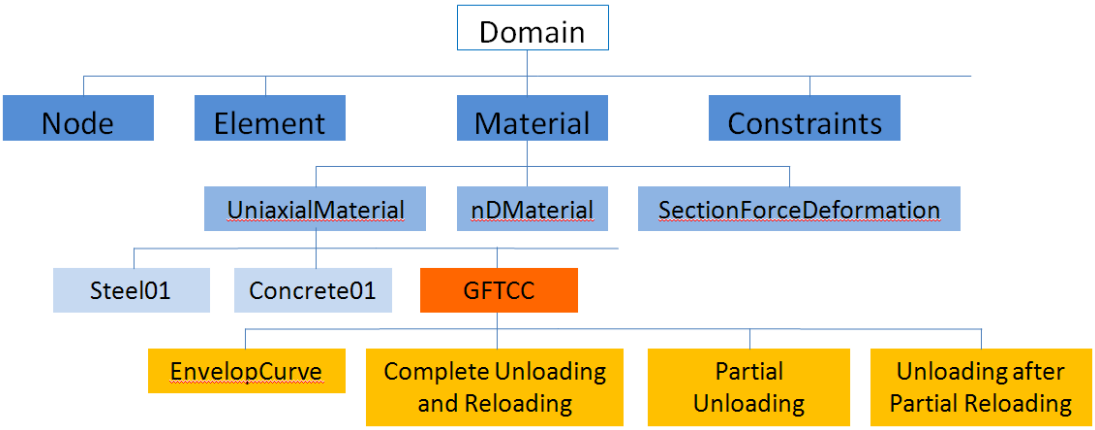

Figure 5- 12. New implemented material (GFTCC) as a class of Domain module

5.9.2. Verification of the New Implemented Material

To verify the accuracy of this implemented analytical tool, experimental stress-strain cycles of the test specimens under compression were simulated in OpenSees. A single compression truss element was used to model the specimen and the GFTCC material is assigned to it.

The loading history for the test specimens in this study were applied to this element and cyclic analysis was performed. Figure 5- 13 (a) and (b) show the results of OpenSees analysis compared with the experimental data. The analysis results show that the implemented material accurately simulated the experimental results corresponding to both cyclic loading histories.

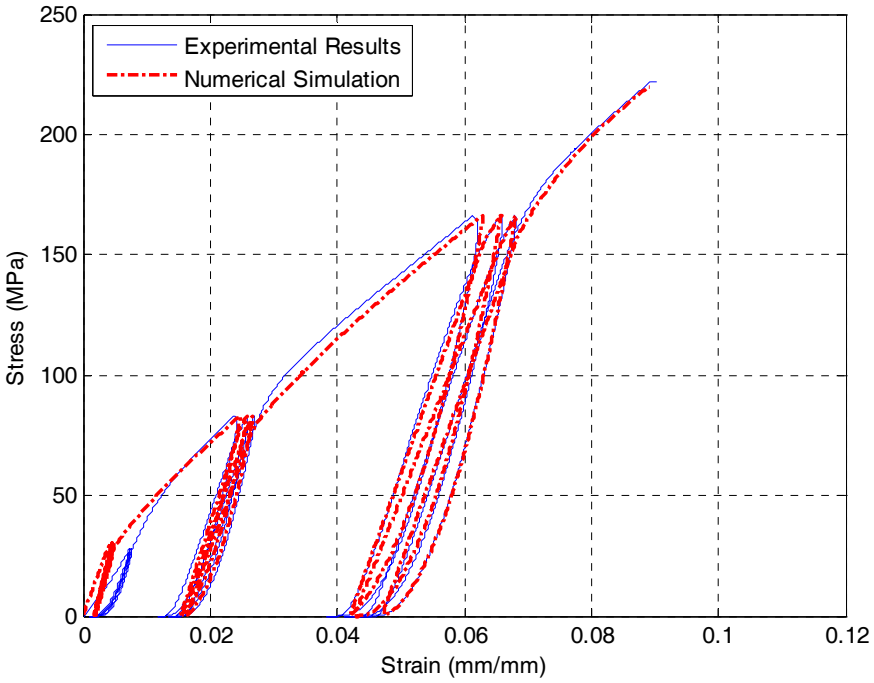

(a)

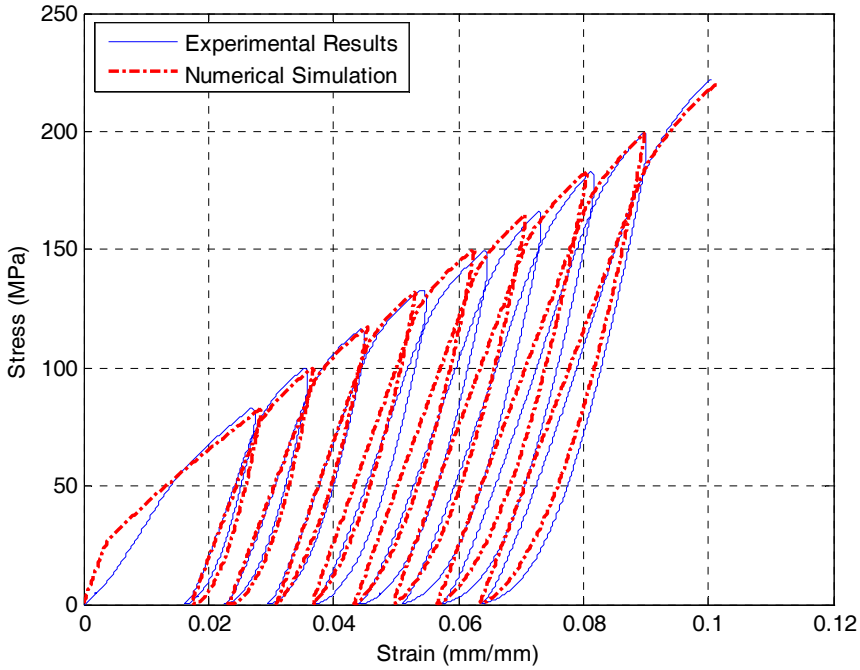

(b)

Figure 5- 13. Numerical simulation of stress-strain curves of GFRP tube confined concrete cylinders: (a) Load history 1; (b) Load history 2

5.10. Summary and Conclusions

This chapter presented the experimental results and analytical modeling of concrete encased in GFRP tube with higher confinement volumetric ratio than those previously reported. The experimental results show a significant increase in strength and ductility of GFRP-tube confined concrete compared to data obtained for lower confinement volumetric ratio. No failure was observed up to the axial load eight times larger than plain concrete ultimate load capacity. The existing strength model for confinement of concrete with thin FRP tubes are not suitable for describing the behavior of GFRP-tube confined concrete with this type of confinement and hence a modified constitutive model is presented in this paper which more accurately predicts the stress-strain behavior of GFRP-tube confined concrete. Specifically, the following conclusions can be drawn from this study:

- The increase in strength and ductility of concrete by confining it with GFRP tube is magnified by increasing the confinement ratio. The tested normal-weight concrete confined with GFRP-tube show the axial load carrying capacity and ductility of 8 and 27 times higher than the plain concrete (up to the load capacity of the 400-kips SATEC testing machine) without any visible failure.
- The primary failure mode in FRP-confined concrete axial elements due to hoop tensile rupture of fibers can be considerably postponed by increasing the confinement ratio.
- The ductility of lightweight concrete increases substantially by encasing it into GFRP tube, however it was observed that the increase in load carrying

capacity would be limited if the concrete strength is too low (f'_{co}=9.5 MPa for the lightweight concrete used in this study). This is believed to be associated with the porous structure of lightweight concrete.

- A constitutive model capable of describing the stress-strain behavior of GFRP-tube confined concrete with high confinement ratio is adapted from existing FRP confined concrete material and calibrated with the test data.
- The promising performance and durability of hybrid element similar to the test specimen configuration make it a suitable form for axial load carrying elements (e.g., braces) in seismic resistant structures. Proper analytical tool which can faithfully simulate the nonlinear behavior of this kind of elements within complex structural systems is desired for performance based engineering. Therefore a uniaxial material model replicating the proposed constitutive laws for GFRP-tube confined concrete was implemented into a general purpose finite element analysis program - OpenSees, and its validity is confirmed using experimental data from this study.

CHAPTER 6 : COMPOSITE CHEVRON WITH SELF-CENTERING BEHAVIOR

6.1. Introduction

The objective of this research is to enhance the ductility and energy dissipation capacity of the diagrid structural system for improved seismic performance. The diagonals at the base module of the diagrid structure carry the maximum axial forces. Instead of regular steel sections, ductile axial load carrying diagonals can be designed to provide required high ductility and energy dissipation capacity. As it was described in Chapter 5, GFRP-tube confined concrete is suitable for use in such axial load carrying elements in seismic resistant structures due to its increased strength and ductility. A new type of composite brace is proposed in this chapter which takes advantage of the confinement action of GFRP tubes to meet the demand for such ductile axial load carrying capacity.

The proposed composite brace is comprised of GFRP-tube confined concrete, inner steel core and high strength post-tensioned tendons. In the following sections of this chapter, the configuration of the composite brace is first described and followed by demonstration of the mechanics and hysteresis behavior of a chevron composed of two inclined composite braces. Then a parametric study on the factors potentially affecting the hysteretic behavior of the composite chevron is conducted and the results are discussed to identify the most important factors that influence the energy dissipation capacity, strength and stiffness of the composite chevron assembly.

6.2. Composite Brace

The schematic of the proposed composite brace is shown in Figure 6- 1 (b). The composite brace is comprised of four components: External GFRP tube, concrete confined with the GFRP tube, an inner steel core and high strength post-tensioned tendons. The steel core is engaged under compression up to a certain axial deformation determined from the analysis of structure under design basis earthquake level. Under larger axial tensile deformations imposed on the element (e.g. under MCE) the steel core will be engaged to carry the tension load together with the PT tendons to ensure the integrity of the building. This can be achieved through a hook mechanism installed on the steel core in construction. In this study the building is analyzed under design basis earthquake and therefore the steel core only carries the compressive load. Therefore the confined concrete together with the steel core carry the compression load imposed on the brace while the PT tendons carry the tensile load. The PT tendons are designed to remain elastic to ensure the tensile load carrying capability of the brace.

There are several alternatives as energy dissipating devices such as friction or viscous dampers, yielding steel bars or shape memory alloys elements. In this study, the steel core and GFRP-tube confined concrete as two parallel compression load carrying elements of the composite brace provide energy dissipation capacity in their post-elastic force-deformation phase under large axial forces.

Slenderness can result in underutilization of confinement in FRP-confined concrete elements (Mirmiran et al., 2001). It was shown that confinement action is not affected by slenderness in compression elements if slenderness ratio was smaller

than 11. Therefore the diameter of the composite brace should be chosen large enough to ensure that no significant reduction in strength or ductility of the FRP-tube confined concrete due to slenderness will happen.

In the following section, the behavior of a chevron composite brace assembly made up of two inclined composite braces is examined for its load-displacement behavior under lateral loading. An analysis model of the chevron assembly is created in OpenSees to investigate its hysteretic behavior under lateral loading.

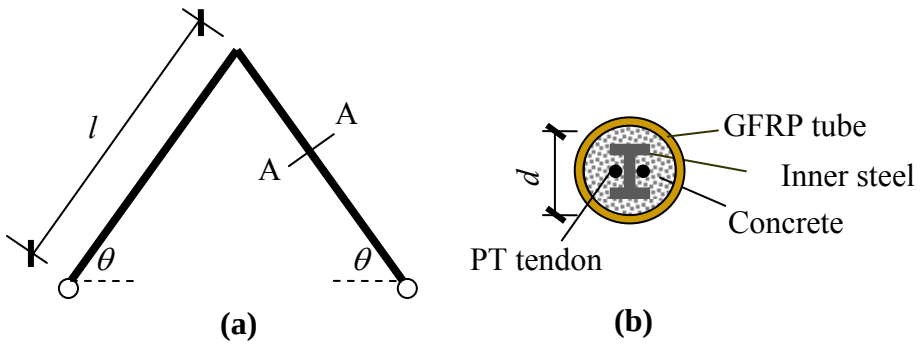

Figure 6- 1. Schematics of the composite brace and subassembly: (a) Geometry; (b) Section A-A

6.3. Self-Centering Chevron Assembly

6.3.1. Configuration

In this section, the behavior of a chevron assembly consisting of two inclined composite braces (Figure 6- 1 (a)) under lateral loading is investigated. The inner diameter *D,* and thickness *t,* of GFRP tube, concrete strength, steel core area, and PT tendons area, strength and ultimate elongation capacity control the strength, post-elastic stiffness, deformation capacity and self-centering capacity of the chevron. The post-tensioning force of tendons contributes to self-centering capability of the chevron.

6.3.2. Composite Chevron

The proposed composite chevron is intended to be used as the base diagonals of diagrid building in Chapter 7. The chevron studied in this section simulates the two adjacent base diagonals of one bay of the prototype building that is analyzed in Chapter 7. Therefore the dimensions of the chevron is designed to be appropriate for this purpose. The analysis parameters for the composite brace subassembly shown in Figure 6- 1 are assumed as follows: θ=72°, l= 3.84 m (151.4") and D=0.965 m (38"). The area of the steel core is selected as 5.5% of the internal area of the GFRP tube; A_s=0.055A_{Tot}=403 cm^2 (62.4 in^2). The total area of the PT tendons is selected as 1.2% of the internal area of the GFRP tube; A_{PT}=0.012A_{Tot}=87.7 cm^2 (13.6 in^2). The PT tendons are Grade 270 strand with modulus of elasticity E_{PT}, the elastic strain and stress $\varepsilon_{PT,E}$ and $f_{PT,E}$, and the ultimate strain $\varepsilon_{PT,u}$ equal to 200 GPa, 0.0084, 1690 MPa

and 0.03, respectively. The tendons are post-tensioned to 10% of their ultimate strength to contribute to re-centering behavior of the chevron along with the gravity load.

Plain concrete cylinder strength is set to be 27.5 MPa (4 ksi) and yielding strength of the steel core is taken as 345 MPa (50 ksi). The GFRP tube considered for the braces is the same material that was used in the experimental study of Chapter 5. As it was mentioned before, the tube is machine-made produced by filament winding high strength continuous glass fiber filaments saturated with corrosion resistant epoxy resin. This type of GFRP-tube products used extensively in oil and gas piping, are available in different diameters and are cost-effective options as confining devices with several advantages such as lightweight and corrosion resistance as mentioned in Chapter 5. The tensile hoop strength and rupture strain of GFRP tubes due to internal pressure are 216 MPa (31.3 ksi) and 0.02 respectively. As it was described before, the confinement effectiveness, which is defined as the ratio of lateral pressure exerted by FRP tube to plain concrete strength ($f_{lu}/f_{co}^{'}$), is a measure of confinement impact in increasing the strength of the concrete. In the experimental study of Chapter 5, the axial load carrying capacity and ductility of normal concrete confined with GFRP-tube with thickness to inner diameter ratio of 0.085, were increased by 8 and 27 times, respectively. It was also found that the primary failure mode in FRP-confined concrete axial elements due to hoop tensile rupture of fibers can be considerably postponed by increasing FRP volumetric confinement ratio, ρ_f (Eq. (5.4)). The high confinement provided for concrete with GFRP tube, prevents undesirable brittle failure of concrete due to high compression load. This is critical for main axial load

carrying elements (e.g. diagonals in diagrid structure) to ensure the reliability of the element. Therefore, the thickness of the GFRP tubes in this study is chosen to be 7% of its inner diameter to obtain a high volumetric confinement ratio and the confinement effectiveness ratio greater than one.

6.4. Numerical Model

The finite element model of composite chevron was modeled in OpenSees to study its hysteretic behavior under lateral loading.

The Steel02 material in OpenSees uses the Giuffre-Menegotto-Pinto model (Menegotto and Pinto, 1973) and is capable of initiating a pre-stress force in the material. This feature is required to model the post-tensioned tendon element. A new tension-only steel material termed "Steel02TO" (Steel02 tension-only) was implemented into OpenSees which uses the same hysteresis rules of Steel02 material but has no compressive strength. This new material with yield strength of 1690 MPa (245 ksi) was used to model the material of the PT tendons.

Since the steel core is supposed to be engaged only under compression under design base earthquake level and lower seismic loads, a new compression only steel material termed "Steel01CO" (Steel01 Compression-only) was implemented into OpenSees. This material uses the same hysteresis rules of the bilinear steel model of Steel01 material in OpenSees (OpenSees, 2009). This new material with 2% strain hardening and yield strength of 345 MPa (50 ksi) was used for the steel core elements.

The GFRP-tube confined concrete model developed and implemented into OpenSees in Chapter 5 was used to model the confined concrete of the composite brace.

Each of three components of two braces of the chevron, are modeled with nonlinear truss elements acting in parallel. The total force in each brace is the sum of the forces in the GFRP-tube confined concrete, steel core and PT tendons.

The chevron presented here is intended to be used as the base diagonals of the diagrid building in the next Chapter. The prototype diagrid building analyzed in Chapter 7, is a 3x3 bay, 21-story diagrid building (similar to the prototype diagrid building in Chapter 2). Therefore, three chevrons will form the first module of the diagrid building covering three bays. Gravity loading is crucial for re-centering behavior of a rocking structure (e.g. the hybrid diagrid frame presented in Chapter 7). Thus, a gravity load equal to one third of the tributary gravity load of 18 stories of the aforementioned diagrid building was applied to the top node of the chevron.

6.5. Hysteretic Behavior of Composite Chevron

Two cycles of displacement controlled horizontal loading were applied at the top node of the composite brace assembly model in OpenSees with the individual cycle peak values being 37 mm, 74 mm, respectively (corresponding to drift ratios of 1% and 2%, respectively). The computed top horizontal load vs. displacement curve plotted in Figure 6- 2 (a) shows a symmetric self-centering hysteresis for the chevron subassembly.

The force-displacement of each component of the brace is shown in Figure 6- 2 (b). The two inclined components of the composite brace assembly, work synergistically as a chevron to exhibit symmetric horizontal load behavior.

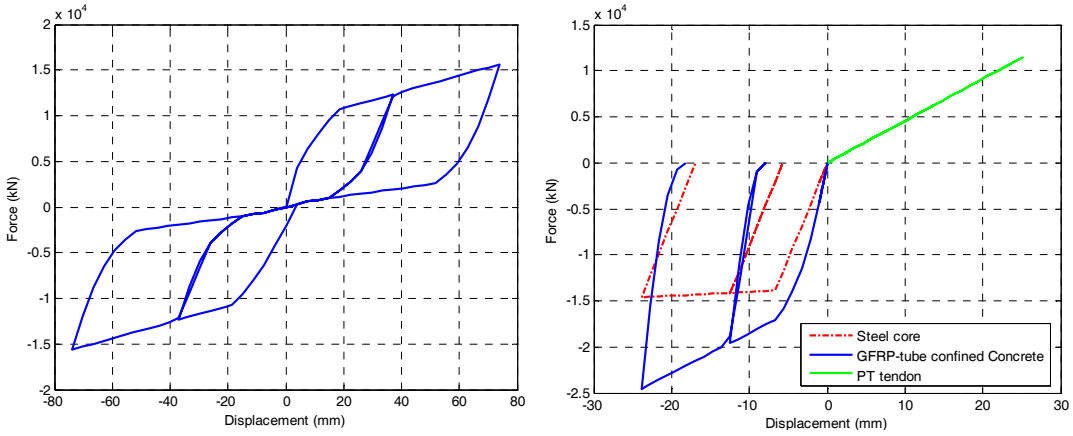

(a) **(b)**

Figure 6- 2. (a)Hysteresis curves of the composite chevron under lateral cyclic loading; (b)Force-displacement curves of brace components;

6.6. Parametric Study of Composite Chevron

A parametric study was carried out to investigate the effect of several parameters on energy dissipation capacity, strength and stiffness of the chevron composite brace subassembly. Four parameters were selected including brace inclined angle (θ), yielding strength of the inner steel core (f_y), and another two parameters defined as:

$$\rho_s = \frac{A_s}{A} \tag{6.1}$$

$$\rho_{PT} = \frac{A_{PT}}{A} \tag{6.2}$$

where ρ_s is the area ratio of steel core to concrete and ρ_{PT} is the area ratio of post-tension tendons to concrete. All other parameter values are kept constant (their values are given in Section 6.3.2) in this parametric study.

The OpenSees model developed in section 6.4 was used to investigate the effect of different parameters on hysteretic behavior of the chevron composite brace subassembly. The same magnitude of gravity load that was applied to the top node of the chevron in section 6.4, was applied to all case studies. One cycle of displacement controlled horizontal loading corresponding to 37 mm horizontal displacement of the top of the chevron (1% drift ratio) was applied to the top node of chevron.

In the following sections of this chapter, the effect of each of considered parameters on hysteretic behavior of the composite chevron brace is presented and the numerical statistics on changes of energy dissipation capacity, strength and stiffness of the brace are discussed.

6.6.1. Effect of Diagonal Inclination Angle (θ)

The following values of the brace inclination angle, θ, were considered for this parametric study: 60^0, 66^0 and 72^0, 78^0. The length of each component is determined in such a way that its vertical projection ($l\sin\theta$) is kept to be a constant value of 3.65 m (12'), about one story height of a regular building. The hysteresis curves (horizontal load vs. displacement) of the chevron composite brace subassembly are shown in Figure 6- 3 for each case with different values of θ.

The effect of varying brace slope on energy dissipation capacity, strength and initial stiffness of the composite chevron is shown in Figure 6- 4. It is observed from Figure 6- 4 (a) that the hysteresis energy dissipated by the chevron (E, i.e. the area enclosed by one hysteresis cycle), deceases with the increase in θ values. The strength, f, and the initial stiffness, k_i, of the brace subassembly corresponding to different values of θ are computed and plotted in Figure 6- 4 (b) and (c), respectively. It is seen that with increasing θ values, the strength and the initial elastic stiffness of the chevron decline. With θ increased from 60^0 to 78^0, the energy dissipation, the strength and the initial stiffness of the brace subassembly is reduced by 78%, 66% and 77% respectively.

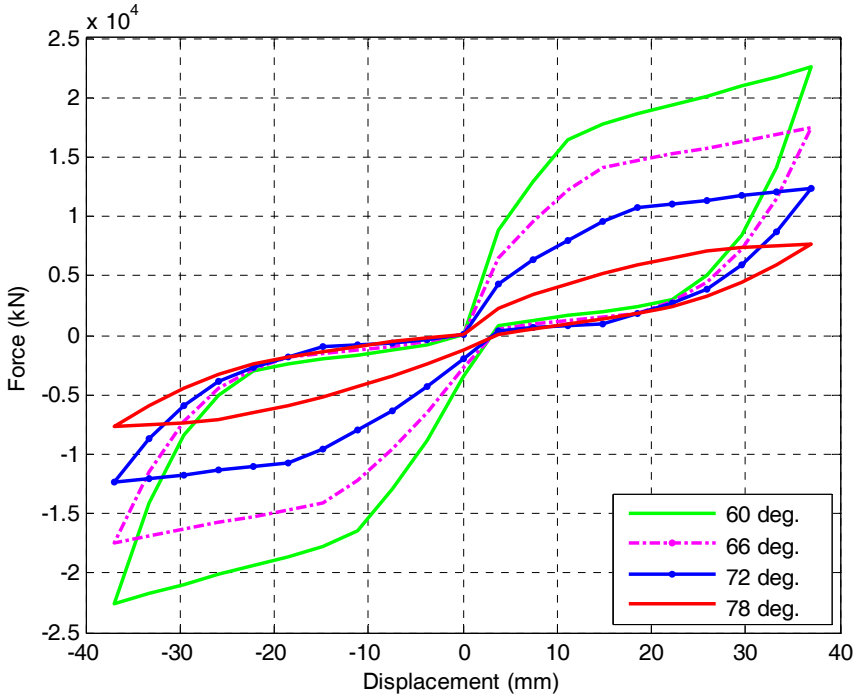

Figure 6- 3. Force-displacement curve of composite chevron for different values of brace angle

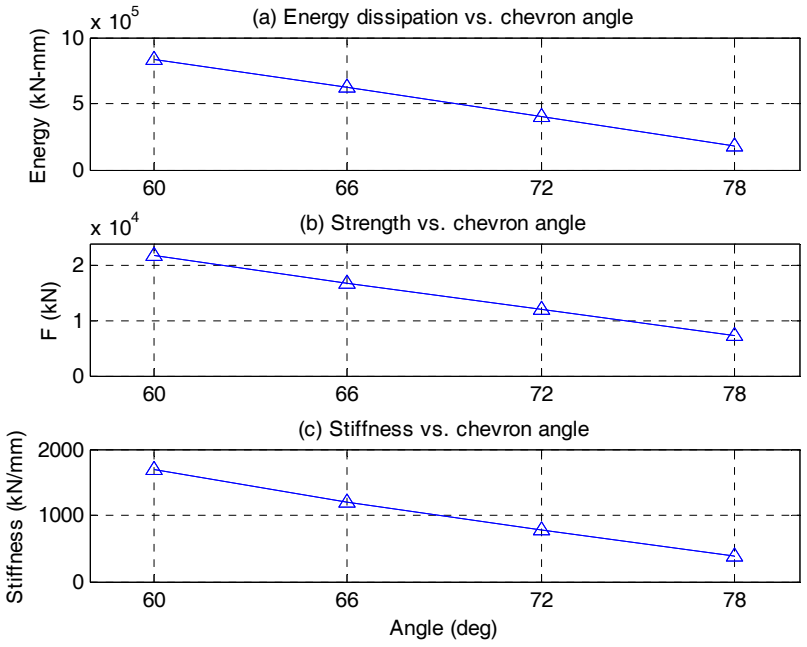

Figure 6- 4. Effect of brace angle on behavior of the composite chevron

6.6.2. Effect of PT Tendon Area

The following values are considered for the ratio of PT tendon area (ρ_{PT}): 0.6%, 1.2%, 1.8%, and 2.4%. The hysteresis curves of the brace subassembly computed for various values of ρ_{PT} are shown in Figure 6- 5.

As seen in Figure 6- 6, the dissipated hysteresis energy and strength of the brace subassembly increases almost linearly with increasing ρ_{PT} values. With ρ_{PT} increased from 0.6% to 2.4%, the energy dissipation and the strength the brace subassembly are increased by 3.65%, 14.4%, respectively, suggesting that increasing steel area had a small effect on increasing the energy dissipation capacity of the chevron brace and a moderate effect on increasing its strength. The initial stiffness of the chevron remained almost the same with increasing the value of ρ_{PT}; however the stiffness of unloading branch of the hysteresis curve of the chevron increases with increasing value of ρ_{PT}, improving the self-centering behavior of the brace subassembly.

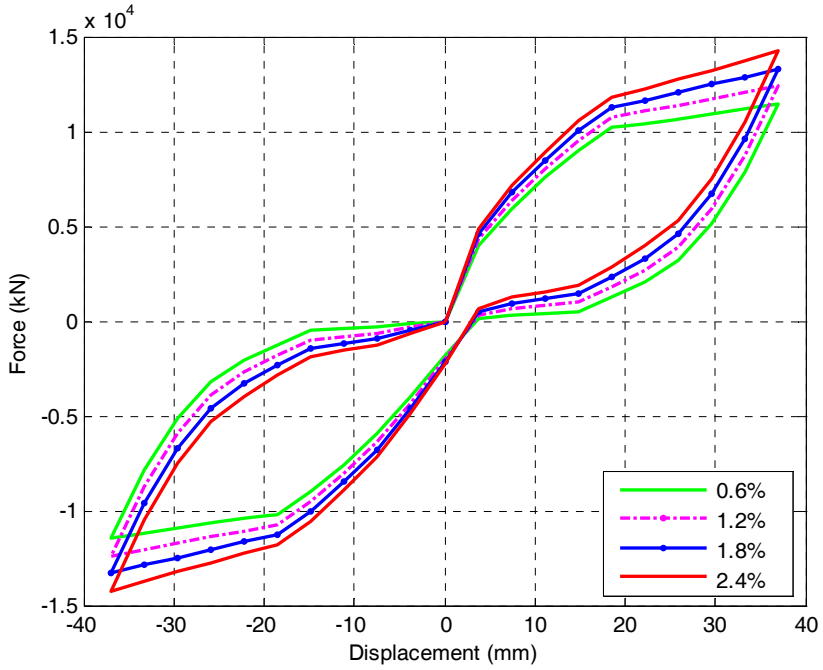

Figure 6- 5. Force-displacement curve of composite chevron for different values of PT tendon area ratio

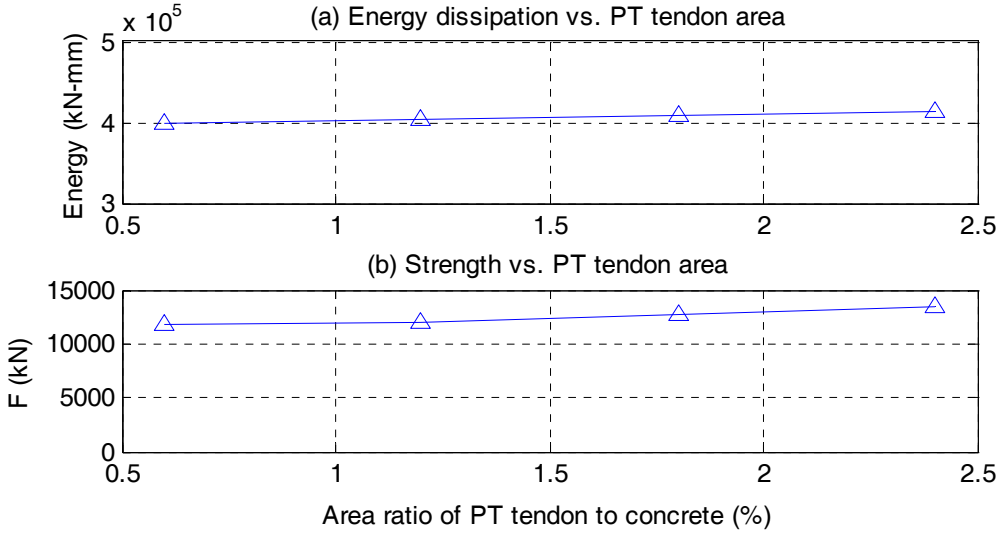

Figure 6- 6. Effect of PT tendon area ratio on the behavior of the composite chevron

6.6.3. Effect of Steel Core Area

The following values are considered for the ratio of steel area (ρ_s): 4.4%, 5.5%, 6.6%, and 7.7%, which correspond to A_s values of 32178, 40222, 48267, and 56311 mm^2, respectively. The hysteresis curves of the brace subassembly computed for various values of ρ_s are shown in Figure 6- 7.

The effect of changed inner steel core area ratio on energy dissipation capacity and strength of the composite chevron is shown in Figure 6- 8 (a) and (b), respectively. The dissipated hysteresis energy and strength of the brace subassembly increases linearly with increasing ρ_s values. With ρ_s increased from 4.4% to 7.7%, the energy dissipation and the strength of the brace subassembly are increased by 18.6%, 21% respectively. The increased value of ρ_s did not have a significant effect on initial stiffness of the composite chevron.

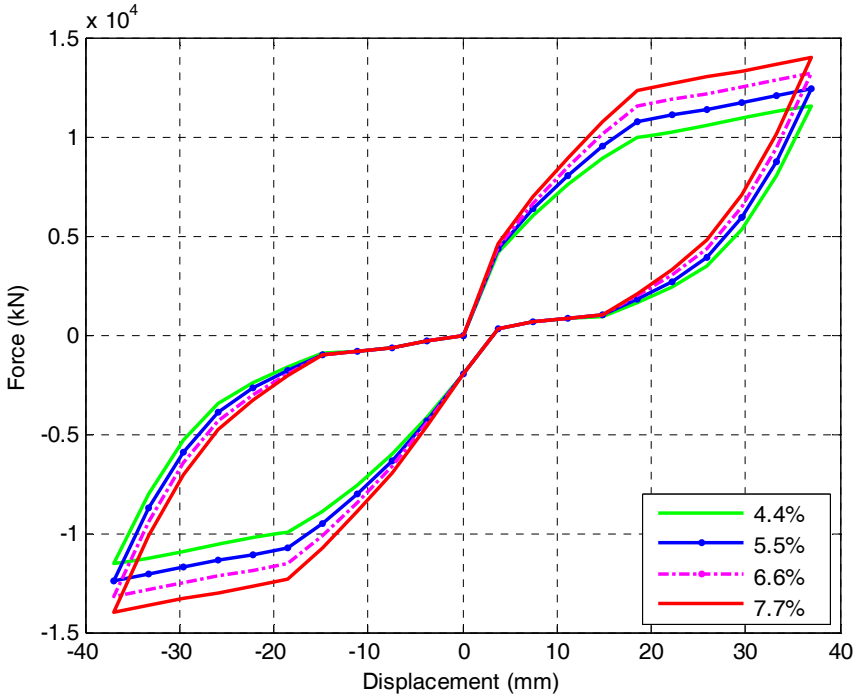

Figure 6- 7. Force-displacement curve of composite chevron for different values of inner steel core area ratio

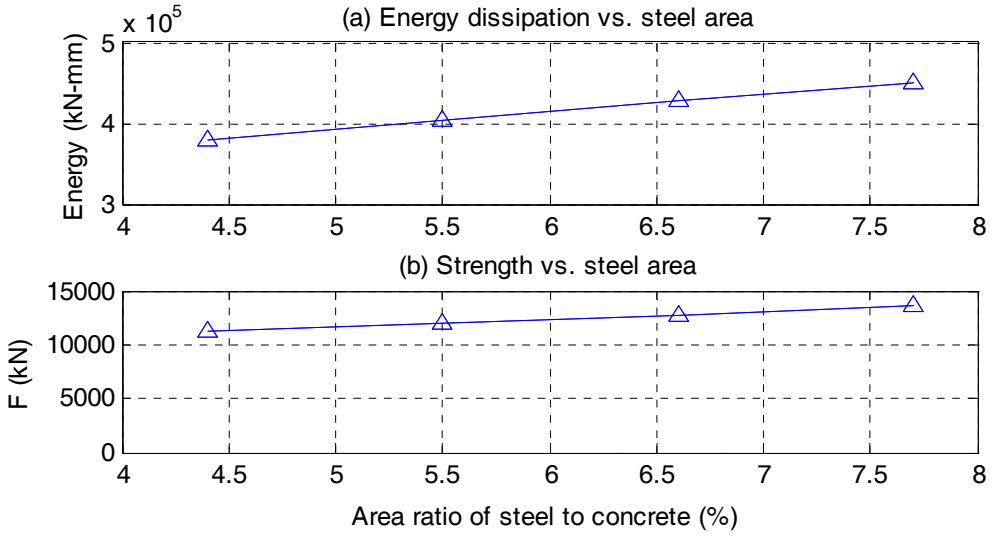

Figure 6- 8. Effect of inner steel core area ratio on the behavior of the composite chevron

6.6.4. Effect of Steel Core Yield Strength (f_y)

The yield stress of the steel core, f_y, includes the following values for the parametric study: 207, 276, 345 and 414 MPa (30, 40, 50 and 60 ksi). The hysteresis curves computed for various values of f_y are shown in Figure 6- 9.

The effect of inner steel core yield strength on hysteretic behavior of composite chevron is shown in Figure 6- 10. It can be seen from Figure 6- 10 (a) that the hysteresis energy dissipated by the brace subassembly increases with increasing f_y value from 207 MPa to 276 MPa, and it remains almost constant for the yield strength of 345 MPa. Afterward it decreases with increasing value of f_y. The strength of the chevron increases for higher values of the yield strength of the steel core showing about 25% increase with f_y increasing from 207 MPa to 414 MPa. The initial stiffness of the brace subassembly remains unchanged for the different values of f_y.

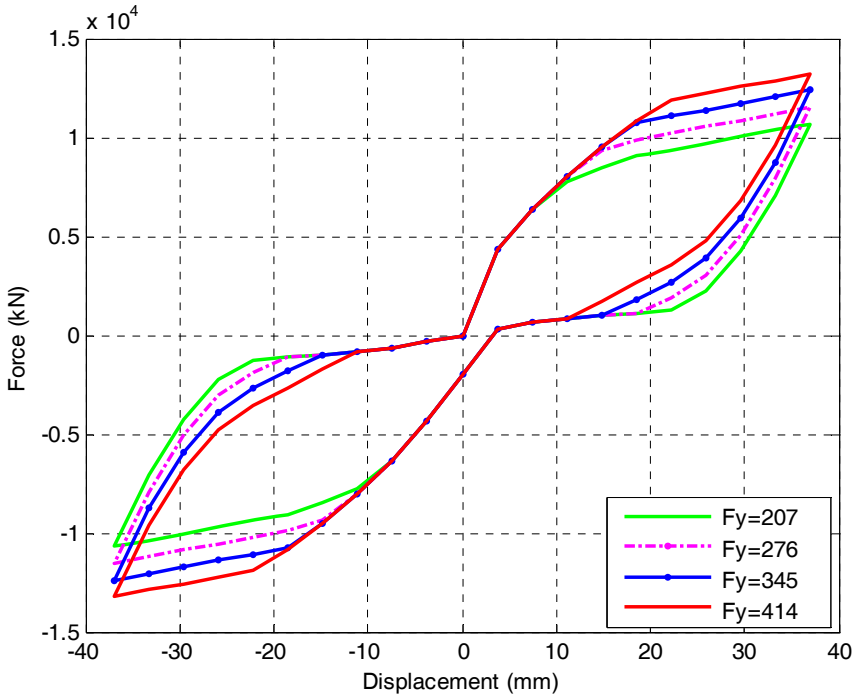

Figure 6- 9. Force-displacement curve of composite chevron for different values of inner steel core yield strength

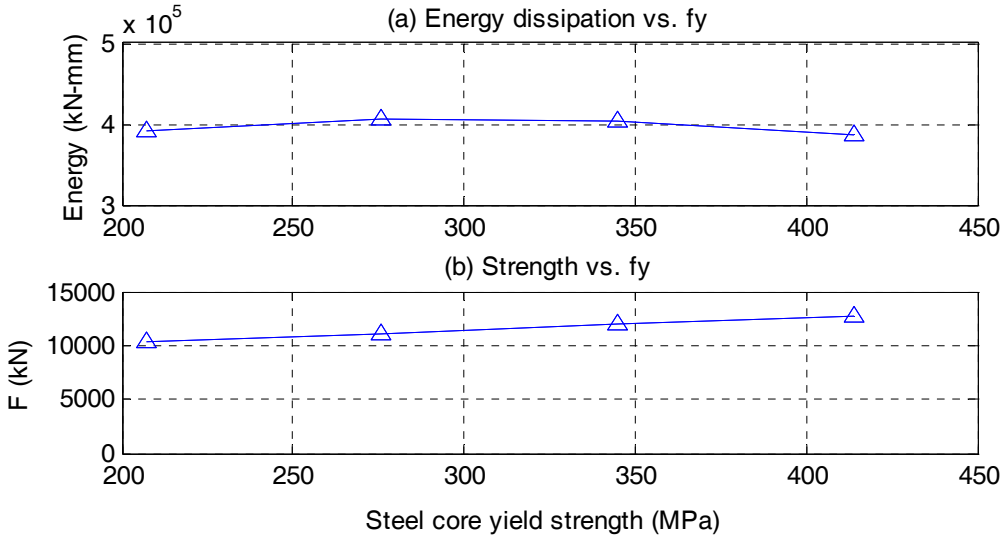

Figure 6- 10. Effect of inner steel core yield strength on the behavior of the composite chevron

6.7. Summary and Conclusions

A new type of GFRP-tube-confined-concrete composite brace is proposed for ductile axial load carrying elements. The brace is composed of GFRP-tube confined concrete, inner steel core and high strength post-tensioned tendons. Such composite bracing features enhanced energy dissipation through steel yielding and GFRP-tube confined concrete hysteresis, as well as large initial stiffness and ductility. The numerical model for the chevron constructed of two inclined composite braces bracing was developed in OpenSees and the mechanical behavior of a chevron composite brace assembly under cyclic lateral loading was studied. The numerical analysis of the chevron shows that two inclined components of the composite brace assembly, work synergistically as a chevron to exhibit symmetric self-entering behavior under lateral loading. The composite chevron exhibits self-centering behavior, high initial stiffness and enhanced ductility and is a desirable alternative for base module of the diagrid structure.

A simulation-based parametric study of the composite chevron was performed and effect of different parameters of the composite brace including inclined angle of each component, post-tensioned tendons area ratio, the inner steel core area ratio and yielding strength on hysteretic behavior of the chevron under lateral loading was investigated. The analysis results reveal that among the considered parameters, the brace angle has the greatest influence on the energy dissipation capacity, strength and initial stiffness of the composite chevron and thus should be given more consideration when designing the composite chevron for lateral load resistance.

The area ratio of post-tensioned tendons has a small effect on energy dissipation capacity and a moderate effect on strength of the chevron assembly under lateral loading. The stiffness of unloading branch of the composite chevron increases with increasing area ratio of tendons and results in sharper flag-shaped hysteresis.

Increasing the area ratio of the steel core increased the energy dissipation capacity and strength of the chevron composite brace subassembly. The steel core with higher yield strength, increased the strength of the chevron moderately but did not affect its stiffness. The energy dissipation capacity of the composite chevron decreased for steel core with yield strength higher than 345 MPa.

CHAPTER 7 : HYBRID DIAGRID FRAMING SYSTEM WITH SELF-CENTERING BEHAVIOR

7.1. Introduction

The limited energy dissipation capacity and ductility of the conventional diagrid structure requires improvements of its seismic performance of this elegant and redundant structural system for use in high seismic regions. The self-centering chevron brace comprised of glass fiber reinforced polymer (GFRP)-tube confined concrete, steel core and post-tensioning tendons presented in Chapter 6, is employed in this chapter to improve the ductility and energy dissipation capacity of the diagrid system. In this part of the research, the concept of hybrid diagrid structural system with re-centering behavior is pursued by using the self-centering chevron as base diagonals. The base chevrons re-center the whole structure post seismic events and retain the rest of the diagrid structure elastic during the earthquake.

In the following sections of this chapter, the concept of self-centering structures as an innovative seismic-force resisting system design is presented first. The nonlinear static and time history analysis of a prototype 21-story hybrid diagrid building are performed and the results are discussed to demonstrate the potential use of such hybrid diagrid structural system in seismic active regions.

7.2. Self-Centering Structures

In conventional structural systems such as moment-resisting frames, shear walls and braced frames, the required displacement capacity of buildings are provided through inelastic ductile response of certain structural elements. Controlling the damage and subsequently the repair cost and improving the serviceability of the building (e.g. decreasing the residual drifts) after design basis earthquakes (DBE) have been the main targets of performance-based earthquake engineering (PBEE). Variety of approaches have been proposed in the past for different structural systems to achieve the PBEE goals.

New trends in seismic design have resulted in proposals of several innovative seismic protection strategies, among which the concept of self-centering system have received a lot of attention recently (e.g., Perez 2004; Restrepo and Rahman 2007; Erkmen and Schultz 2009; Chou and Chen 2010; Hajjar *et al.* 2010). A flag-shaped hysteresis loop is typical of such self-centering systems with energy dissipation capability. Self-centering systems can be achieved by utilizing post-tensioning (Kurama 1999), special energy dissipating devices or special material such as shape memory alloys (Zhu and Zhang 2008). Researchers in the US have studied a family of post-tensioned (PT) systems with self-centering capabilities, including PT concrete wall, PT concrete frame, and steel frame system with PT moment connections. In general, these systems use gap-opening behavior at selected critical joints between main structural members, along with associated energy dissipation elements, to provide nonlinear softening behavior, ductility, and energy dissipation without significant inelastic deformation and related damage to the primary structural

members. Elastic restoring forces provided by PT tendons return the structure to its original position, eliminating residual drift. Self-centering systems thus have the ability to control damage and to reduce (or even eliminate) residual structural deformation, after strong earthquake events.

In moment resisting frames, post-tensioned (PT) beam-column connections have been used by researches (e.g. Ricles et al., 2001; Sause et al., 2010) to minimize residual drifts through gap opening and closing at the beam-column interface resulting in a self-centering behavior.

In damage-tolerant braced frames, structural damages caused by an earthquake are concentrated only on braces as energy-dissipative lateral-load resisting elements (Kim and Seo, 2003). Bracing elements with flag-shaped hysteretic behavior utilizing mechanical or fluid dampers or shape memory alloys have also been used in the past by researches to enhance the seismic performance of braced frames. (e.g. Nims et al. 1993; Dolce et al. 2000; Christopoulos et al. 2008).

Structural systems with controlled rocking behavior also exhibit self-centering ability (e.g., Holden et al. 2003; Ajrab *et al.* 2004; Jeong and Mahin 2007; Pollino and Bruneau 2008; Cheng 2008). Rocking systems created with the idea of allowing the structure to rotate relative to their foundations are very promising self-centering design options for use in high seismic regions. The rocking structures' desirable seismic performance can be explained by free vibration response of a rigid rocking block (Housner, 1963; Ajrab et al. 2004). Post-tensioned rocking systems can be properly designed to show self-centering behavior allowing the structure to return to its original position after earthquake. The rocking columns for a bridge structure

studied by Mander and Cheng (1997) used unbounded concentric tendons anchored to the foundation and deck at both ends which showed a good serviceability under strong ground motions showing no damage under large displacements. In the study conducted by Sakai and Mahin (2003) on re-centering reinforced concrete columns, it was shown that replacing half of the steel rebars with prestressed tendons resulted in a 25% decrease in the residual displacement of the column. Post-tensioned steel was added along height of the concentrically-braced frames by Roke at al. (2008) to achieve self-centering behavior under DBE. Supplemental damping devices have been used by different researchers along with tendons to increase the energy dissipation capacity.

7.3. Hybrid Diarid Framing System with Self-Centering Behavior

The diagrid system has high elastic stiffness which is one of the desirable characteristics of seismic system for drift control under low to moderate earthquakes; however under strong earthquakes the limited ductility and energy dissipation capacity of the conventional diagrid system makes it susceptible to concentrated damage in diagonals that are primary structural elements for gravity load carrying and prone to residual lateral deformations. In order to improve the seismic performance of diagrid structure, a hybrid diagrid framing structural system with re-centering ability through rocking during earthquake is proposed in this chapter. The diagrid system possessing high elastic stiffness is suitable for the rocking system, which ideally should be a rigid block. To improve the limited ductility and energy dissipation capacity of diagrid systems, a new type of self-centering diagrid members comprised of GFRP-tube confined concrete, steel core and post-tensioned tendons that presented in Chapter 6, is implemented in the lower stories of the hybrid diagrid framing systems. Figure 7- 1 (a) and (b) show schematic of the proposed hybrid diagrid framing system. The self-centering diagrid members which form base chevrons with large stiffness, enhanced ductility and energy dissipation capability, enable the rocking behavior for the diagrid system.

The chevron composite bracing described in Chapter 6, exhibits self-centering behavior under lateral loading and has large initial stiffness and high ductility because of the contribution of the confined concrete and post-tensioned tendons. To assess the benefits of such elements as base diagonals in diagrid framing system, a high-rise diagrid building with such self-centering chevrons installed in its base module was

designed and analyzed under lateral static and earthquake loading. The area of the concrete and steel core and post-tensioned tendons control the strength of the base diagonals and it is proportioned according to capacity design goals to prevent the increased base shear which demands larger design forces for the footing.

Similar configuration to what described before is considered for the base diagonals consisting of GFRP-tube confined concrete, steel core and unbonded, post-tensioned steel tendons to mitigate the residual displacement and avoid yielding of rest of steel diagonals. Since in this study the performance of the building is investigated under design basis earthquake, the steel core is being engaged only under compressive load and contributes to the integrity of the diagonals. The confined concrete prevents the steel core from buckling and together they carry the compression load and dissipate energy under large deformations. Another advantage of using GFRP-tubes confined concrete with high volumetric confinement ratio in the base diagonals is shock absorption and steel core protection when the structure is rocking during the earthquake.

Steel tendons have relatively low deformability capacity and should be prevented from yielding through proper design. Unbonding the tendons reduces the imposed strain on the tendons (see e.g. Sakai and Mahin, 2004; Lee and Billington, 2011). To increase the elongation capacity of the tendons, they are anchored to the base at one end and the nodes of the steel diagonals at the top of second module at the other end as shown in Figure 7- 1 (b).

The rest of the hybrid diagrid system above the base module consists of diagonals and beams similar to regular diagrid arrangement and is intended to remain

elastic under DBE. The elastic upper structure and base chevrons collectively form a rocking system. Gravity loads and post-tensioning forces resist diagonals uplift and re-center the structure after uplift.

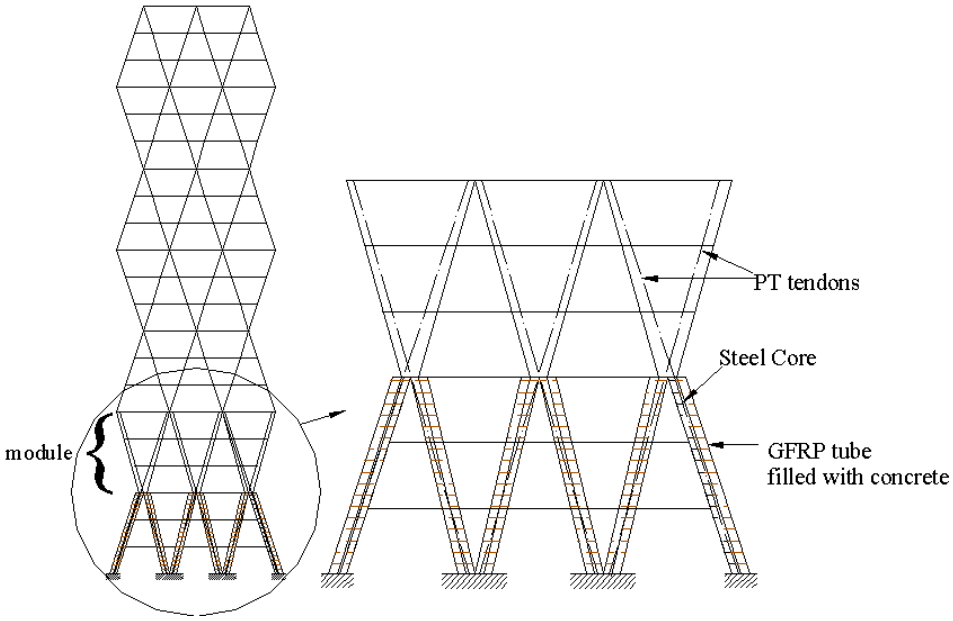

Figure 7- 1. Schematic of hybrid diagrid framing system
(a) Hybrid diagrid frame (b) Close-up view

7.4. Case Study

The 3x3 bay, 21-story diagrid building presented in Chapter 2 was selected as the base design for case study of hybrid diagrid building. The elevation and plan of the prototype hybrid diagrid building studied in this chapter is shown in Figure 7- 2 (a) and (b).

The size of the diagonals and beams at stories above the base chevrons should be designed large enough to create a rigid block above the composite base module and resist the forces induced in the diagonals and ensure that they remain elastic. The area of the structural elements of the prototype 21-story hybrid diagrid building is shown in Table 7- 1.

The same composite chevron studied in Chapter 6 and shown in Figure 7- 2 (c) was used as the base diagonals. The inner diameter of GFRP-tube was 0.965 m (38 inch) filled witrh normal concrete with 27.5 MPa (4 ksi) strength. Similar to the chevron studied in Chapter 6, the area of the steel core is selected as 5.5% of the internal area of the GFRP tube; A_s=0.055A_{Tot}=403 cm^2 (62.4 in^2). The total area of the PT tendons is selected as 1.2% of the internal area of the GFRP tube; A_{PT}=0.012A_{Tot}=87.7 cm^2 (13.6 in^2). The PT tendons are grade 270 strand with modulus of elasticity E_{PT}, the elastic strain and stress $\varepsilon_{PT,E}$ and $f_{PT,E}$, and the ultimate strain $\varepsilon_{PT,u}$ equal to 200 GPa, 0.0084, 1690 MPa and 0.03, respectively.

Three such composite braces form the six base diagonal elements. The post-tensioning force of 1,500 kN (340 kips) was about 10% of the ultimate strength of the grade 270 steel strands for the post-tensioned tendons.

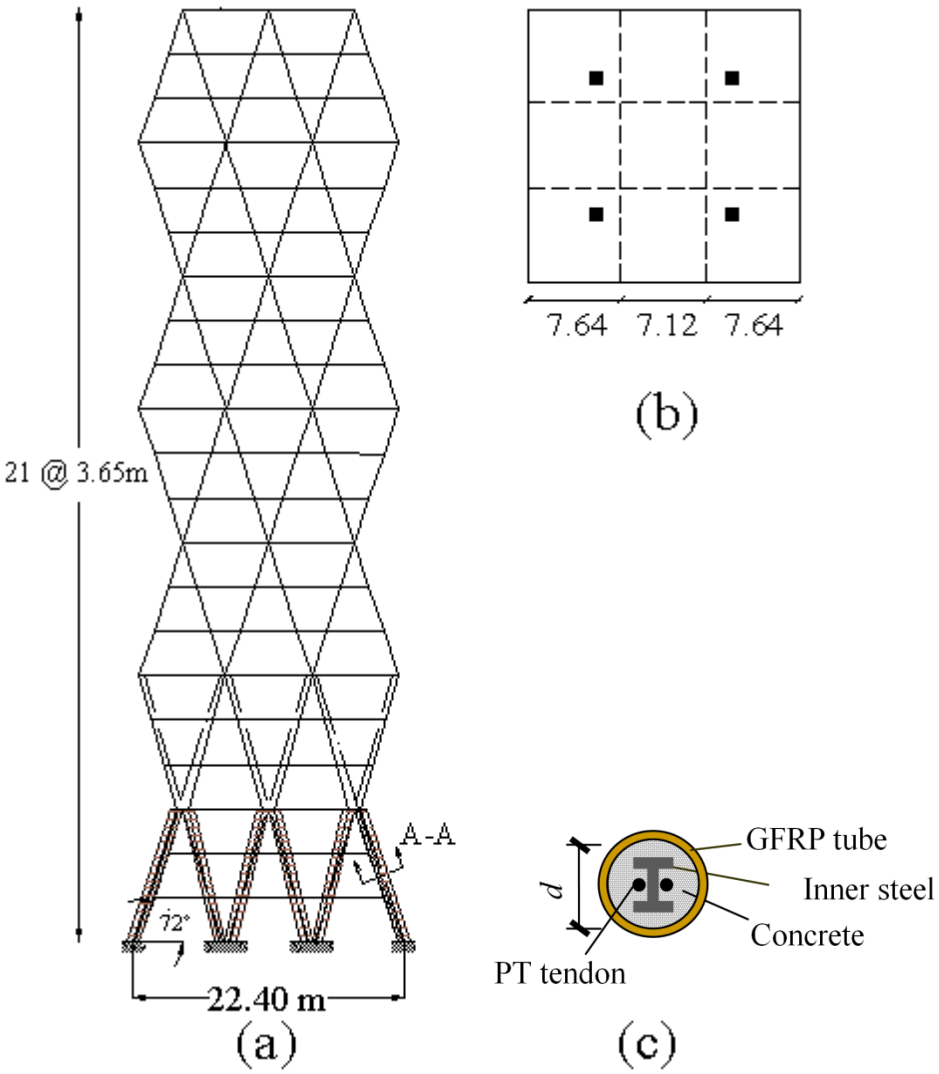

Figure 7- 2. Schematic of a 21-Story hybrid diagrid building: (a) Elevation; (b) Plan; (c) Section A-A of the composite base diagonal

Table 7- 1. Member sizes of 21-story hybrid diagrid building

Story	Cross-sectional (cm^2)	
	Diagonals	**Beams**
3-6	W36x652 (1187)	W36x652 (1160)
7-12	W36x529 (1096)	W40x593 (1096)
13-18	W36x487 (929)	W40x593 (1096)
19-21	W36x395 (729)	W40x593 (1096)

7.5. Numerical Modeling

A two-dimensional finite element model was constructed in OpenSees to study the performance of the hybrid diagrid frame. All the diagonals above the hybrid base were modeled using nonlinear truss elements. The beams were modeled with nonlinear beam-column element. Material behavior of all steel diagonals and beams were modeled using Steel02 material in OpenSees (Menegotto and Pinto, 1973) with 2% isotropic strain hardening and yield strength of 345 MPa (50 ksi).

The diagonals at the first story were considered fixed at their base and were modeled using the similar model of chevron subassembly in Chapter 6. Floor masses were lumped into the beam end nodes at each floor level. In the planar structural model in OpenSees, half of the total seismic mass is assigned to the planar frame due to symmetry of the building plan. The seismic weight of each floor level above the hybrid base module was 5780 kN (1300 kips). To account for additional weight of concrete-filled tubes the seismic weight of 1st to 3rd floors was considered to be 6220 kN (1400 kips).

A lean-on column along the height of the structure, consisting of 21 elastic beam-column elements was used in the model to account for the P-Delta effect and it was pinned at its base. The tributary gravity load of the frame including dead and live loads are applied at each floor level. Half of the load on all gravity columns of the building was assigned to the lean-on column. The load combination presented in Eq. (2-7) was used to calculate the gravity loads and the live load was considered to be 2.87 kN/m^2 (60 psf).

From the Eigen value analysis of the OpenSees model of the 21-story hybrid diagrid building, the first three vibration periods of the 21-story HED diagrid building were obtained as 1.72, 0.45 and 0.26 seconds, respectively

7.6. Nonlinear Static Analysis

The inverted triangular lateral load profile was considered for nonlinear static analysis. The center node at the roof level was selected as the control node for displacement control analysis and the 21-story hybrid diagrid building was gradually pushed to a target roof drift ratio of 2.5%. The pushover curve of the hybrid diagrid structure along with the sequence of plastic deformation development in different elements of the base diagonals is shown in Figure 7- 3.

All the diagonals and beams in the upper structure above the base chevrons remain elastic during the pushover analysis up to 2.5% drift. At roof drift ratio of 0.9% the steel core of the rightmost base diagonal which sustains the maximum compression load yielded. As it was expected, the post-tensioned tendons remain elastic up to high level of lateral forces. The tendon of the leftmost base diagonal which is under maximum tension, started yielding at a roof drift ratio of 1.95%. The steel diagonals at the second module right above the base diagonals started to yield almost at the end of the pushover analysis near 2.5% roof drift ratio. As presented in the next section, the displacement demand on the diagrid building under design basis earthquakes is low (not getting close to 2% roof drift ratio) and hence the post-

tensioned tendons and structural elements above the base module will remain elastic during design basis earthquakes.

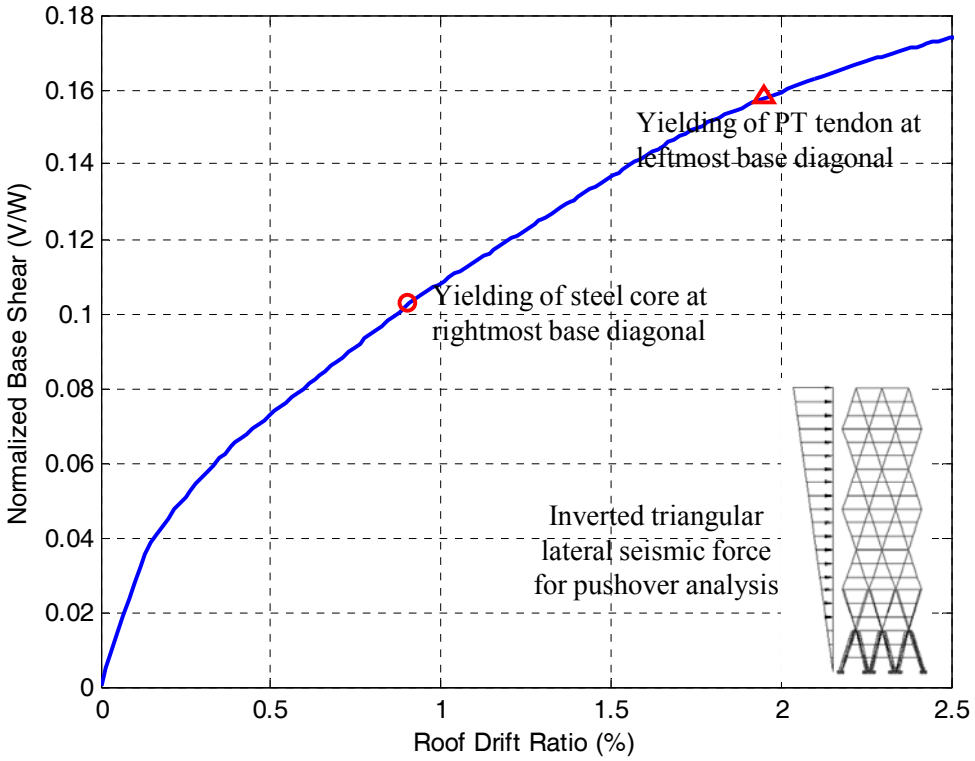

Figure 7- 3. Push-over curve of the 21-story hybrid diagrid building

7.7. Nonlinear Time History Analysis

Certain Engineering Demand Parameters (EDPs) are usually investigated to evaluate the performance of a structure under earthquake. The roof and inter-story drift ratios, residual drift ratios, peak floor displacements, peak base shear ratios and peak ductility demands of diagonals are selected as the EDPs here to evaluate the seismic performance of the 21-story hybrid diagrid structure under a suite of 14 ground motions. The selected strong earthquake records with a probability of exceedance of 10% in 50 years were the same as records used for nonlinear time history analyzes in Chapters 3 and 4 (see Table 3- 2). The sampling interval for the all time history analyses was 0.02 second.

The Newark average-acceleration (γ=1/2, β=1/4) time-step integration method was used to solve the dynamic equations. Rayleigh damping with 2% damping ratio for the first and third modal frequencies of the building were considered for the nonlinear time history analysis in OpenSees model.

7.7.1. Global Deformation Demands

The roof drift ratio time history of the prototype hybrid diagrid building under 14 earthquake records are shown in Figure 7- 4 to Figure 7- 10 . The displacement time histories of the roof, 12th and the 3rd floor of the hybrid diagrid building under LA18 ground motion are shown in Figure 7- 11. One thing to note is that the vibration period observed from this figure is around 3 seconds, which is longer than the fundamental period calculated from Eigen value analysis. This can be attributed to the compression only elements of the composite brace in the base stories of the hybrid diagrid structure.

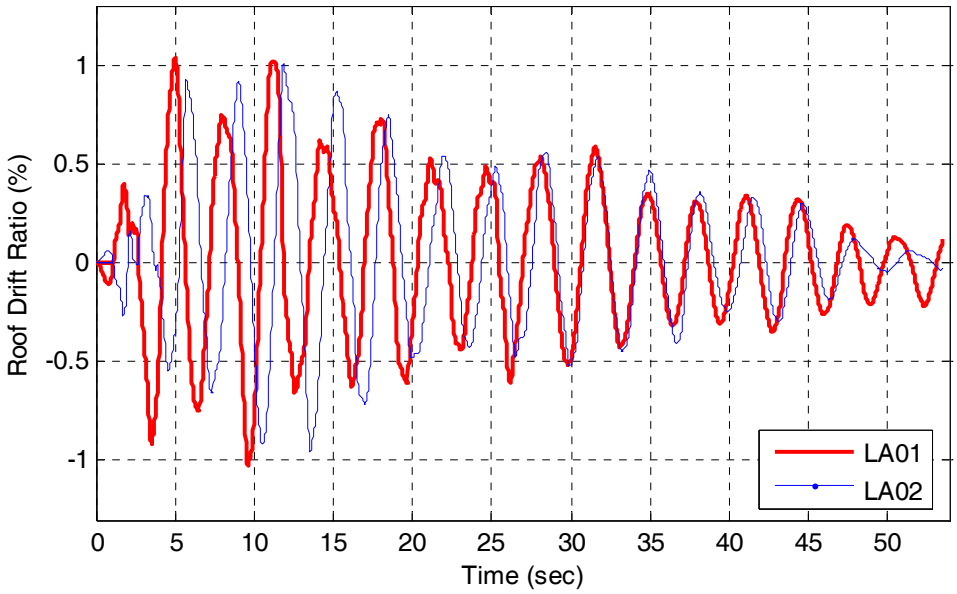

Figure 7- 4. Roof drift ratio time history of 21-story hybrid diagrid building under LA01 and LA02

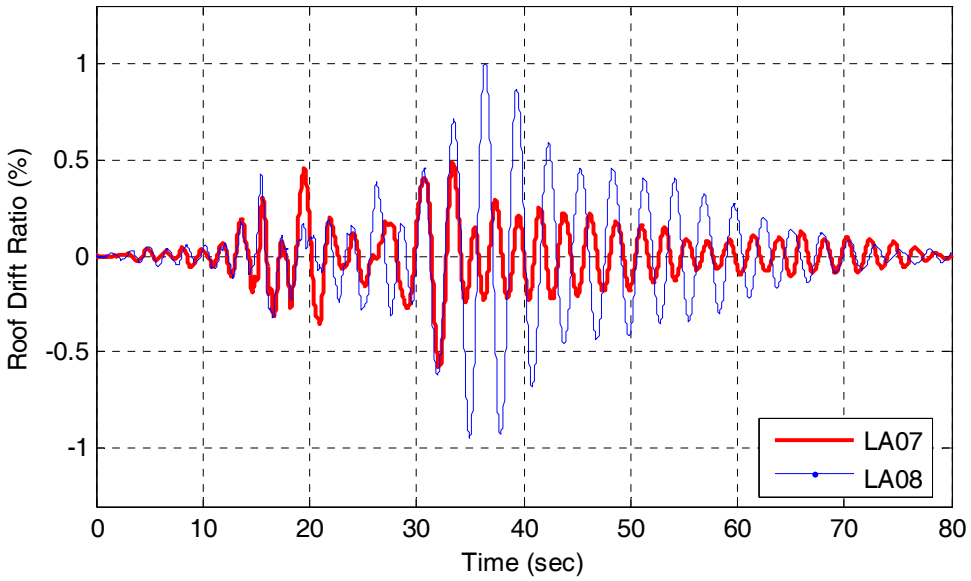

Figure 7- 5. Roof drift ratio time history of 21-story hybrid diagrid building under LA07 and LA08

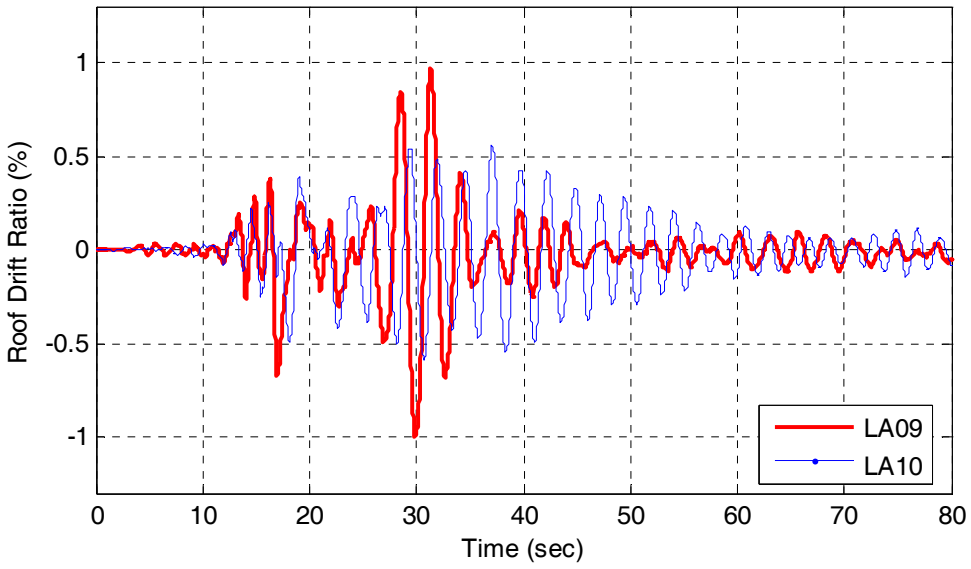

Figure 7- 6. Roof drift ratio time history of 21-story hybrid diagrid building under LA09 and LA10

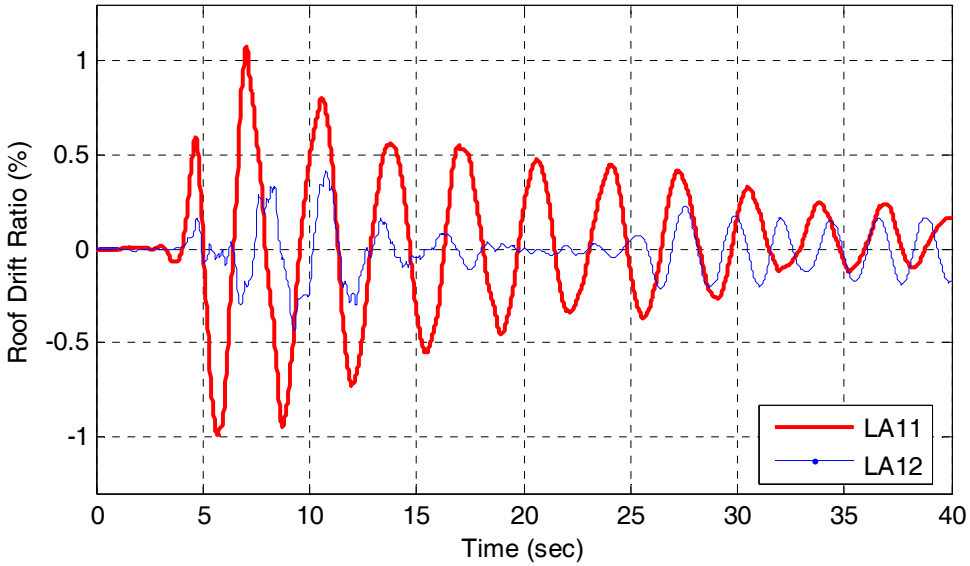

Figure 7- 7. Roof drift ratio time history of 21-story hybrid diagrid building under LA11 and LA12

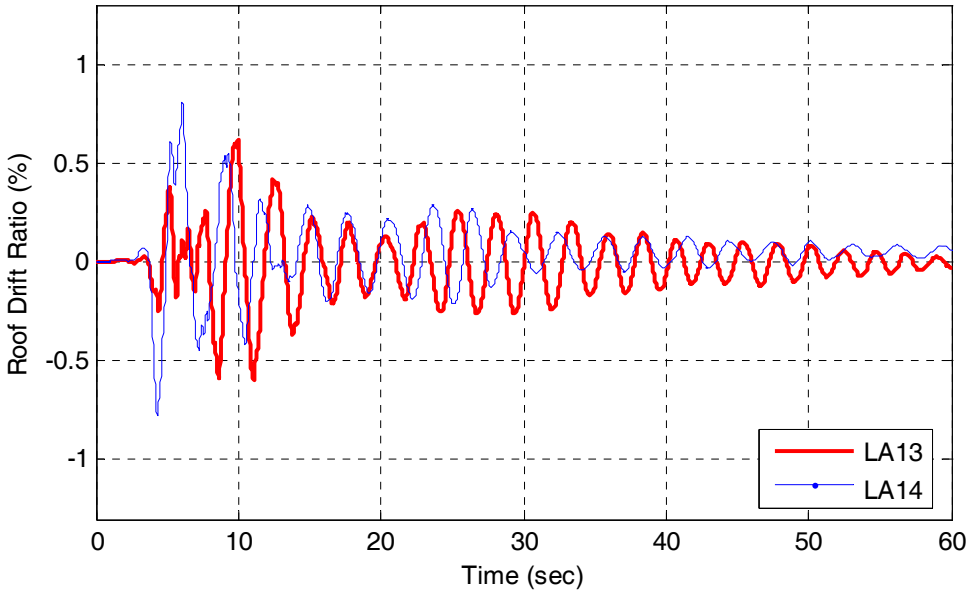

Figure 7- 8. Roof drift ratio time history of 21-story hybrid diagrid building under LA13 and LA14

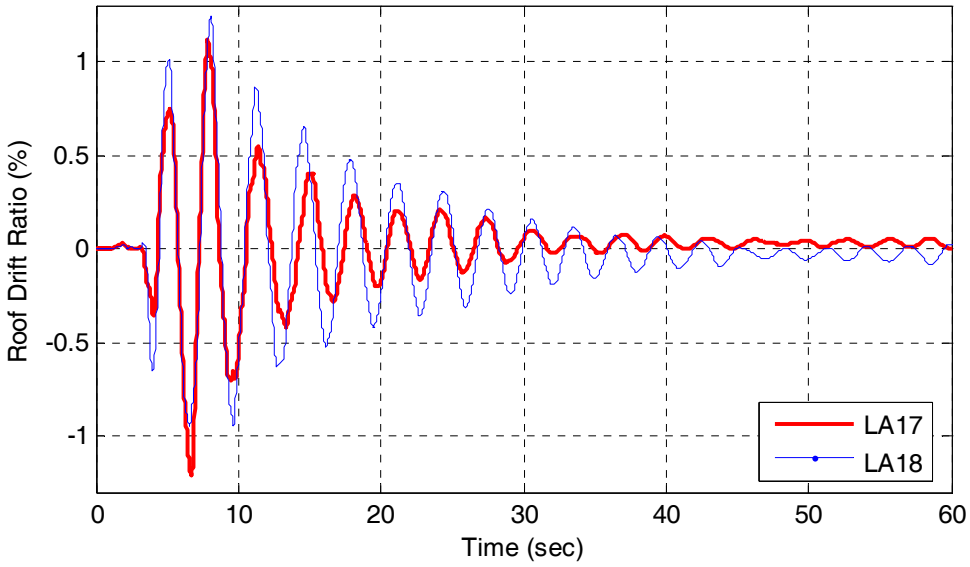

Figure 7- 9. Roof drift ratio time history of 21-story hybrid diagrid building under LA17 and LA18

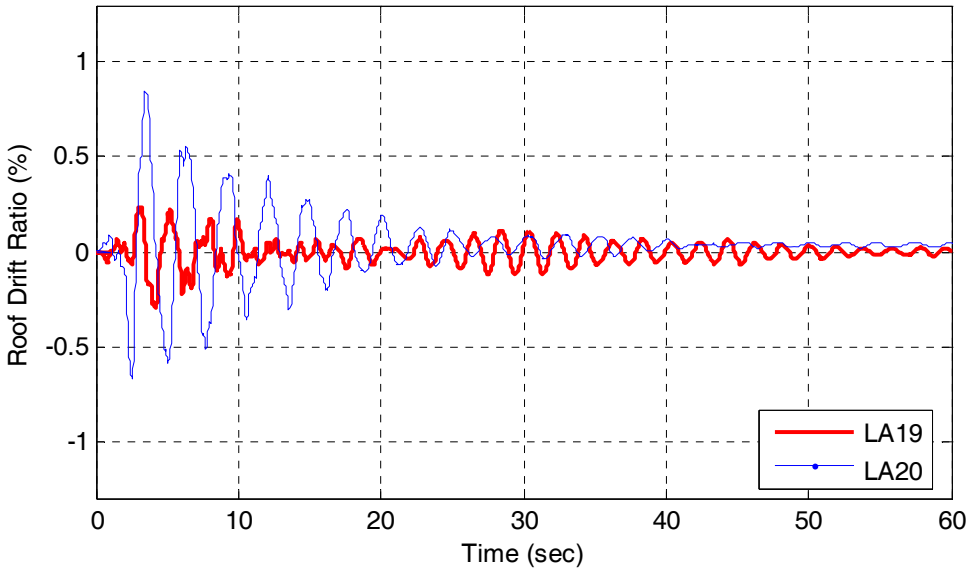

Figure 7- 10. Roof drift ratio time history of 21-story hybrid diagrid building under LA19 and LA20

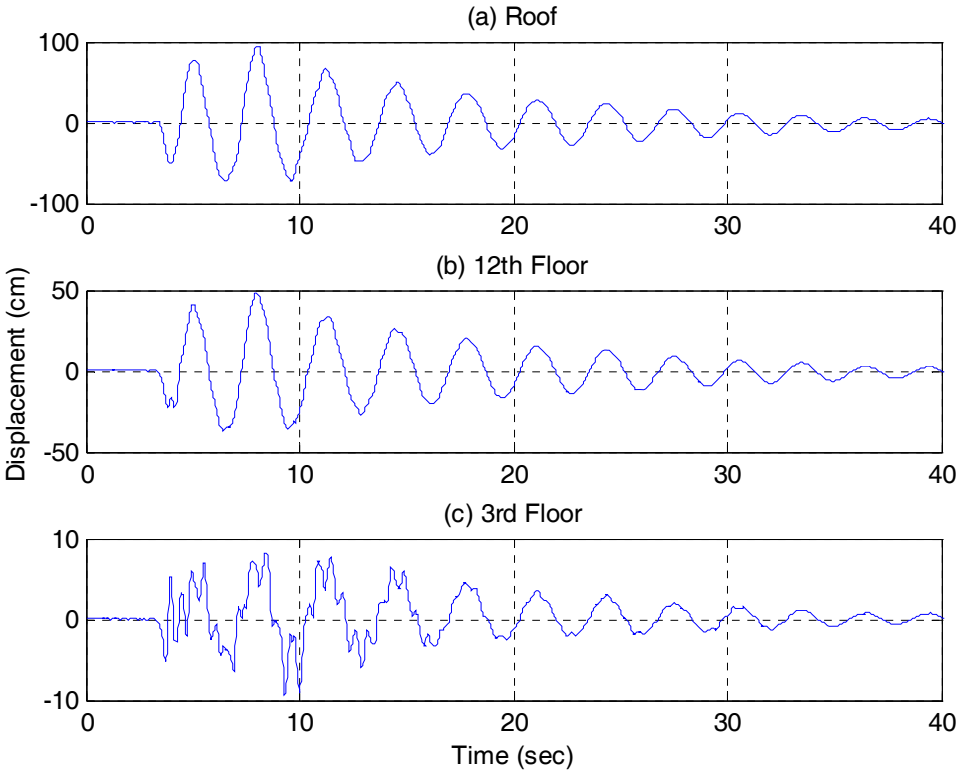

Figure 7- 11. Displacement time history of the selected floors of the 21-story hybrid diagrid building subjected to LA18 earthquake record

Figure 7- 12 shows the maximum roof drift ratio under 14 earthquake records. The ensemble average of the maximum roof drift ratio was 0.84%. Figure 7- 13 shows the residual roof drift ratio for each earthquake record. The ensemble average of roof residual drift ratio values was 0.024%. The very small values of the roof residual drift ratios demonstrate the self-centering behavior of the proposed hybrid diagrid structure. The highly stiff structure above the base module remains elastic during earthquake and acts more like a rigid body of the rocking system. The chevrons at the base re-center the structure under lateral loading and dissipate energy through yielding of the steel core and the GFRP-tube confined concrete.

Figure 7- 14 shows the peak floor displacement responses of the hybrid diagrid building subjected to each ground motion. The maximum roof displacement of 95.6 cm occurred under LA18 which corresponds to the roof drift ratio of 1.24%.

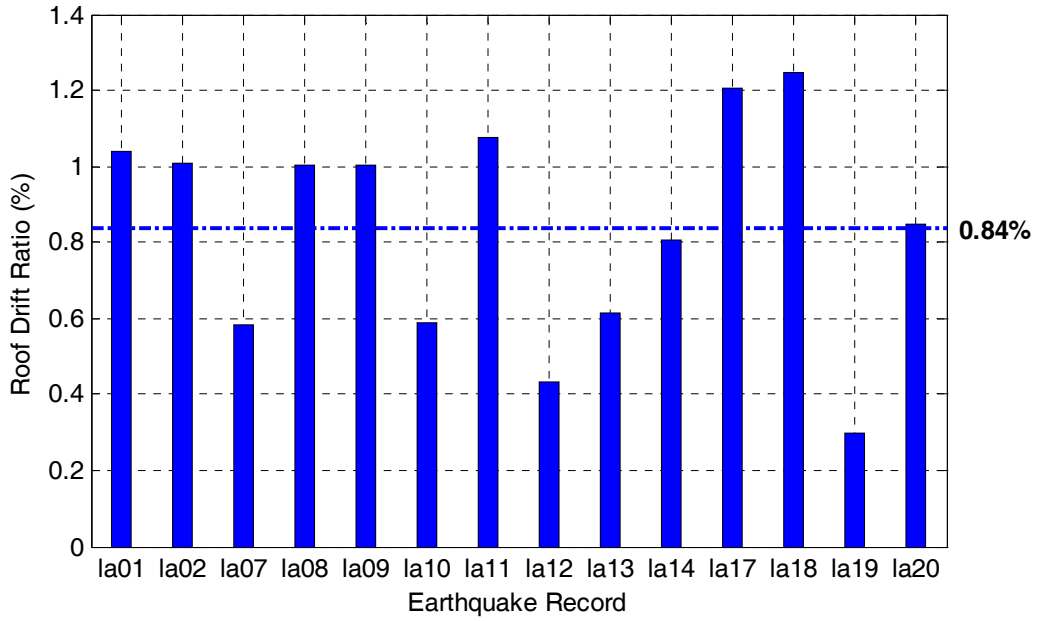

Figure 7- 12. Maximum roof drift ratios of 21-story hybrid diagrid building under 14 earthquake records

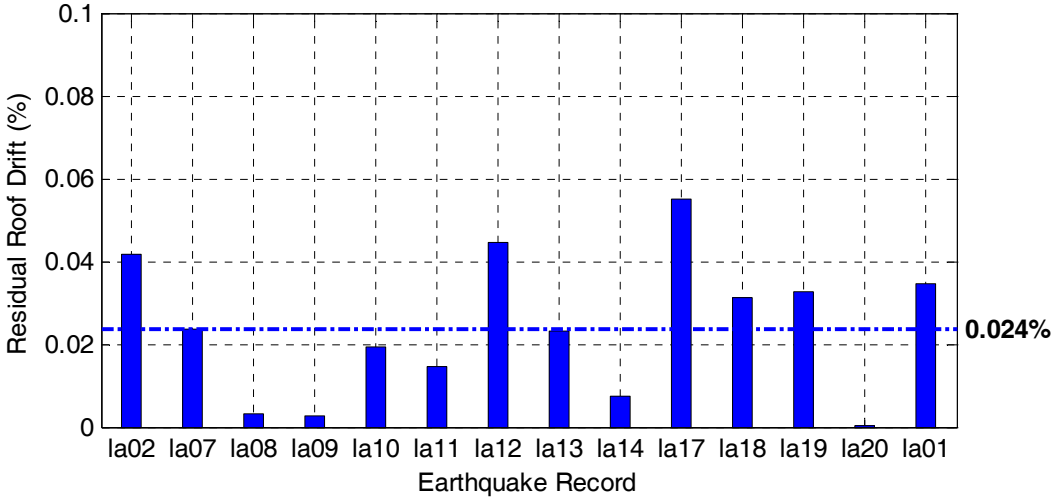

Figure 7- 13. Residual roof drift ratios of 21-story hybrid diagrid building under 14 earthquake records

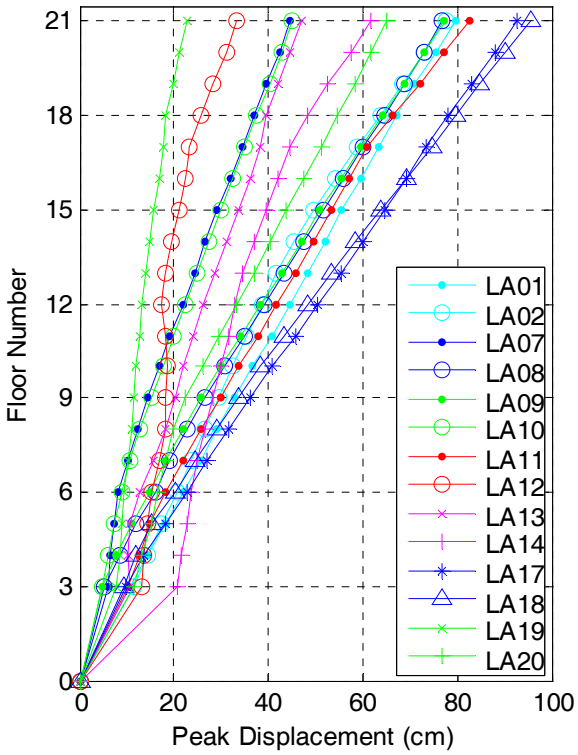

Figure 7- 14. Distribution of the peak displacement of the 21-story hybrid diagrid building under 14 earthquake records

7.7.2. Local Deformation Demands

The inter-story drift ratio is a suitable measure to assess the level of nonstructural damage of the building under earthquake loading. Figure 7- 15 shows the distribution of the peak inter-story drift ratios under each ground motion record. The dark circles show the values of the ensemble average inter-story drift ratios with the maximum value of 1.25% occurring at 18th story. Except the inter-story drift ratio at the 3rd story under LA14 which is about 1.9%, the maximum peak inter-story drift ratio occurred at 12th story under LA18 was 1.65%. The maximum inter-story drift ratio limit specified in ASCE/SEI 7-10 for nonlinear time-history analysis is 2.5%. The large triangles in Figure 7- 15 show the peak inter-story drift ratios of the building under LA18 earthquake ground motion.

The maximum inter-story residual drift ratio for each earthquake record is shown in Figure 7- 16. The ensemble average of maximum residual inter-story drift ratio is 0.047%. The biggest residual inter-story drift ratio was 0.084% occurred under LA12. The maximum inter-story residual drift ratio values ware generally observed at the 6th and 7th stories. The very values of the inter-story residual drift ratios reconfirms the conclusion regarding the self-centering behavior of the proposed hybrid diagrid structure already expressed from low roof residual drift ratios. The structure above the hybrid base diagonals behaves like a rigid block resulting is very low residual displacements after the earthquake.

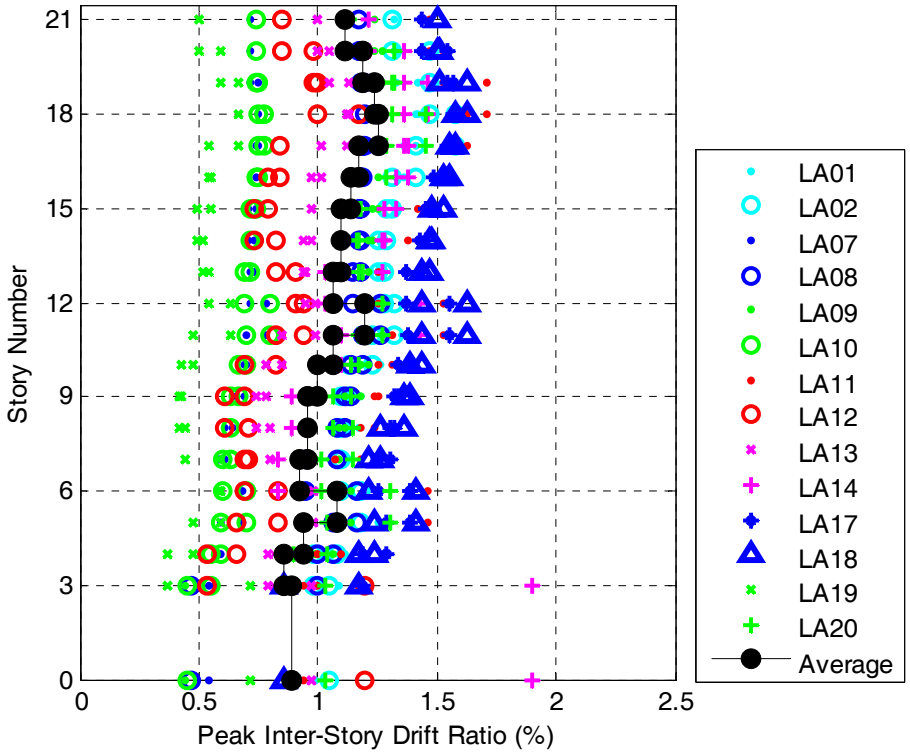

Figure 7- 15. Distribution of peak inter-story drift ratio of the hybrid diagrid building under 14 earthquake records

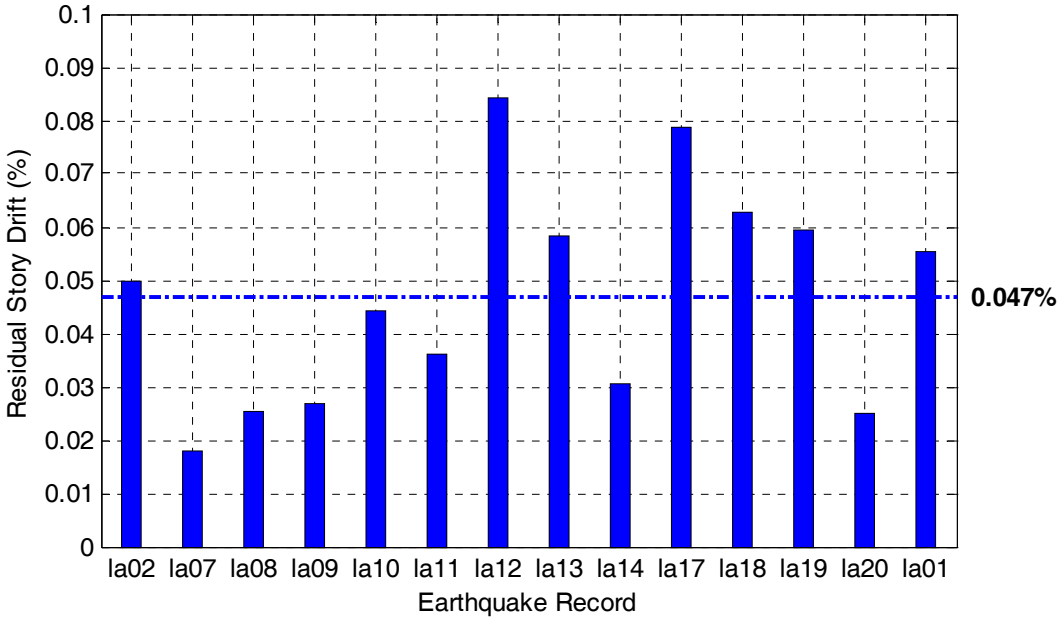

Figure 7- 16. Maximum residual inter-story drift ratio of 21-story hybrid diagrid building under 14 earthquake records

7.7.3. Structural Members Ductility Demands

7.7.3.1. Composite Base Diagonals

Figure 7- 17 shows the maximum ductility demand of the GFRP-confined concrete, steel core and the PT tendons under each earthquake. The ensemble average of peak ductility demand value of 0.51 and the maximum peak ductility demand of 0.7 (occurred under LA17) for PT tendons ensure that all tendons remain elastic under 14 earthquakes. The ensemble average of peak ductility demands for the steel core and GFRP-tube confined concrete were 2.19 and 1.89, respectively.

The stress-strain hysteresis of GFRP-tube confined concrete and the steel core the leftmost and rightmost base diagonals under LA18 are shown in Figure 7- 18.

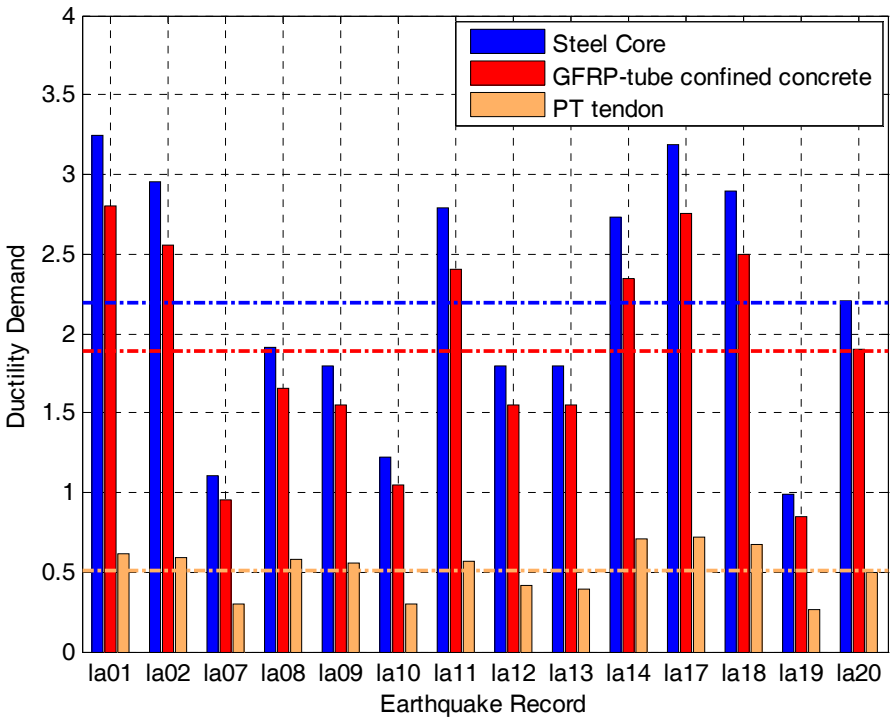

Figure 7- 17. Ductility demands of components of the base diagonals of the hybrid diagrid building under 14 earthquake records

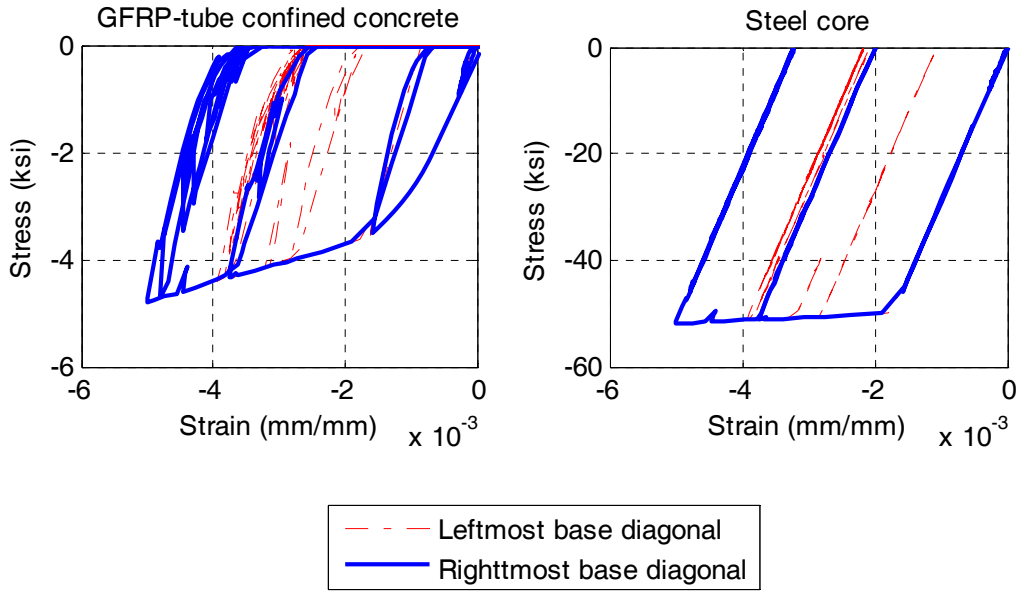

Figure 7- 18. Force-displacement hysteresis of components of leftmost and rightmost base diagonals of hybrid diagrid building under LA18 earthquake record

7.7.3.2. Other Structural Elements

By checking the maximum stress on all beams of 21-story hybrid diagrid building it was insured that they all remained elastic under all 14 earthquake records.

Figure 7- 19 shows the maximum ductility demand of diagonals above the composite base module. The dark circles connected with a line, show the ensemble average of peak ductility demand of diagonals of each story under 14 earthquake records. The maximum ensemble average of peak ductility demand was 0.78 for the diagonals at the 4th story right above the composite base diagonals. The maximum residual inter-story drift of 0.084% under LA12 shown in Figure 7- 16 that was the greatest among all 14 earthquake records, is related to big ductility demands of diagonals under this record as shown in Figure 7- 19. The diagonals could be designed with larger sections to further decrease the ductility demands.

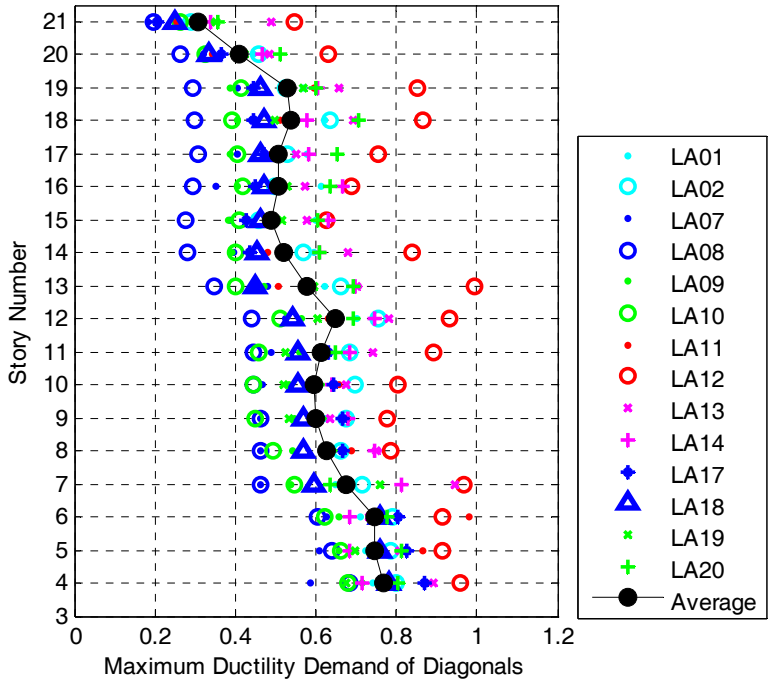

Figure 7- 19. Maximum ductility demands of diagonals of 21-story hybrid diagrid frame

7.7.4. Base Shear Demands

Figure 7- 20 shows the maximum base shear ratios sustained by the hybrid diagrid building under the 14 earthquake records. The ensemble average of maximum base shear ratios is 0.085. The maximum peak base shear ratio of 0.125 occurred under LA14.

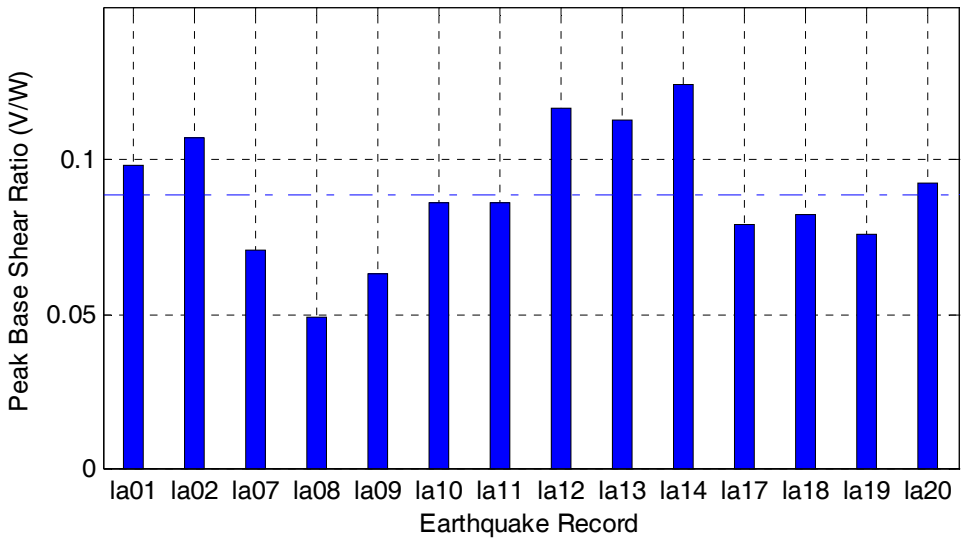

Figure 7- 20. Maximum base shear of the 21-story hybrid diagrid building under 14 earthquake records

7.7.5. Floor Acceleration

Figure 7- 21 (a), (b) and (c) shows the acceleration time history of the building at the roof, 12th and 3rd floors under LA18 ground motion. The peak floor acceleration values under LA18 along the building height are shown in Figure 7- 21 (d).

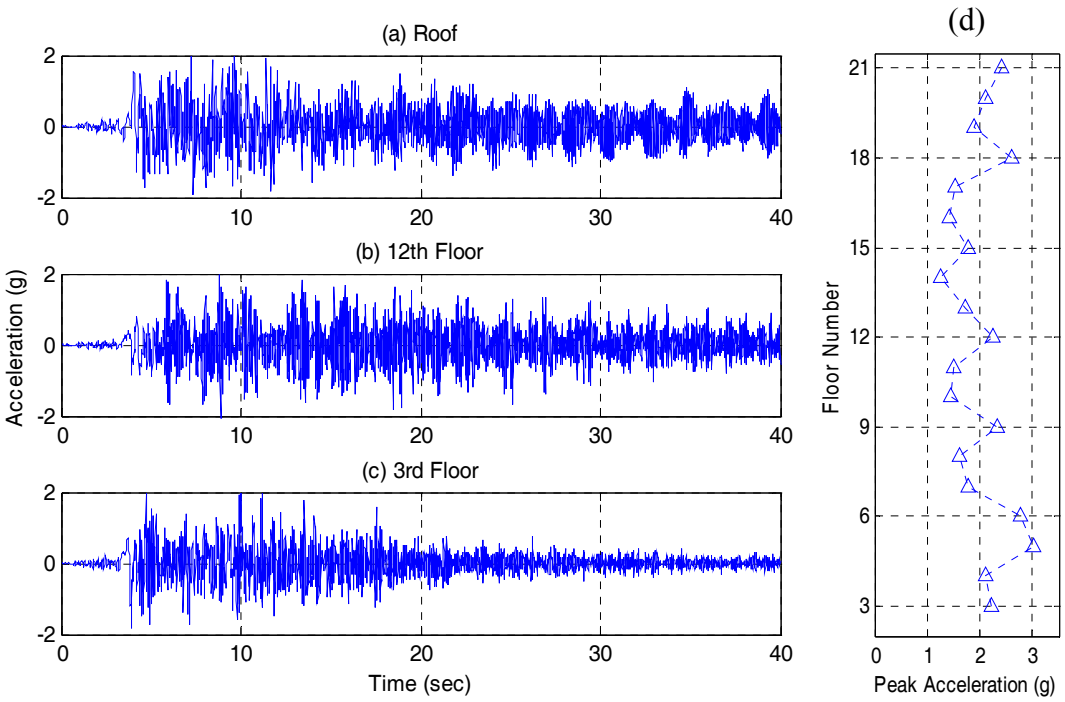

Figure 7- 21. Floor acceleration response of the 21-story hybrid diagrid building under LA18: (a) Roof acceleration time history; (b) 12th floor acceleration time history; (c) 3rd floor acceleration time history; (d) Distribution of peak floor acceleration

7.8. Summary and Conclusions

The conventional diagrid structure is visually appealing and structurally efficient under gravity loading and low level of lateral forces but prone to high inelastic deformation demands in primary load carrying members during strong earthquakes. A composite diagonal element consisting of GFRP-tube confined concrete, steel core and post-tensioned tendons proposed in Chapter 6, was used as self-centering base diagonals of a prototype hybrid diagrid building in this chapter.

Designing a stiff network of diagonals and beams above the base module to keep them elastic during earthquake, a rocking system was pursued with self-centering chevrons installed at the base module of a 21-story diagrid building. From nonlinear time history analyses, a favorable seismic performance was observed for the hybrid diagrid structure in terms of controlling peak drift and residual drift. The ensemble average of maximum residual roof drift ratio and residual inter-story drift ratio under the 14 strong earthquake records were 0.024% and 0.047%, respectively. The average maximum base shear ratio under the 14 earthquake records was found to be 0.084. The numerical results show that the hybrid diagrid structure exhibits nearly self-centering behavior (e.g. almost zero residual drifts) without sustaining a large base shear. The rocking behavior assures the minor structural damage and subsequently immediate operation of the building after a strong earthquake.

It can be concluded that the proposed self-centering chevron braces to be used as base elements for the hybrid diagrid structure provides the conventional diagrid frame with re-centering capability. The base chevrons re-center the whole structure post seismic events and retain the rest of the diagrid structure elastic during the

earthquake. Therefore, it provides a promising alternative design for diagrid structural system to be used in high seismic regions.

CHAPTER 8 : SUMMARY, CONCLUSIONS AND RECOMMENDATIONS

8.1. Research Summary

The diagrid structural framing system which is a network of planar or curved-surfaced triangular grids has been used in recent years for high-rise buildings. A competent seismic force-resisting system must have good ductility and stable energy dissipation mechanism to accomplish the design goal of life safety when subjected to severe earthquake ground motions; based on analysis, the diagrid structural system can have improved ductility and energy dissipation capacity through innovative design. The main objective of this research is to develop and implement such innovative design concepts in diagrid structural system while retaining its architectural flexibility and elegance. A summary of performed research work toward this objective is as follows:

- The characteristics of diagrid framing system were discussed in Chapter 2 and nonlinear static analysis of a case study 21-story diagrid building was performed.
- A new lateral-force resisting system termed highly energy-dissipative ductile (HED) diagrid framing system consisting of diagonals and beams, and fuse elements for dedicated energy dissipation (shear links in this study) was proposed in Chapter 3. The seismic performance of the proposed system was investigated through nonlinear time history analysis of a 21-

story case study building under an ensemble of 14 earthquake records scaled to the design basis earthquake (DBE) at Los Angles, California region.

- A parametric study of the effects of length of shear links and inclination angle of diagonals on the seismic performance of HED diagrid system was conducted in Chapter 4. A total of four case studies were defined and nonlinear static and time history analysis of each case under an ensemble of 14 DBE ground motion records were performed and the results were compared and discussed.
- The experimental and analytical studies of GFRP-tube confined concrete with high volumetric confinement ratio were conducted with the purpose of providing a ductile axial load carrying element that could be adopted for use in the diagonals.
- An analytical tool for numerical simulation of GFRP-tube confined concrete material with high volumetric confinement ratio was developed to enable the finite element analysis of complex structures using elements with this type of material.
- The concept of a self-centering chevron consisting of post-tensioned steel tendons, steel core and GFRP-tube confined concrete was examined in Chapter 6. A parametric study on the influence of the brace angle, the area ratio of post-tension tendons, the area ratio of steel core and yield strength of the steel core on hysteretic behavior of the composite chevron was performed.

- The second diagrid-based new seismic resisting system termed hybrid diagrid framing system was proposed in Chapter 7. This system utilizes the self-centering composite chevrons as its base diagonals to create a rocking system with re-centering behavior.

8.2. Outcomes and Conclusions

In search of alternative approaches to improve the seismic performance of conventional diagrid framing system, the seismic performance of two newly proposed systems was examined and the following conclusions were drawn:

- The nonlinear static analysis of a conventional 21-story diagrid building showed that this system is subjected to yielding of considerable number of diagonal yielding as soon as the building was deformed beyond its linear elastic point. This is unfavorable to the goal of achieving high ductility and energy dissipation in seismic load resisting systems.
- It was concluded that the HED diagrid framing system provides a promising seismic resistant structural system with large energy dissipation capacity due to the use of dedicated fuse elements (i.e. shear links in this study). The findings from nonlinear time history analysis verified that under DBE-level earthquake loading, the damage can be confined to the shear links which are easy to replace post earthquakes and would thus cause less interruptions to the operation of the building.
- Among the cases analyzed in parametric study of Chapter 4, the building with shorter shear links (i.e. case SL-1) showed a better result for some engineering demand parameters including lower inter-story drift ratios and lower base shear ratios. No significant improvement in seismic performance was observed for other cases. Specifically, increasing the inclination angle of the diagonals in case DS-2, deprived the seismic performance of the

building with the most significant increase in roof drift ratios, residual roof drift ratios, inter-story drift ratios and residual inter-story drift ratios.

- Through an experimental study and comparison of test results with other GFRP-tube confined concrete experimental data, it was shown that the volumetric confinement ratio has a significant effect on increasing the ductility of concrete and therefore primary failure mode in FRP-confined concrete axial elements due to hoop tensile rupture of fibers can be considerably postponed by increasing the confinement ratio. Also, higher volumetric confinement ratio increases the strength of GFRP-tube confined concrete since it results in higher slope of post confinement branch of the stress-strain curve.
- In search of an appropriate model to predict the stress-strain behavior of the proposed GFRP-tube confined concrete with high volumetric confinement ratio, a constitutive model was adapted and calibrated with the experimental results to properly simulate the stress-strain behavior of such GFRP-tube confined concrete with high confinement ratio.
- The proposed hysteretic model of GFRP-tube confined concrete was implemented into finite element analysis platform, OpenSees as an uniaxial material. The dynamic library developed to create the material object can be modified for calibrated models if variation in FRP-confined concrete material property is to be considered.

- The numerical analysis of the proposed composite chevron showed that two inclined components of the composite brace assembly work synergistically and exhibit symmetric self-entering behavior under lateral loading.
- The results of the parametric study on the composite chevron showed that the slop of braces and the area ratio of post-tensioning steel tendons have the most significant effect on the load behavior of the composite chevron.
- From the nonlinear time history analysis results given in Chapter 7, it was concluded that the proposed hybrid diagrid framing system provides a promising alternative design for diagrid structures in high seismic regions. The time history analysis results confirmed the re-centering behavior of the structure post seismic events due to composite base chevrons. It was shown that the inter-story residual displacements were very small and that the rest of the diagrid structure above the composite base remained elastic during the earthquake.

8.3. Contribution to the Structural Engineering Field

Modern architecture challenges structural engineers to provide new design options that allow visual elegancy without sacrificing the structural efficiency. Diagrid framing system as a visually appealing and geometrically flexible structure has attracted the attention of architects in recent years; however there are few comprehensive researches done on the seismic performance of diagrid structural system. Diagrid has not been included as a seismic force-resisting system among building frame systems in ASCE 7-10. The diagonals in a diagrid structure cannot be compared to braces in regular braced frame systems such as concentrically braced frames or eccentrically braced frames because diagonals are the main load carrying elements under both gravity and lateral loading and their failure causes serious consequences to the stability of the structure. Despite the high stiffness and redundancy of diagrid frame, the limited ductility and lack of energy dissipating elements makes this system vulnerable under moderate and strong earthquakes.

This research contributes to structural engineering field with proposing two new alternatives for diagrid system in high seismic region for mid-rise and high-rise buildings design. HED diagrid frame offers improved ductility and energy dissipation capacity through dedicated fuse element of shear links. In hybrid diagrid framing structure, the base diagonals of a conventional steel diagrid is improved to create a rocking system with self-centering behavior. It was shown that both proposed systems have good seismic performance under strong ground motions while they maintain the architectural advantages of diagrid system (e.g. angular configuration).

8.4. Recommendations for Future Research

The focus of this study was on developing new alternatives with improved ductility and energy dissipation capacity for conventional diagrid framing system and demonstrating the promise of proposed systems as seismic-force resisting structures that not only are structurally efficient but also keep the architectural flexibility of the diagrid system. The nonlinear time history analysis results of prototype buildings with proposed structural systems fulfilled these objectives and showed that these systems are prospective design options for high seismic regions. There are research questions and assumptions that can be clarified in a further study. Further research could be conducted in the following subjects:

1- The analytical model of the buildings with HED diagrid framing system in Chapter 3 and hybrid diagrid framing system in Chapter 7, were two dimensional planar frames. Three-dimensional models which demand higher analysis cost but account for out-of plane effects such as torsion and shear lag, could be developed in a future research to perform more detailed nonlinear time history analysis of the proposed systems.

2- This research focused on presenting two new structural systems and analyzed case studies of each type to show their promises as seismic-force resisting systems. It was shown in Chapter 4 that different design parameters can affect the seismic performance of the HED diagrid frame. Also, the parametric study of self-centering composite chevron in Chapter 6 investigated the influence of different design parameters on energy dissipation, strength and stiffness of the chevron. Future research with the concentration on design methodology of

HED diagrid building and hybrid diagrid building could provide guidelines and criteria for seismic design of these structures for construction. Detailing guideline could also be developed with experimental data.

3- The GFRP-tube confined concrete specimens with high volumetric confinement ratio presented in Chapter 5 were casted in two sizes. The capacity of the testing machine used in this study was not large enough to test the bigger specimens which had a more common cylinder size (158x280 mm) that is typically used in this type of research. It was shown that the increase in strength and ductility of confined concrete intensifies significantly with increasing the volumetric confinement ratio. A future experimental research on monotonic and cyclic behavior of this type of confined concrete material using larger quantity and size of specimens will provide more experimental results and better verify the accuracy of the presented analytical model.

REFERENCES

American Concrete Institute (ACI), (2008). "Guide for the design and construction of externally bonded FRP systems for strengthening of concrete structures." *ACI 440.2R-08*, Farmington Hills, Mich.

AISC. (2005). "Seismic provisions for structural steel buildings." *ANSI/AISC 341-05*. Chicago, IL.

Ajrab, J., Pekcan, G., and Mander, J. B. (2004). "Rocking Wall-Frame Structures with Supplemental Tendon Systems," *Journal of Structural Engineering*, ASCE, 130 (6), 895 - 903.

Ali, M. M., Moon, K.-S. (2007). "Structural development in tall buildings." *Architectural Science Review*, Vol. 50, No. 3, September 2007.

ASCE. (2010). "Minimum design loads for buildings and other structures." *ASCE/SEI 7-10/ANSI,* Reston, Va.

Baker, W., Besjak, C., Sarkisian, M., Lee, P., and Doo, C. S. (2010). "Proposed Methodology to Determine Seismic Performance Factors for Steel Diagrid Framed Systems." *CTBUH Technical Paper.*

Buyukozturk, O., and Hearing, B. (1998). "Failure behavior of precracked concrete beams retrofitted with FRP" J. Compos. Constr,, Vol. 2, No. 3, pp. 138-144.

Carroll, C., Duan, X., Gibbons, C., Lawson, R., Lee, A., Luong, A., Mcgowan R. and Pope, C. (2006). "China Central Television Headquarters - Structural design." *International J. Steel Structures*, 6: 387-391.

Chang, G.A., and Mander, G.B. (1994). "Seismic energy based fatigue damage analysis of bridge columns: Part I – evaluation of seismic capacity." *Technical Report NCEER-94-0006.*

Charnish, B., McDonnell, T., Yolles, H. (2008). "The Bow: Unique Diagrid Structural System for a Sustainable Tall Building." *CTBUH 8th World Congress.*

Cheng, C.-T. (2008). "Shaking table tests of a self-centering designed bridge substructure." *Engineering Structures*, 30, 3426-3433.

Christopoulos, C., Tremblay, R., Kim, H.-J., and Lacerte, M. (2008). "Self-centering energy dissipative bracing system for the seismic resistance of structure: development and validation." *ASCE J. of Struct. Eng.*, 134(1):96–107.

Chou, C. C. and Chen J. H. (2010). "Column restraint in post-tensioned self-centering moment frames", *Earthquake Engineering and Structure Dynamics*, 39, 751-774.

Dolce, M. D., Cardone, D., and Marnetto, R. (2000). "Implementation and testing of passive control devices based on shape memory alloys." *Earthquake Eng. Struct. Dyn.*, 29(7), 945–968.

Fam, A. Z., and Rizkalla, S. H. (2001a). "Behavior of axially loaded concrete-filled circular fiber-reinforced polymer tubes", *ACI Struct. J.*, 98(3): 280-289.

Fam, A. Z., and Rizkalla, S. H. (2001b). "Confinement model for axially loaded concrete confined by circular fiber-reinforced polymer tubes." *ACI Struct. J.*, 98(4): 451-461.

Gilmore A. T., and Cambray, N. (2009). "Preliminary design of low-rise buildings stiffened with BRB by a displacement approach."*Earthquake Spectra*, 25(1): 185-211

Hajjar, J. F., Schiller, P. H., and Molodan, A., (1998). "A distributed plasticity model for concrete-filled steel tube beam-columns with interlayer slip.", *Eng. Struct.*, 20(8): 663-676.

Hajjar, J. F., Eatherton, M., Ma, X., Deierlein, G. G., and Krawinkler, H. (2010). "Seismic Resilience of Self-Centering Steel Braced Frames with Replaceable Energy-Dissipating Fuses – Part I: Large-Scale Cyclic Testing", *Proceedings, the Seventh International Conference on Urban Earthquake Engineering*, Tokyo, Japan, March 3-5, Center for Urban Earthquake Engineering, Tokyo Institute of Technology, Tokyo, Japan.

Harajli, M.H., Hantouche, E., and Soudki, K. (2006). "Stress–strain model for fiber-reinforced polymer jacketed concrete columns." *ACI Struct. J.*, 105(5): 672–82.

Hjelmstad, K.D. and E.P. Popov, (1983). "Cyclic behavior and design of link beams." *J. Struct. Eng. ASCE,* 109(10): 2387-2403.

Holden, T., Restrepo, J. and Mander, J.B. (2003). "Seismic performance of precast reinforced and prestressed concrete walls", *ASCE Journal of Structure Engineering*, 129(3), 286-296.

Housner, G. W. (1963). ''The behavior of inverted pendulum structures during earthquake.'' *Bull. Seismol. Soc. Am.*, 53(2):403–417.

Jeong, H. and Mahin, S. (2007). "Evaluation of self-centering reinforced concrete columns by shaking table tests and numerical simulations." *PEER Report*, University of California, Berkeley, CA.

Kim, J. and Lee, Y.H. (2009). "Progressive collapse resisting capacity of tube-type structures." *The Structural Design of Tall and Special Buildings*, 10: 1002/tal.512

Kim, Y.J., Jung, I.Y., Ju, Y-K., Park, S.J. and Kim, S.D. (2011). "Cyclic behavior of diagrid nodes with H-section braces," *J. Struct. Eng*. ASCE, 136(9): 1111-1122.

Krawinkler, H, Seneviratna, GDPK. (1998). "Pros and cons of a pushover analysis of seismic performance evaluation," *Engineering Structures*, 20(4–6):452– 464.

Kurama, Y., Sause, R., Pessiki, S. and Lu, L.-W. (1999). "Lateral load behavior and seismic design of unbonded post-tensioned precast concrete walls", *ACI Structural Journal*, 96(4), 622–632.

Lam, L., and Teng, J. G. (2002). "Strength models for fiber-reinforced plastic-confined concrete." *ASCE J. Struct. Eng.*, Vol. 128, No. 5, 2002/5-612-623.

Lam, L., Teng, J. G., Cheung, C.H., and Xiao, Y. (2006). "FRP-confined concrete under axial cyclic compression." *Cement & Concrete Composites*, 28: 949-958.

Lee, W. K., and Billington, S. L. (2011). "Performance-based earthquake engineering assessment of a self-centering, post-tensioned concrete bridge system." *Earthquake Engineering & Structural Dynamics*, 40:887-902

Leonard, J. (2007). "Investigation of shear lag effect in high-rise buildings with diagrid system." *M.Sc. Thesis*, Department of Civil and Environmental Engineering, Massachusetts Institute of Technology

Li, G. (2006). "Experimental study of FRP confined concrete cylinder", *Engineering Structures*, 28: 1001-1008.

Lorenzis, L., and Tepfers, R. (2003). "Comparative study of models on confinement of concrete cylinders with fiber-reinforced polymer composites." *J. Compos. Constr.,* 3: 219–237.

Mander, J. B., Priestley, M. J. N., and Park, R. (1988). “Theoretical stress–strain model for confined concrete.” *J. Struct. Eng.*, 114(8): 1804–26.

Mander, J. B., and Cheng, C.-T. (1997). ‘‘Seismic resistance of bridge piers based on damage avoidance design.’’ *Tech. Rep. NCEER-97-0014*, National Center for Earthquake Engineering Research, Buffalo, N.Y.

Mansour, N., Shen, Y., Christopoulos, C., Tremblay, R. (2008). “Seismic design of EBF steel frames using replaceable nonlinear links.” *Proc. 14th World Conference on Earthquake Engineering*, Beijing, China.

The Mathworks Inc., “MATLAB, the language of technical computing”.

Mazzoni, S., McKenna, F., Scott, M.H., and Fenves, G.L. (2009). "The Open System for Earthquake Engineering Simulation (OpenSEES) User Command-Language Manual." *Pacific Earthquake Eng. Research Center,* Univ. Calif., Berkeley, CA, (http://opensees.berkeley.edu).

McKenna, F.T. (1997). “Object-oriented finite element programming: frameworks for analysis, algorithms and parallel computing.” *Ph.D. Thesis*, University of California, Berkeley, CA.

McKenna, F.T. (2009). “OpenSees Dynamic API”, University of California, Berkeley

Menegotto, M. and Pinto, P.E. (1973). “Method of analysis of cyclically loaded RC plane frames including changes in geometry and non-elastic behavior of elements under normal force and bending, Preliminary Report.” *IABSE,* Vol. 13, pp. 15-22.

Mirmiran, A., and Shahawy, M. (1997). “Behavior of concrete columns confined by fiber composites.” *J. Struct. Eng.*, 123(5):583-590.

Mirmiran, A., Shahawy, M., and Beitleman, T. (2001) “Slenderness limit for hybrid FRP-concrete columns.” *J. Compos. Const.* 5(1):26–34.

Mohamed, H. M., and Masmoudi, R. (2010). “Axial load capacity of concrete-filled tube columns: experimental versus theoretical predictions”, *J. Compos. Constr.*, 14(2): 231-243.

Moon, K.-S., Connor, J.J. and Fernandez, J.E. (2007). “Diagrid structural systems for tall buildings: characteristics and methodology for preliminary design.” *The Structural Design of Tall and Special Buildings*, 16: 205-230.

Moon, K. S. (2008a). “Sustainable structural engineering strategies for tall buildings.” *The Structural Design of Tall and Special Buildings,* 17:895–914

Morino, S., and Tsuda, K. (2001). “Design and construction of concrete-filled steel tube column system in Japan”, *Earthquake Engineering and Engineering Seismology*, Vol. 4, No. 1.

Mosalam, K.M., Talaat, M., and Binici, B. (2007). "A computational model for reinforced concrete members confined with fiber reinforced polymer lamina: implementation and experimental validation," *Composites:* Part B, 38(5-6): 598-613.

Munro, D. (2004). “Swiss Re´s Building, London.”, MA MIStructE, Associate, Arup and Partners, London

Nanni, A., and Bradford, N. M. (1995). ” FRP jacketed concrete under uniaxial compression.” *Construction and Building Materials*, 9(2), 115-124

Nims, D. K., Richter, P. J., and Bachman, R. E. (1993). "The use of the energy dissipating restraint for seismic hazard mitigation." *Earthquake Spectra*, 9(3), 467–489.

Okazaki, T., Arce, G., Ryu, H-C., and Engelhardt, M.D. (2005). "Experimental study of local buckling, overstrength, and fracture of links in eccentrically braced frames." *J. Struct. Eng. ASCE,* 131(10): 1526-1535.

Okazaki, T., and Engelhardt, M.D. (2007). "Cyclic loading behavior of EBF links constructed of ASTM A992 steel." *J. of Construction Steel Research*., 63:751–765.

Okazaki, T., Engelhardt, M.D., Nakashima, M., and Suita, K. (2006). "Experimental performance of link-to-column connections in eccentrically braced frames." *J. Struct. Eng. ASCE,* 132(8), 1201-1211.

Pantazopoulou, S. J., and Mills, R. H. (1995). "Microstructural aspects of the mechanical response of plain concrete." *ACI Mater. J.*, 92; 605-616.

Parvin, A., and Wang, W. (2001). "Behavior of FRP jacketed concrete columns under eccentric loading." *J. Compos. for Constr.*, 5(3), 146-152.

Perez F. J. (2004). "Experimental and analytical lateral load response of unbonded post-tensioned precast concrete walls." *Ph.D. Dissertation*, Department of Civil and Environmental Engineering, Lehigh University, Bethlehem, PA.

Pollino, M. and Bruneau, M. (2008). "Dynamic seismic response of controlled rocking bridge steel-truss piers", *Engineering Structure*s, 30(6), 1667-1676.

Popovics, S. (1973). “A numerical approach to the complete stress-strain curve of concrete”, *Cement and Concrete Research*, Vol. 3, pp. 583-599.

Rahimian, A. and Eilon, Y. (2007). “Something Old, Something New.” *Modern Steel Construction*, AISC, April 2007.

Ramadan, T., and Ghobarah, A. (1995). “Analytical model for shear-link behavior.” *J. Struct. Eng., ASCE*, 121(11), 1574-1580.

Restrepo, J.I. and Rahman, A. (2007). “Seismic Performance of Self-Centering Structural Walls Incorporating Energy Dissipators”, *ASCE Journal of Structural Engineering*, 133(11), 1560-1570.

Richards, P.W. and Uang, C-M. (2005). “Effect of flange width thickness ratio on eccentrically braced frame link cyclic rotation capacity.” *J. Struct. Eng. ASCE,* 131(10): 1546-52.

Richart, F. E., Brandtzaeg, A., and Brown, R. L. (1928). “A study of the failure of concrete under combined compressive stresses.” *Bulletin No. 185*, Univ. of Illinois, Engineering Experimental Station, Urbana, III.

Ricles, J. M., and Popov, E. P. (1987a). “Experiments on eccentrically braced frames with composite floors.” *Rep. No. VCBIEERC-87106,* Earthquake Engrg. Res. Ctr., Univ. of California, Berkeley, Calif.

Ricles, J. M., and Popov, E. P. (1987b). "Dynamic analysis of seismically resistant eccentrically braced frames." *Rep. No. VCBIEERC-87107,* Earthquake Engrg. Res. Ctr., Univ. of California, Berkeley, Calif.

Ricles, J.M., Sause, R., Garlock, M. and Zhao C. (2001) “Post-tensioned seismic-resistant connections for steel frames.” *J. Struct. Eng.,* 127(2):113–121

Rocca, S., Galati, N., and Nanni, N. (2008). “Review of design guidelines for FRP confinement of reinforced concrete columns of noncircular cross sections.” *J. Compos. Constr.,* **12** (1), pp. 80–92.

Roke, D., Sause, R., and Ricles, J.M. (2008) "Design concepts for damage-free seismic-resistant self-centering steel concentrically-braced frames." Proceedings, *13th World Conference on Earthquake Engineering*, Beijing, China.

Saadatmanesh, H., Ehsani, M. R., and Li, M.W. (1994). “Strength and ductility of concrete columns externally reinforced with fiber composite straps.” *ACI Struct. J.*, Vol. 91, No. 4 .

Saafi, M., Toutanji, H.A., and Li, Z. (1999). “Behavior of concrete columns confined with fiber reinforced polymer tubes.”, *ACI Mater. J.*, Vol. 96, No. 4.

Sakai, J., and Mahin, S. (2003). “Hysteretic behavior and dynamic response of re-centering reinforced concrete columns.” *Proceedings of the 6th Symposium on Seismic Design of Bridge Structures Based on the Ductility Design Method*, Tokyo, Japan.

Sakai, J., and Mahin, S. (2004). “Analytical investigations of new methods for reducing residual displacements of reinforced concrete bridge columns.” *PEER Report 2004/02*, Pacific Earthquake Engineering Research Center, University of California, Berkeley, CA.

Samaan, M., Mirmiran, A., and Shahawy, M. (1998). “Model of concrete confined by fiber composites.” *J. Struct. Eng.*, 124(9), 1025-1032.

Sause, R., Ricles, J.M., Lin, Y.C., Seo, C.Y. and Roke, D. (2010) "Performance-based design of self-centering steel frame systems.” *Advances in Performance-*

Based earthquake Engineering, Geotechnical, Geological, and Earthquake Engineering, Volume 13, Part 3, 287-296, DOI: 10.1007/978-90-481-8746-1 (27).

Schneider, S. P. (1998). "Axially loaded concrete-filled steel tubes", *J. Struct. Eng.*, 124(10), 1125-1138.

Shao, Y., and Mirmiran, A. (2004). "Nonlinear cyclic response of laminated glass FRP tubes filled with concrete." *Compos. Struct., 65*, 91-101.

Shao, Y., Zhu, Z., and Mirmiran, A. (2006). "Cyclic modeling of FRP-confined concrete with improved ductility." *Cement & Concrete Composites,* 28, 959–968.

Somerville, P., Smith, N., Punyamurthula, S., and Sun, J. (1997). "Development of ground motion time histories for phase 2 of the FEMA/SAC steel project." *SAC/BD-97/04*, SAC Joint Venture, Sacramento, CA.

Soo, K. J., Sik, K. Y., Hee, L. S. (2008). "Structural Schematic Design of a Tall Building in Asan using the Diagrid System" *CTBUH 8th World Congress*.

Spoelstra, M., and Monti, G. (1999). "FRP confined concrete model." *J. Compos. Constr.*, 3(3), 143-150.

Talaat, M., and Mosalam, K. (2008). "Computational Modeling of Progressive Collapse in Reinforced Concrete Frame Structures." *Pacific Earthquake Engineering Research Center,* PEER 2007/10.

Taranath, B. (1997). "Steel, Concrete, & Composite Design of Tall Buildings" *McGraw-Hill*, Second Edition.

Teng, J. G., Huang, Y. L., Lam, L., and Ye., L.P. (2007a). "Theoretical model for fiber-reinforced polymer-confined concrete." *J. Compos. Constr.,* 2-201-210.

Teng, J.G., Yu, T., Wong, Y.L., and Dong, S.L. (2007b). “Hybrid FRP–concrete–steel tubular columns: Concept and behavior,” *Construction and Building Materials*, 21: 846-854.

Thaghavi-Ardakan, S., and Miranda, E., (2006). “Probabilistic seismic assessment of floor acceleration demands in multi-story buildings”, *Report No. 162*, Stanford University, Palo Alto, California.

Varma, R.K., Barros, J.A.O., and Sena-Cruz, J.M. (2009). “Numerical model for CFRP confined concrete element subject to monotonic and cyclic loading.” *Composites: Part B*, doi:10.1016/j.compositesb.2009.05.005

Zareian, F. and Medina, R. A. (2010). “A practical method for proper modeling of structural damping in inelastic plane structural systems.” *Computers & Structures*, Vol. 88, 1-2, pp. 45-53.

Zhu, Z., Ahmad, I., and Mirmiran, A. (2006). “Seismic performance of concrete-filled FRP tube columns for bridge substructure.” *J. of Bridge Eng.*, 11(3), 359-370.

Zhu, S. and Zhang, Y. (2008). "Seismic analysis of concentrically braced frame systems with self-centering friction damping braces," *ASCE Journal of Structural Engineering*, 134(1): 121-131.

About the Author

Nasim Sadat Moghaddasi Bonab was born in Iran, Tehran. She earned her B.Sc. in Civil Engineering in 2003 and her M.Sc. in Structural Engineering in 2006, both from University of Tehran. In 2011, she completed her Ph.D. degree in Structural Engineering from University of Maryland.

Nasim started working in Dena Rahsaz Construction Company while she was a sophomore and continued her part-time collaboration with the same company and another construction company during her undergraduate studies. Upon graduation, she joined a colleague to establish a new firm, Hamon Rah Asia, where she worked as construction and technical manager for four years and directed five road construction projects.

During her doctorate studies, she has been serving as teaching assistant for seven academic semesters for different Civil Engineering courses. Nasim also cooperated with Nemetcheck Scia and provided consulting services on implementation of American steel and concrete structural design codes into Scia European software. In summer 2010, she joined WSP Cantor Seinuk - a pioneer firm in design of diagrid structure who has provided structural engineering services for Heart Tower and World Trade Center Towers in New York City - to get a better understanding of analysis and design of diagrid structure.

Nasim is a member of American Society of Civil Engineers, American Concrete Institute and Society of Women Engineers. Her technical and research interests include performance-based design, innovative and sustainable structural systems, seismic analysis/design of buildings and bridges, performance evaluation and progressive collapse of structures, material engineering and applications, structural software and application development, structural testing and computational mechanics.